NISTIR 7327

Design, Measurements and Performance Predictions for a Micromolded Refrigerant Expansion Device

David A. Yashar

U.S. DEPARTMENT OF COMMERCE
National Institute of Standards and Technology
Building Environment Division
Building and Fire Research Laboratory
Gaithersburg, Maryland 20899-8631

National Institute of Standards and Technology
Technology Administration
United States Department of Commerce

NISTIR 7327

Design, Measurements and Performance Predictions for a Micromolded Refrigerant Expansion Device

David A. Yashar

U.S. DEPARTMENT OF COMMERCE
National Institute of Standards and Technology
Building Environment Division
Building and Fire Research Laboratory
Gaithersburg, Maryland 20899-8631

April 2006

U.S. DEPARTMENT OF COMMERCE
Carlos M. Gutierrez, Secretary
TECHNOLOGY ADMINISTRATION
Michelle O'Neill, Acting Under Secretary of Commerce for Technology
National Institute of Standards and Technology
William Jeffrey, Director

ABSTRACT

The design, fabrication and testing of a thermopneumatic microfabricated valve for controlling refrigerant mass flow rate during expansion is presented in this report. This device was fabricated through nickel electroplating within very thick SU8 molds, thereby realizing expansion devices useful for small vapor compression systems through an inexpensive modified Ultraviolet-LIGA (German acronym for lithography, electrodeposition and molding) process.

This work begins with process development to create meso-scale nickel pieces through electroplating into SU8 molds. Two test benches were constructed and used to benchmark the performance of a prototype with compressed air and R134a. Three dimensional numerical simulations were performed on the flowfield within the device to predict its ability to control compressed air. A code was also developed to predict the device's temporal response and relationship between actuation level and power input.

The prototype was able to reduce the mass flow rate of the compressed air by 22 % at the conditions used in the analysis. The performance was then demonstrated in a 1.5 kW to 2 kW R134a vapor compression system to characterize both steady state and transient response. Steady state data showed that the mass flow rate of refrigerant could be controlled using the valve. The level of refrigerant subcooling defined the magnitude of the response. Steady state data taken at 750 kPa inlet pressure shows the mass flow rate was reduced by 4.2 % at 1 ºC subcooling and up to 10.8 % at 5 ºC subcooling for a given level of actuation. Transient system response was characterized using cyclic actuation of the device. The change in capacity was approximately 5 %, at the conditions used during these tests.

Keywords: HVAC&R, MEMS, Microfabrication, Refrigerant Expansion, SU8

ACKNOWLEDGEMENTS

I would like to thank Dr. Piotr Domanski, Dr. W. Vance Payne II, Dr. Mark Kedzierski, Dr. David Didion and Mr. John Wamsley of the National Institute of Standards and Technology (NIST) for their technical and laboratory support during this project.

I would also like to thank my dissertation advisor, Dr. Don DeVoe, Associate Professor at the University of Maryland, for his direction and assistance during this project. Also, I would like to extend gratitude to the members of my advisory committee at the University of Maryland, Dr. Amr Baz, Dr. Inderjit Chopra, Dr. Kenneth Kiger, and Dr. Reinhard Radermacher for their guidance, assistance, and cooperation.

I would also like to thank the Cornell Nanoscale Science and Technology Facility (CNF) for the use of their cleanroom during the fabrication of the DRIE prototype produced during this effort.

PREAMBLE

This report is essentially the dissertation of David Anthony Yashar which was submitted to the University of Maryland in partial fulfillment of his Doctor of Philosophy requirements.

DISCLAIMER

Certain trade names and company products are mentioned in the text or identified in an illustration in order to adequately specify the experimental procedure and equipment used. In no case does such an identification imply recommendation or endorsement by the National Institute of Standards and Technology, nor does it imply that the products are necessarily the best available for the purpose.

Table of Contents

List of Tables

List of Figures

Nomenclature

Parameter		Units
A_{cs}	Cross Sectional Area	m^2
C	Speed of Sound	m/s
C_p	Specific Heat Capacity	J/kg·K
D_h	Hydraulic Diameter	m^2
E	Young's Modulus	N/m^2
f	Friction Factor	dimensionless
Gr	Grashof Number	dimensionless
h	Enthalpy	kJ/kg
h_p	Height of Piston	m
k	Thermal Conductivity	W/m·K
L_c	Critical Length	m
M	Mach Number	dimensionless
m	Nodal Variable	dimensionless
$\dot{m}$	Mass Flow Rate	kg/s
n	Nodal Variable	dimensionless
P	Pressure	N/m^2
P_o	Stagnation Pressure	N/m^2
P^*	Choking Pressure for Fanno Flow	N/m^2
R	Universal Gas Constant	m^2/s^2·K
R^2	Residual Squared Error for Best Fit Curve	dimensionless
Re	Reynolds Number	dimensionless
r	Radius of Diaphragm	m
r_p	Radius of Piston	m
s	Entropy	J/kg·K
t	Diaphragm Thickness	m
T	Temperature	K
T_{ss}	Steady State Temperature	K
T_o	Stagnation Temperature	K
U_x	x-Component of Velocity	m/s
U_y	y-Component of Velocity	m/s
U_z	z-Component of Velocity	m/s
V	Shear Force	N/m^2
w	Pressure Differential Across Diaphragm	N/m^2

Nomenclature: Greek and other Symbols

Parameter		Units
α	Thermal Diffusivity	m^2/s
β	Coefficient of Thermal Expansion	1/K
γ	Ratio of Specific Heats	dimensionless
δ	Piston Deflection	m
ε	Time Lag	s
ϕ	Parameter used for Deflection Analysis Integration	m
ν	Poisson's Ratio	none
ρ	Density	kg/m^3
σ	Stress	N/m^2
σ_y	Yield Stress	N/m^2
τ	Time Constant	s
τ_s	Shear Stress	N/m^2
Θ	Steady State Temperature	K
$\forall$	Volume	m^3

CHAPTER I
Introduction

The vapor compression cycle is used to move energy from a low temperature reservoir to a high temperature reservoir. There are four major mechanical components of the vapor compression cycle which are necessary to implement this cycle. The four basic cycle components and the process which the refrigerant undergoes are shown below in Figure 1.1.

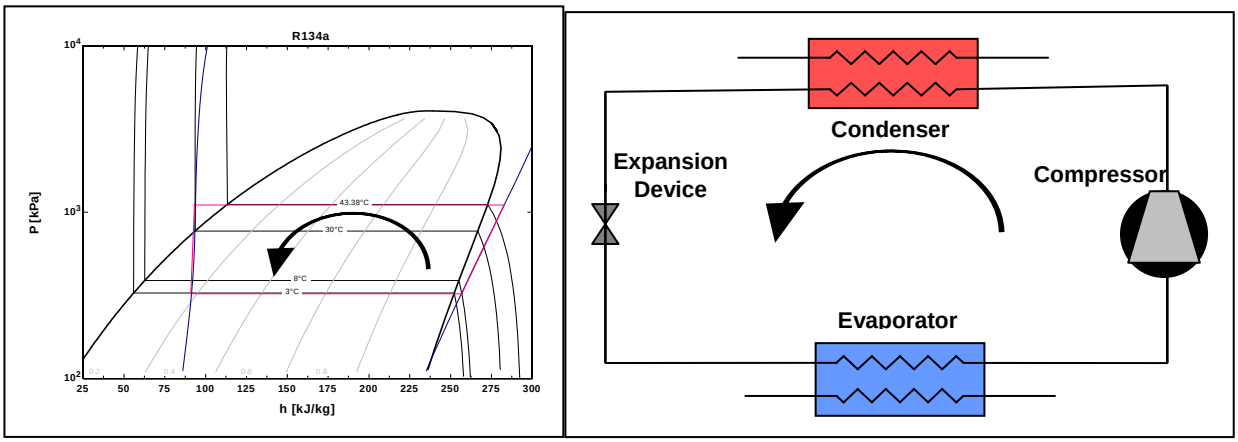

Figure 1.1 Vapor Compression Cycle and Required Mechanical Components

The compressor takes low pressure vapor and compresses it into a hot, high pressure vapor.

The condenser is a heat exchanger that takes the hot, high pressure vapor from the compressor and allows it to reject heat. While doing so, the fluid undergoes phase change and condenses into a liquid.

The expansion device is a flow constricting device; its purpose is to establish a pressure differential between the components on either side. Also, the expansion device is tasked with controlling the mass flow of the refrigerant through the cycle. As the refrigerant from the condenser passes through the expansion device, it undergoes substantial pressure drop. This pressure drop occurs without energy addition to the fluid; therefore, the temperature of the fluid is lowered through this process. Generally, the expansion device receives refrigerant that is near saturated liquid conditions, and it lowers the refrigerant's pressure to the point where it undergoes a partial change of phase and becomes a liquid-vapor mixture.

The evaporator is a heat exchanger that takes the low temperature liquid-vapor and allows it to absorb heat from an outside source. This causes the remaining liquid refrigerant to boil at a low temperature, producing a cooling effect.

1.1 Expansion Devices

Most of the smaller vapor compression systems use a simple, fixed area flow restrictor as the expansion device. Their simple design and low cost make them well suited for many applications. The most common of these devices are the capillary tube and the short tube restrictor.

The capillary tube is the device of choice for the smallest systems, such as household refrigerating appliances [1]. The capillary tube is a small gage section of pipe which induces a drop in pressure through friction. Typical sizes for capillary tubes range between 1 m and 6 m in

length, with a diameter between 0.5 mm and 2 mm. The exact diameter and length of a capillary tube must be selected based on the designed operating conditions and the specifications of the compressor.

Short tube restrictors are commonly used for many residential air conditioning and heat pump applications. They are also frequently used in automotive air conditioning systems. A short tube is a slug of metal, typically between 5 mm and 40 mm in length, with a small hole bored through its length. The short tube diameter typically ranges between 0.5 mm and 2 mm. A sketch of a short tube is shown below in Figure 1.2.

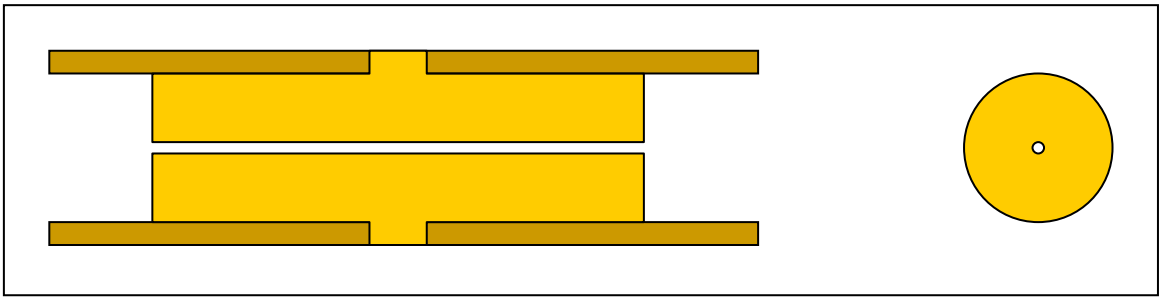

Figure 1.2 Short Tube Restrictor

Unlike the capillary tube, which induces pressure drop through friction, the short tube mainly induces pressure drop through abrupt changes in flow area. As the refrigerant enters one side of the short tube, the area contraction causes the refrigerant's pressure to drop, isenthalpically, until it begins to undergo phase change. At this point, the flow is termed "approximately" choked because it seems to be relatively insensitive to the downstream conditions [2, 3]. This is one of the most difficult problems in fluid mechanics to analyze because it involves metastable multiphase flow with the vapor phase traveling near its sonic velocity. Like the capillary tube, the short tube, is also a fixed area expansion device and must be sized according to its application.

A major disadvantage of these devices is that they must be designed for a unique operating condition. Therefore, a system operating with a fixed area expansion device loses efficiency when operating away from its design point, which often occurs through changes in the heating or cooling load. Also, a refrigerant working in the system is at a much higher pressure than atmospheric and therefore tends to leak out of a system over time if not perfectly sealed. When a system leaks refrigerant the cycle efficiency declines, and the impact is very large for a fixed area expansion.

Improved operational efficiency can be realized if the expansion device has the ability to control the mass flow rate of the refrigerant so that the demands of the application are aptly met [4]. There are a few types of expansion devices designed to control the mass flow rate of refrigerant based on information that is sensed during operation. The most common of which is the thermostatic expansion valve (TXV). The TXV is shown below in Figure 1.3 [5].

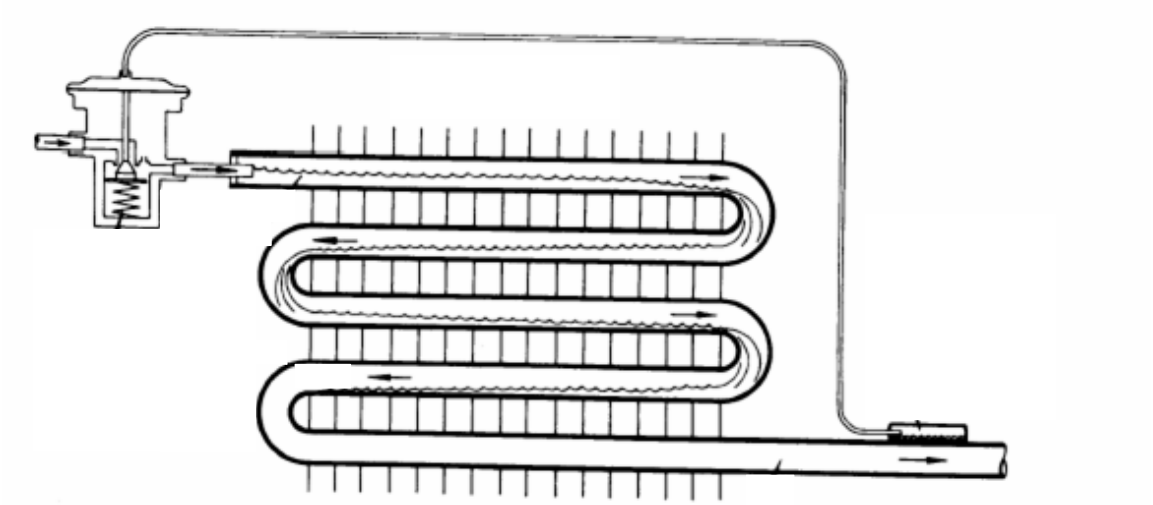

Figure 1.3 Thermostatic Expansion Valve

The TXV is controlled by a small bulb that is in thermal contact with the exit of the evaporator heat exchanger. The bulb's temperature is very close to the temperature of the refrigerant exiting the evaporator. The bulb is filled with liquid and vapor refrigerant, therefore the pressure in the bulb will vary according to the temperature of the refrigerant. A membrane on the upper portion of the expansion valve flexes in response to the changes in the pressure of the bulb, and thereby controls the movement of a plug inside the valve.

The operation is easily understood by example. If the refrigerant flow rate through the evaporator is too low, then the refrigerant would be exiting the evaporator at a warmer than desired temperature. This causes the temperature in the bulb to rise, thereby raising the pressure of the refrigerant in the bulb. The increased pressure in the bulb causes the membrane in the valve to flex downward (as shown in figure 1.3). Since the membrane is rigidly connected to the plug in the valve, the plug also moves downward which opens the flow passage for the refrigerant. This allows more refrigerant to flow through the valve into the evaporator.

TXV's are mainly used in moderate sized refrigeration systems and residential heat pumping and air conditioning applications. Obviously, they are much more expensive than the constant area devices; therefore, they are not typically used unless the cost can be offset by the improvement in operational efficiency. The benefits seen from employing TXV's over a fixed area expansion device can be quite substantial, particularly when the cycle must operate over varying conditions [6]. Figure 1.4, taken from Proctor [7], demonstrates the decline in residential air conditioner efficiency with off-design refrigerant charge. This occurs in approximately 2/3 of all residential systems at any moment in time [8].

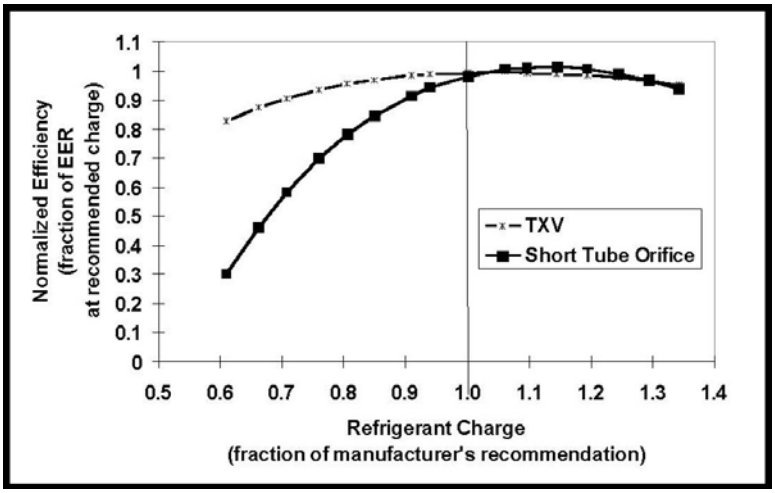

Figure 1.4 Air Conditioner Efficiency Relative to Refrigerant Charge for Systems with Short Tubes and TXV's (Proctor [7])

The obstacle for using a TXV over a constant area device is cost. If variable restriction expansion devices could be produced cheaply, they could be used in many different applications where they are currently uneconomical.

1.2 Applications

One application which would greatly benefit from an inexpensive, small, variable expansion device is that of automotive air conditioning systems. These systems are all oversized for their application out of necessity because such a system must be able to quickly reduce the temperature in the car when first started. Also, the compressors receive power directly from the crankshaft; therefore, these systems can not be hermetically sealed and consequently, they leak refrigerant over time.

According to the National Renewable Energy Laboratory [9], the average car in the United States has a fuel economy of 9.4 kilometers per liter. This reduces to 7.7 km/L while the air conditioner is operating. This means that a 15 % to 30 % increase in automotive AC efficiency, which is a reasonable expectation for a variable flow restrictor replacing its fixed area expansion device, will result in a 0.3 km/L to 0.5 km/L improvement in the fuel economy. The cost of using a variable expansion device for automotive air conditioning is substantially larger than the savings in fuel consumption; therefore, they are rarely used in automotive AC systems. Given the current global concerns of rising fuel costs and CO_2 emissions, this will likely get more attention; but it will not become common unless one can be produced inexpensively.

Another excellent application for an inexpensive controllable expansion device is in the concept of a smart distributor [10]. Most residential air conditioning systems use a multiple circuit evaporator. By dividing the refrigerant flow between parallel circuits in the evaporator, the penalties associated with the refrigerant's pressure drop in the evaporator are reduced.

Currently, the refrigerant's pressure is reduced by the expansion device, and then divided amongst the circuits in the evaporator using a distributor. After the refrigerant passes through a circuit and exits the evaporator, it is reconnected to the other circuits and the refrigerant goes on to the compressor, see Figure 1.5a. If a TXV is used, the sensing bulb is located at a point after the circuits are merged to ensure that no liquid droplets are passed to the compressor. Non-uniform air flow or partial frosting of the evaporator can significantly impact the uniformity of

the heat transfer from circuit to circuit. If the refrigerant exiting one of the circuits is not completely vaporized, the TXV will sense that there is not enough superheat in the suction line and the total mass flow rate to all of the circuits will be reduced.

The concept of a smart distributor works in a slightly different manner. Here, the distributor precedes the expansion process and the refrigerant to each circuit can be throttled individually based on the demands of that circuit, see Figure 1.5b. Therefore, if the refrigerant in one circuit does not completely vaporize, only the mass flow rate through that circuit will be reduced. As a consequence, the refrigerant will be rerouted through circuits that can accommodate greater mass flow.

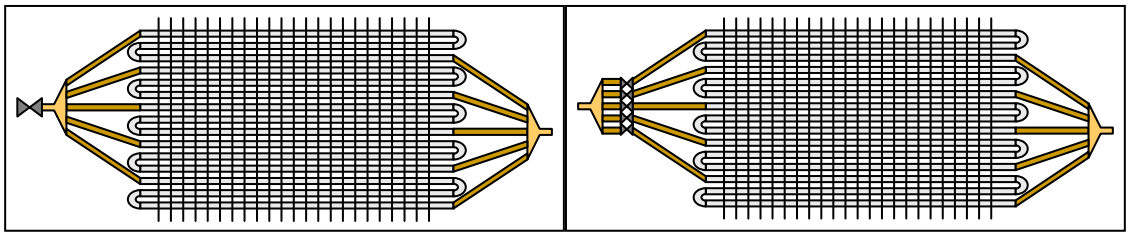

Figure 1.5 Multipath Evaporator without (a) and with (b) Smart Distributor

The benefits of a smart distributor were demonstrated at the National Institute for Standards and Technology through a series of tests [10]. For these tests, the capacity of a three circuit evaporator was measured under conditions of uniform air flow. Next, a non-uniform air flow pattern was imposed on the evaporator, with one half of the evaporator receiving more air than the other. A reduction in the evaporator capacity resulted. Finally, the individual expansion valves for each circuit were adjusted so that the exit conditions for each circuit were identical under non-uniform air flow conditions. Figure 1.6 shows the results of this study. In this figure, the blue diamonds depict the degraded performance of the evaporator under non-uniform air flow and uniform refrigerant distribution, the pink squares depict the capacity of the evaporator with non-uniform air flow and individually optimized expansion. It was found that the performance of this evaporator was severely reduced as the air flow became more non-uniform, and with a smart distributor, nearly all of the lost capacity could be recuperated.

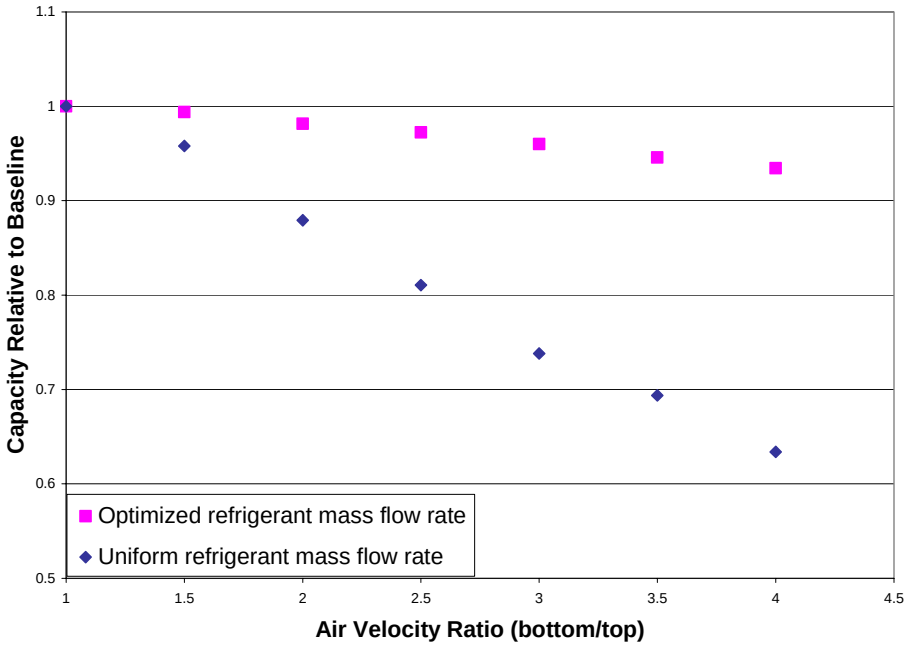

Figure 1.6 Degradation of Evaporator Capacity with Uniform and Optimized Refrigerant Distribution [10]

These are just two applications which would benefit greatly from a small, inexpensive, variable expansion device. In addition, there are a number of small HVAC&R systems that would benefit if their fixed area expansion device were replaced by such a device. Other applications include window-style air conditioners and household refrigerating appliances.

1.3 Existing MEMS Fluidic Valves

Fabrication technologies developed for MicroElectroMechanical Systems (MEMS) processes have been widely explored as a means to develop fluidic valves. Batch fabrication processes offer potential for satisfying the demands of refrigerant expansion at a market acceptable cost. Several groups have developed microfabricated valves that may be applicable for refrigerant expansion. Microstaq [11] has fabricated a valve for which refrigerant expansion is named as a possible application. Their valve is made from a three layer stack of silicon, fabricated using reactive ion etching (RIE), deep reactive ion etching (DRIE), and wet etching. The valve operation is based on the principle of thermal actuation controlling a sliding plate which alters the dimensions of an orifice. At the present time, Microstaq has not begun production, nor have they publicly disclosed any test data for refrigerant expansion.

Redwood Microsystems [12-15] has developed a boss-and-valve seat type valve which was demonstrated as a refrigerant expansion control device with flow rates of up to 3 g/s and differential pressures of up to 1 MPa. This device was designed and fabricated using inexpensive wet etching techniques. It uses thermal expansion of a liquid to seal a valve seat with a membrane. A schematic of their basic normally-open device is shown below in Figure 1.7. This device is comprised of three layers in a stack. The bottom and middle layers are made out of silicon and formed by anisotropic wet etching. The bottom layer is the orifice layer and serves as a connection point for the manifold; the middle layer contains a thin membrane. The top layer is made out of Pyrex, it has a metal resistive heaters patterned onto the

lower side and two contact holes drilled through it ultrasonically. In between the Pyrex layer and the membrane layer is a reservoir liquid, shown in blue.

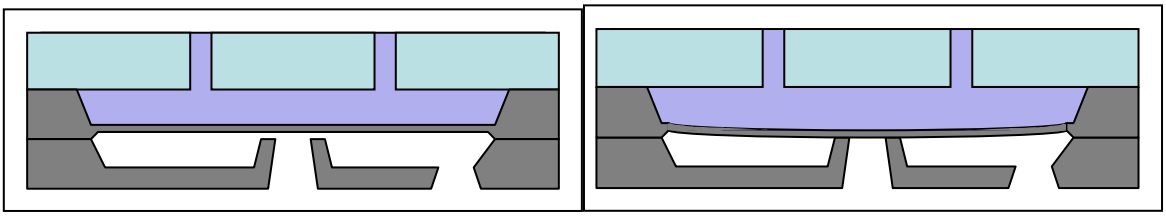

Figure 1.7 Fluidic Valve by Redwood Microsystems – basic normally-open design

The fluid being controlled flows upwards through the inlet port at the center of the stack and leaves through the exit port shown on the right hand side of the device. When the heaters are powered on, the liquid is warmed and it expands, pushing the membrane downwards. The membrane acts as a valve seat, partially or completely sealing off the inlet port to the device.

For the operation of the basic design, the liquid must undergo very large temperature changes. Although the magnitude of this temperature increase was not directly disclosed in any of their publications, it could be easily calculated from their work as being between 120 °C to 350 °C depending on the design parameters studied in their published works.

Since the basic design inherently provides a high degree of heat transfer between the liquid and the fluid passing through the device, Redwood Microsystems changed the design so that it could be used for refrigerant control. This design incorporates a fourth layer into the stack, as seen below in Figure 1.8, which greatly reduced the amount of heat transfer imparted onto the fluid.

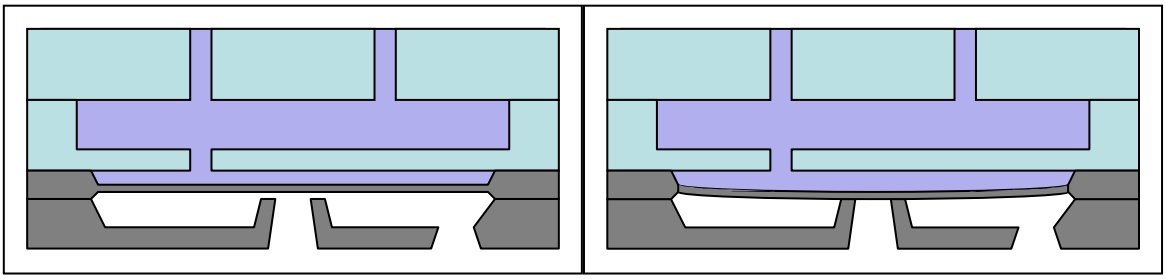

Figure 1.8 Fluidic Valve by Redwood Microsystems for Refrigerant Control

The additional layer is a Pyrex layer which sits between the membrane layer and the heater layer. This layer adds a considerable amount of volume to the liquid reservoir, thereby requiring a smaller temperature change to push the membrane onto the valve seat. Also, this Pyrex layer provides a mechanical stop for the membrane under conditions of rapid cool down. This device was demonstrated with refrigerant HFC134a, controlling flow rates between 0 g/s and 3 g/s with differential pressures of up to 1 MPa. Redwood Microsystems' devices have not received much acceptance in the HVAC&R market to date, mainly due to the refrigerant path inherent to its design.

In order for a fluid to flow through this device, it must travel up through the inlet port, be impinged on the membrane, turn 90° towards the outer edge of the device, and turn another 90° before leaving through the exit port. Furthermore, the fully-open gap between the membrane and the valve seat is typically on the order of 50 μm.

Real HVAC systems are made of copper, brass, and steel components which must be brazed or soldered together; therefore, there are always particulates entrained in the refrigerant. With the flow pattern dictated by the Redwood Microsystem design, it is inevitable that this device will become clogged with particulates. Some HVAC&R systems use filters in the refrigerant lines to catch these particulates; however, filters that can reliably remove particulates to the level required for this device can cause substantial pressure drop within the system. Therefore this device is acceptable for laboratory work, but HVAC&R systems manufacturers are skeptical. It is more desirable to ensure an open flow path on the order of 500 μm.

There are literally hundreds of other designs of devices being developed at numerous research institutions worldwide for the purpose of fluid control. The common concern is the ability to completely stop flow with very little leakage. In order to accomplish this, the concept of a boss and valve seat, as shown in the Redwood Microsystems design, is the focus of nearly all research. The problem with this is type of design is that current fabrication processes make it difficult to scale up such a design so that the fluidic path can pass particulates entrained in the flow. Nguyen and Wereley [16], Gad-El-Hak [17], Cui [18], and Kovacs [19] present good overviews for the types of device concepts that have been developed for fluid control.

One device which works on a fundamentally different basis than boss and valve seat is that of Papavasiliou [20-21], shown in Figure 1.9. This device works by opening and closing a gate across a fluidic channel, which thereby decreases or increases the resistance to the flow in the channel.

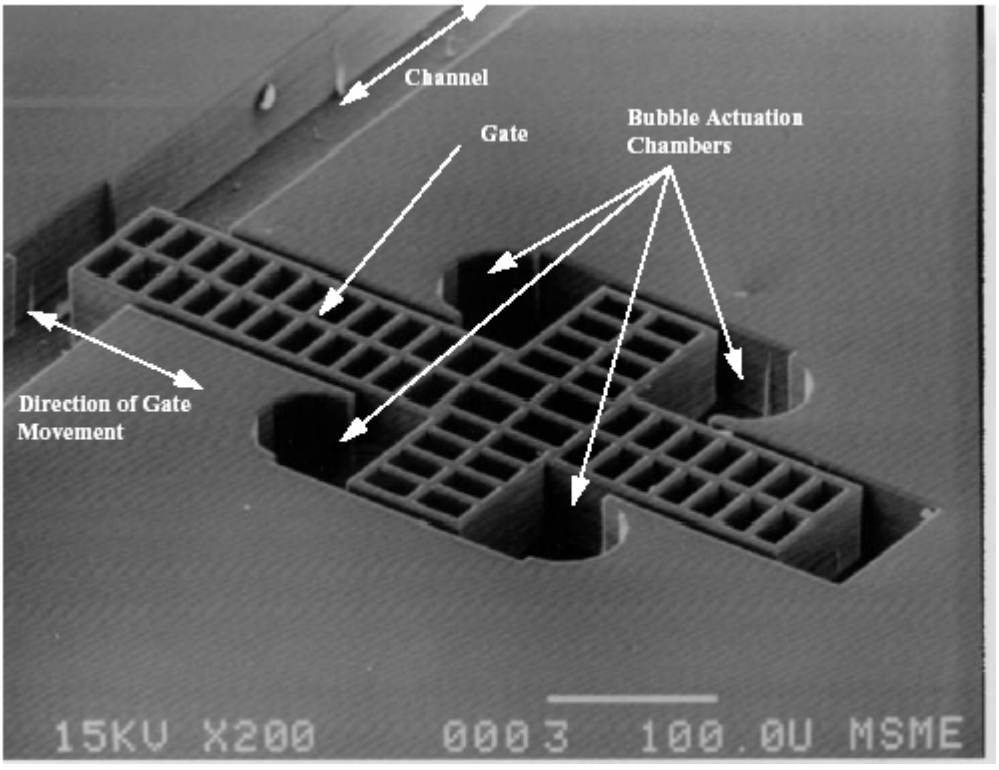

Figure 1.9 Bubble-Actuated Planar Microvalve by Papavasiliou

The Papavasiliou device works on the basis of bubble actuation. The slider is pushed back and forth by the formation of bubbles in the bubble actuation chambers. The actuation mechanism takes advantage of the relative importance of surface tension at the micro scale,

using it to hold the gate in position. The flow channel for this device is 75 μm tall and 100 μm in width.

What sets the Papavasiliou device apart from other microfabricated fluid controllers is that the motion of the slider and that of the fluid are in the same plane. Therefore, it can disturb the flow without forcing it through an obscure path. Although this device is too small for the application of refrigerant expansion, and it would be difficult to scale it up because of the actuation mechanism, this concept of planar impingement on the flow channel is attractive because it allows for a wide-open fluid passage when the device is not interfering with the fluid flow.

1.4 Fabrication Options

The feature sizes necessary to fabricate a device capable of being used for the expansion of refrigerants are on the order of 100 μm to 1 000 μm. This leaves very few options for the processes that can be used to build them, because this is on the larger side of available microfabrication processes. At the present time, there are three different types of processes which can be used to produce features of this magnitude [22]: wet chemical etching, deep reactive ion etching, and LIGA (including LIGA-like derivatives).

1.4.1 Wet Etching

Wet chemical etching processes are the most common processes used to fabricate microfluidic structures. This is because wet etching is generally very inexpensive and can make features that are large enough to facilitate fluid flow. The reserve is that the possible geometries formed with wet etching are limited. Wet etching can be isotropic or anisotropic.

Anisotropic wet etching works on the basis that, in crystal form, certain silicon atoms are more readily etched based on their orientation. Specifically, the {111} crystal planes are etched considerably slower than the {110} and the {100} planes. This allows the ability to etch V-shaped grooves, inverted pyramidal shapes, and vertical channel walls into single crystal silicon. Curved features or complex geometries, however, cannot be made with wet etching.

1.4.2 Dry Etching

Reactive Ion Etching, or RIE, refers to a dry etching technique in which large quantities of material may be removed from a substrate. An RIE chamber consists of two parallel plates, with a large voltage difference between them. The chamber is filled with an inert gas at low pressure which undergoes electrical breakdown when the electrons are accelerated in the existing field and transfer an amount of kinetic energy greater than the ionization potential to the inert gas' neutrals. Collisions generate free electrons and ions which reenergize, and a current begins to flow between the anode and cathode.

To use this as an etching mechanism, a wafer is placed between the parallel plates and in contact with the cathode. The energized electrons and ions bombard the surface of the wafer and remove material by reacting chemically with the substrate. A typical chemical reaction that takes place for reactive ion etching of silicon is $4F^{-} + Si^{4+} \rightarrow SiF_4$.

Deep Reactive Ion Etching (DRIE) refers to a slightly more complicated mechanism in which the RIE process can be manipulated to preferentially etch in one direction, specifically in the direction along the path from the anode to the cathode, perpendicular to the surface of the wafer. DRIE involves an iterated sequence of etching and passivation steps. The etching step is similar to the RIE process, but only lasts for a few seconds. The passivation step involves

depositing a thin polymer layer on the wafer to protect the sidewalls that were created during the etching process. The momentum in the ions during the subsequent etch step is not sufficient to remove the polymer coating on the side walls, but it is sufficient to remove the polymer that is facing the anode. The result is that the silicon is etched straight downward, regardless of crystal orientation.

The flexibility provided by this process allows the creation of shapes that would otherwise be impossible to produce in silicon such as curved or complicated features. The drawback is that DRIE is a somewhat expensive process. The use of DRIE will be explored for prototyping purposes, but it is probably too expensive to be used for a real device.

1.4.3 LIGA Based Methods

LIGA (German acronym for Lithographie, Galvanoformung, Abformung or lithography, electrodeposition, molding) is a process where a thick layer of polymethylmethacrylate (PMMA) is patterned using X-ray lithography and the resulting structures are used as a mold for electroplating. X-ray lithography offers many benefits in terms of fabrication tolerances and attainable thicknesses; however, it is very expensive. Low cost LIGA-like methods are currently being explored at numerous research institutions with promising results. Some researchers have worked with dry film photoresists, but these materials often lack the adhesive properties and chemical resistance that are necessary to make very tall structures [23, 24]. At the forefront are methods based on SU8, a negative tone, UV sensitive, epoxy based photoresist.

The SU8 molecule contains 8 epoxy groups which enable polymerization [25]. The SU8 molecule is shown below in Figure 1.10. In this figure, carbon atoms are denoted in black and oxygen atoms are red.

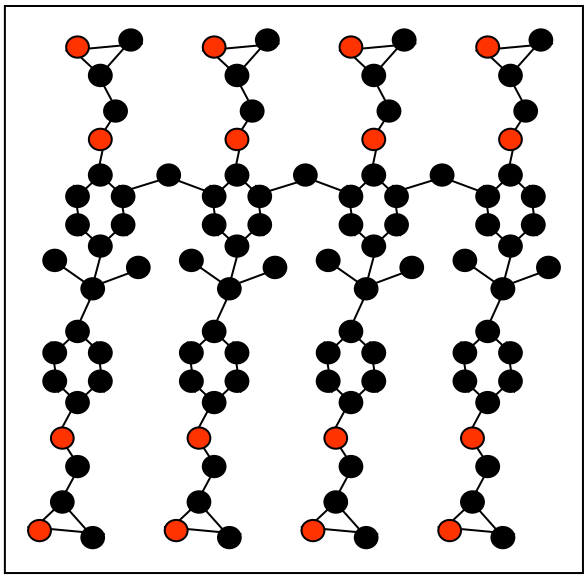

Figure 1.10 SU8 Molecule

Included with the SU8 is a photoacid generator, which forms a weak acid in the presence of ultraviolet light. This acid reacts with the epoxy groups on the SU8 molecules and enables them to cross link with other molecules, forming a rigid polymer structure. The cationic polymerization process is shown below in Figure 1.11. An epoxy group (a) becomes ionically bonded to a hydrogen atom (b). Next, the epoxy ring is opened by cross linking with an epoxy

ring from another SU8 molecule (c) and a hydrogen atom is freed (d) to react with another epoxy group.

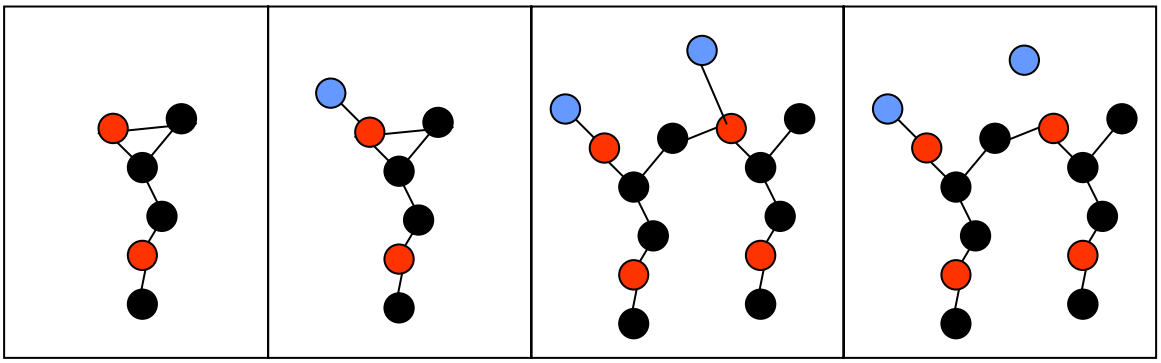

(a) (b) (c) (d)

Figure 1.11 Cationic Polymerization Process

Afterwards, the polymerized structures are rigid and resilient towards most chemicals; therefore, unpolymerized SU8 may be selectively etched with a solvent. This process is used to produce tall, rigid polymer structures with ultraviolet light, at very low cost.

There are many drawbacks involved with using SU8 as a material for a LIGA-based process. First, it is not possible to attain the same resolution with ultraviolet light as that attainable with X-ray lithography. This is simply a result of X-rays having a much smaller wavelength than UV light. Therefore, the effects of scattering are more pronounced with UV lithography. The resolution attainable with UV lithography, however, is suitable for many applications. Also, ultraviolet light, unlike X-rays, is absorbed by SU8. Because of this material property, there exists a theoretical upper limit to the thickness of a single layer of SU8 that can be patterned with UV light, approximately 2 mm.

Another issue which needs to be addressed is that SU8 is a relatively new material; therefore, the process parameters are not optimized for many feature sizes. A lot of information exists on SU8 application for 1 μm to 250 μm layers, but little information exists for thicker layers. In fact, there is currently conflicting information regarding these parameters.

During the polymerization process, SU8 molecules become highly tangled, which induces very large stresses within the material. With thicker and thicker films, this stress can cause SU8 to lose adhesion to the substrate on which it is deposited or approach the ultimate stress of the cross-linked material causing the SU8 to shatter. Therefore, there are a lot of stability problems involved with thick SU8.

Finally, once cross linked, SU8 is very resilient towards most chemicals. Therefore, it is not easy to remove SU8 at the end of a process. For this reason, SU8 is often used as a permanent structure. Removal of SU8 has been accomplished by various methods for different applications. Methods for removing SU8 are generally application specific because most of the devised methods will attack and/or affect other materials present in the fabrication sequence. Thus, any application involving SU8 removal must involve a unique plan for that fabrication sequence.

CHAPTER 2
Design Concept

The basic concept of the refrigerant expansion device presented in this report is rather simple. The operation of this device involves a small flow restrictor combined with a microfabricated actuator that is capable of moving an obstruction into and out of the refrigerant flow. Therefore, when the device is not actuated, the flow passage is similar in nature to a common short tube restrictor. When the device is actuated, the flow passage is partially blocked by an obstruction fixed to one of the boundaries. Inserting a flow obstruction into the short tube introduces a boundary discontinuity and reduces the cross sectional area of the passage, thereby producing a more restrictive tube.

2.1 Design

A sketch of this mechanism is shown in Figure 2.1, note that the flow path of the refrigerant is between the semi-circular tube and the flat wall in the direction perpendicular to this page.

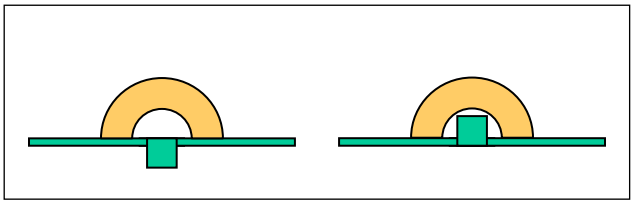

(a) Unactuated (b) Actuated

Figure 2.1 Conceptual Sketch of Refrigerant Expansion Device

The actuator consists of two parts, bonded together. The first of the two pieces consists of a thin membrane, with a piston fixed to it. A sketch of this is shown below in Figure 2.2.

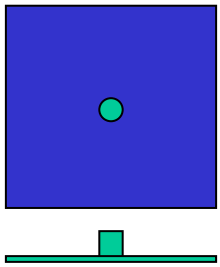

Figure 2.2 Sketch of Piston/Diaphragm

The second piece is a device containing a port slightly larger than the diameter of the piston. The port allows the piston to pass through and interact with fluid on the opposite side of this piece. Also, one of the pieces must have a rigid lip that maintains a small gap between the two pieces. A sketch of the coverplate device is shown below in Figure 2.3. In this figure, the spacer is shown as a circular divot removed from the device.

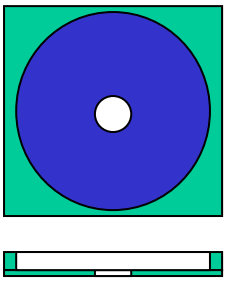

Figure 2.3 Sketch of Cover-plate Chip

The pieces are then assembled to produce the structure shown below in Figure 2.4.

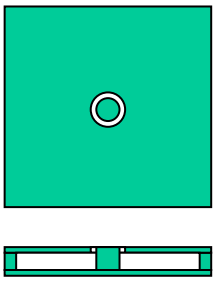

Figure 2.4 Actuator Assembly

The device's principle of operation is based on thermal expansion of a liquid in order to produce the necessary forces for actuation. Once the fabrication and assembly of the actuator has been completed, it is to be inserted between the short tube refrigerant flow restrictor and a reservoir filled with the actuating fluid; in this case an oil. Included in the oil reservoir is a small electric resistance heater. As thermal energy is added into the oil reservoir from the heater, the oil gets warmer and its density decreases. This expanding oil exerts pressure on the thin flexible membrane, which results in the membrane flexing outward. This movement pushes the flow obstruction into the short tube refrigerant passage. The final assembly and device actuation is shown in Figure 2.5. Note that the direction of the refrigerant flow is perpendicular to this page.

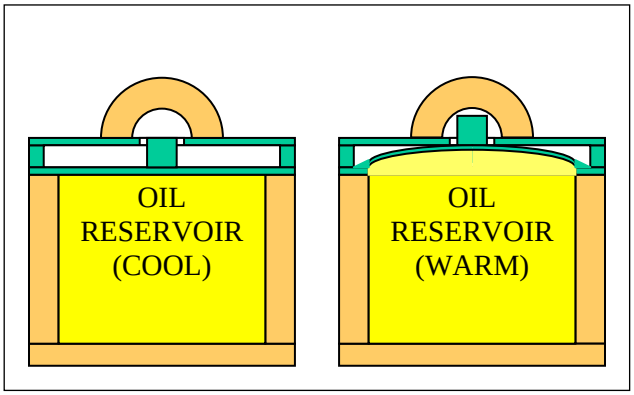

(a) Unactuated (b) Actuated

Figure 2.5 Final Assembly of Refrigerant Expansion Device Components

2.2 Simulation

2.2.1 Stresses on the Diaphragm

The membrane is the only moving part in the system. The walls of the oil cavity are much thicker than the membrane and will not flex. The membrane is exposed to the oil reservoir by a circular area. When the oil is heated, the circular area of the diaphragm will flex outward. Centered on top of the membrane is a post. When the diaphragm is flexed, the post is pushed into the refrigerant flow passage, thereby obstructing the refrigerant's flow.

The properties that are required to simulate the stresses on the diaphragm are Young's modulus, the yield strength, and Poisson's ratio. A design spreadsheet was generated to calculate the necessary dimensions of the device's features, based on the material properties and the expected movement.

The input to the design spreadsheet includes the following parameters:

- The desired deflection δ
- The thickness of the diaphragm, t
- The radius of the diaphragm, r
- The radius of the piston, r_p
- The height of the piston, h_p

The first parameter calculated from this input is the required pressure differential, w, across the diaphragm to make the center flex upward by a distance δ. For a circular diaphragm, these parameters are linearly related by the following formulas [16, 26]:

$$w = \frac{16 \cdot \delta \cdot E \cdot t^3}{3\left(1-\nu^2\right) \cdot r^4}$$

Once the required pressure differential is known, the maximum stress in the membrane due to the flexure is calculated as:

$$\sigma_{\max,\,flex} = \frac{3 \cdot w \cdot r^2}{4 \cdot t^2}$$

Next, there exists a stress on the diaphragm at the point where it is attached to the post. This stress is due to the force exerted by the refrigerant's interaction with the top of the post. In order to calculate the stress induced on the diaphragm an assumption was made that the worst case scenario would occur if the entire pressure differential between the evaporator and condenser were held at the tip of the post. This pressure difference was based on an air conditioning cycle using R134a, operating with a condensing pressure of 1.3 MPa (T_{cond} = 50 °C) and an evaporating pressure of 200 kPa (T_{evap} = -10 °C), representing a pressure difference of 1.1 MPa [27].

This pressure difference is multiplied by the cross sectional area of the flow channel that is blocked by the piston to obtain the shear force on the piston, V. The maximum stress on the diaphragm due to this shear force is [28]:

$$\tau_{s,\max} = \frac{4V}{3\pi r_p^2}$$

This stress is added to the stress resulting from the diaphragm flexure by superposition to obtain the total maximum stress on the diaphragm. This is then compared to the yield stress of the material to obtain a factor of safety.

Using this design spreadsheet, the device material could be easily changed by inserting the appropriate values for Young's modulus and the yield strength. The thickness and radius of the diaphragm, as well as the dimensions of the post and the desired flexure could easily be manipulated while monitoring their effect on the maximum stress.

2.2.2 Oil Coefficient of Thermal Expansion

It was necessary to measure the coefficient of thermal expansion of the oil used in the reservoir, so that its interaction with the membrane could be predicted. The particular oil that was selected for this application was polyalkalene glycol (PAG), a common lubricant for use with hydrofluorocarbon (HFC) refrigerants. In order to measure the coefficient of thermal expansion, a known amount of PAG was placed in a graduated cylinder and the volume of the oil in the cylinder was monitored as the temperature varied.

A 500 mL graduated cylinder was used for this experiment. A fixed mass of PAG was placed into the cylinder along with a thermocouple probe. The cylinder was then placed in a refrigerated environment for a period of time and allowed to cool. Heat was added to the cylinder by placing in quiescent air, then in a warm bath, during which time the temperature and volume was recorded. The following data was taken for a mass of 387 g:

Table 2.1 Volume Measurements for PAG

T (K)	$\forall$ (m^3)	ρ (kg/m^3)
280	0.000399 ± 0.000001	969.9 ± 2.4
285	0.000399 ± 0.000001	969.9 ± 2.4
290	0.000400 ± 0.000001	967.5 ± 2.4
295	0.000400 ± 0.000001	967.5 ± 2.4
300	0.000401 ± 0.000001	965.1 ± 2.4
305	0.000403 ± 0.000001	960.3 ± 2.4
310	0.000403 ± 0.000001	960.3 ± 2.4
315	0.000404 ± 0.000001	957.9 ± 2.4
320	0.000405 ± 0.000001	955.6 ± 2.4
325	0.000405 ± 0.000001	955.6 ± 2.4
330	0.000406 ± 0.000001	953.2 ± 2.3

The density data points were then fitted with the best fit straight line:

ρ (kg/m^3) = 1073.46-0.3652*T (K).

The coefficient of thermal expansion (β) at 295 K was calculated as a reference:

$$\beta = -\frac{1}{\rho}\left(\frac{\partial \rho}{\partial T}\right)_P = 0.0003755$$

2.2.3 Relationship Between Oil Temperature and Piston Motion

Once the dimensions of the diaphragm and piston were deduced, and the thermal expansion properties of the oil were measured, the volume of additional space in the oil cavity due to the flexure was calculated. To calculate this volume, the shape of the flexed diaphragm is taken from [16].

$$y = \frac{3w\left(1-\nu^2\right)}{16Et^3}\left(r^2-\phi^2\right)^2$$

Therefore, the volume of additional space underneath the diaphragm is calculated from the 2-dimensional axisymmetric integral underneath this curve as shown below:

$$\forall = \int 2\pi\phi y \partial\phi = \int_0^r 2\pi\phi \frac{3w\left(1-\nu^2\right)}{16Et^3}\left(r^2-\phi^2\right)^2 \partial\phi$$

$$\forall = \frac{\pi w\left(1-\nu^2\right)}{16Et^3} r^6$$

Substituting the relationship for the pressure differential, w, the volume reduces to:

$$\forall = \frac{\pi\delta r^2}{3}$$

Another spreadsheet was generated to construct a relationship between the oil temperature and the displacement of the piston. In order to generate this relationship, all of the relevant parameters were calculated as a function of the displacement in the following manner.

The pressure differential, w, was calculated from the displacement, δ, and the material properties. Next, the additional volume of oil was calculated from the relationship derived above, which then corresponds to the additional volume that the oil needs to occupy in order to push the diaphragm outward by the distance δ.

The initial volume of the oil placed behind the diaphragm and its temperature during assembly is used in conjunction with its thermal expansion coefficient to calculate the temperature that the oil must be in order to fill this additional volume. By working with these equations in a spreadsheet form, the required oil temperature was calculated for every 10 μm of vertical displacement of the piston. Once these calculations were tabulated, the results were fit with a curve. This curve can then be used to predict the displacement as a function of the oil temperature.

CHAPTER 3
Performance Measurement Methodology

Two separate test beds were constructed to validate the performance of the device. A breadboard HVAC system capable of delivering a large range of operating conditions was constructed as the primary test apparatus. After the first design of the device was fabricated and assembled, measurement of its performance in this system was attempted. Based on the findings of the first prototype, a second test bed was constructed to test the device's ability to control the flow of compressed air.

There are two reasons for this second test apparatus. The first reason is that it is not possible to analytically or numerically predict the flow of flashing refrigerant through the geometry presented by this device. The only methods of mass flow prediction currently available rely on empirical data based on present day expansion devices. By using a single phase fluid, it is possible to predict the performance with numerical methods; thereby, providing a basis to compare with measurements. The second reason for constructing the compressed air test apparatus is that it provides a testing environment that can be operated at significantly lower pressures, without excessive vibration, and is therefore more likely to allow proper operation of the device during the developmental process.

3.1 Compressed Air Test Apparatus

A simple test apparatus was constructed to measure the flow of air through the device. A supply of compressed air is connected to the device. A manual valve is located between the apparatus and the compressed air supply to control the inlet pressure to the device. A pressure transducer is located upstream and downstream of the device. A manually adjustable needle valve is located downstream of the device to adjust the back pressure. A hose is connected to the outlet of the device and discharges into a basin full of water. As air is discharged into the basin, it is collected in an inverted container which is initially full of water. This container is delimited with markings that read up to 8 L. A schematic of this apparatus is shown below in Figure 3.1.

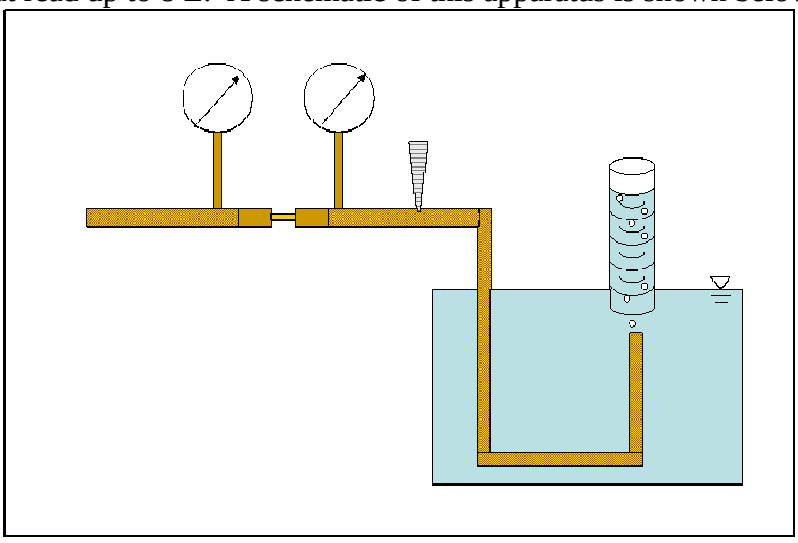

Figure 3.1 Schematic of Gas Flow Test Apparatus

With this apparatus, the air passing through the device over a period of time can be collected with the graduated cylinder and this could then be used to determine the mass flow rate of air through the device.

Initially, the manual valve to the compressed air supply is closed and the discharge hose is left outside the water basin. During this time, the ambient pressure is recorded. Next, the valve is opened and adjusted until the desired supply pressure is stable. Simultaneously, the downstream needle valve is adjusted to fix the back pressure. The hose is then placed underneath the container and a stopwatch is used to monitor the time to fill the container. Once the container is filled to a level near the 8 L mark, the time is logged and the discharge hose is moved so that it no longer sends air to the container.

The container is then held so that the water level inside is even with the water level outside so that the pressure of the air in the cylinder is equal to the atmospheric pressure. The volume of air in the cylinder is recorded. A thermocouple probe is then placed inside the container and the temperature of the air is recorded. The mass of the air collected inside the container is calculated from the volume, the ambient pressure and the air temperature. The mass is then divided by the amount of time to fill the container to obtain the mass flow rate.

The upstream pressure transducer was calibrated using a standard dead weight tester with 5 points in the range of 100 kPa to 275 kPa with an uncertainty of 0.15 % with 95 % confidence. The uncertainty of the thermocouple was 0.15 ºC with 95 % confidence and was calibrated between 10 ºC and 50 ºC using a thermistor. Temperatures and pressures are recorded through a virtual instrument interfacing with a data acquisition system. This virtual instrument communicates with three channels of a 20 channel relay card on the data acquisition system, one channel for the pressure transducer and one for each thermocouple.

3.2 Breadboard Vapor Compression Test Apparatus

A vapor compression system was constructed and outfitted with instrumentation to test the device's ability to control the expansion of a refrigerant. The test loop was designed so that the operating parameters could be easily manipulated and a large range of operating conditions could be obtained. The test rig consists of three major flow loops: (1) a refrigerant flow loop which contains a detachable test section, (2) a cold water-glycol (heat transfer fluid, HTF) flow loop used to exchange heat with the refrigerant flow loop's evaporators, and (3) a warm HTF flow loop used to exchange heat with the refrigerant flow loop's condenser.

A schematic of the main loop of the experimental setup is shown in Figure 3.2. An open-drive compressor is used to pump the refrigerant through the loop. This compressor is capable of pumping 1.35 m^3/h to 10.8 m^3/h of refrigerant over its acceptable input drive of 500 RPM to 4 000 RPM. The drive shaft for this compressor is controlled by 3 700 W motor capable of delivering up to 1 745 RPM at 60 Hz input; therefore, the maximum pumping capability of the compressor is 4.71 m^3/h. The motor speed is controlled by a variable frequency AC inverter. An oil separator was placed near the compressor discharge so that the oil concentration in the circulating refrigerant would be minimized.

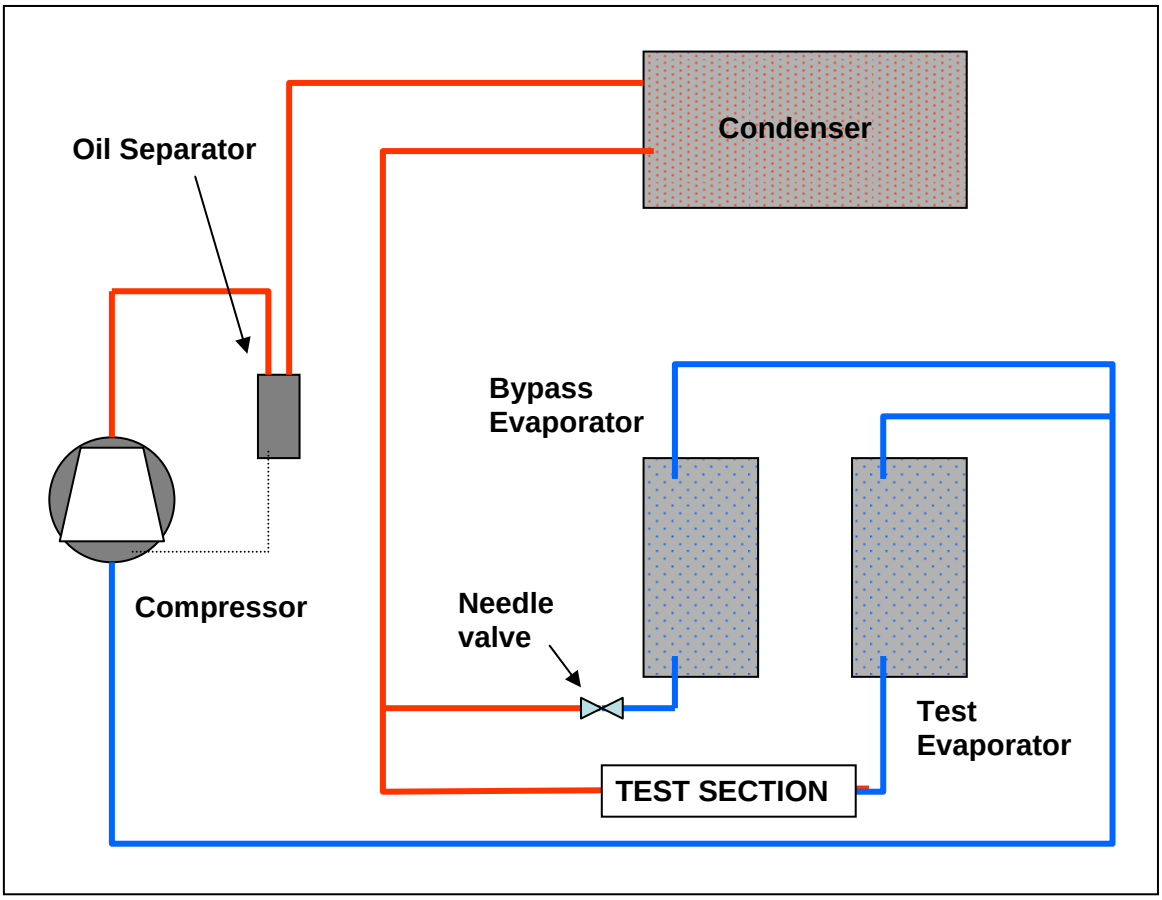

Figure 3.2 Refrigerant Flow Loop for Vapor Compression Test Apparatus

After the oil separator, the refrigerant changes phase into a liquid and is subcooled by exchanging heat with the condenser HTF flow loop. Next, the liquid line splits into two circuits.

The test circuit directs refrigerant through the test section where its pressure is reduced and it flashes to two phase. The test section consists of two manual shut off valves with the flow restriction device between. This allows for easy removal and change of flow restrictors. After passing through the test section, the refrigerant enters a brazed plate heat exchanger, where it absorbs energy from the evaporator HTF flow loop. After exiting the evaporator, the refrigerant passes through a vapor turbine meter to measure its flow rate.

Constructed in parallel to the test section and test evaporator is a bypass evaporator with a manually controlled needle valve. The bypass loop also contains a bonnet valve which can close this circuit completely. This loop allows refrigerant to bypass the test section and test evaporator. The outlet of this bypass evaporator connects to the exit of the test evaporator and the refrigerant from both circuits returns to the compressor.

Temperatures are monitored using copper-constantan (type-T) thermocouples placed at the compressor discharge, the condenser inlet, and the condenser exit. Additionally, five thermocouples are placed at the test section inlet, test section exit, test evaporator outlet, bypass evaporator inlet, and bypass evaporator outlet. Five thermocouples are used at these locations so that these temperatures can be measured with higher confidence. Pressure measurements are recorded with transducers located at the compressor exit, the test section inlet, test section exit, and the test evaporator exit.

The condenser HTF flow loop is shown in Figure 3.3. It is circulated by a single speed pump which draws a 50/50 mix of Dowtherm SR-1 and water from a 230 - liter container. A bypass valve is located in parallel with the pump so that the flow rate of HTF can be reduced from the maximum output of the pump. After the pump, the HTF passes through a heat exchanger where it is cooled by chilled water. Next, an electrical resistance heater, capable of delivering between 0.0 kW and 1.5 kW, is used to set the temperature of the HTF before it enters the condenser.

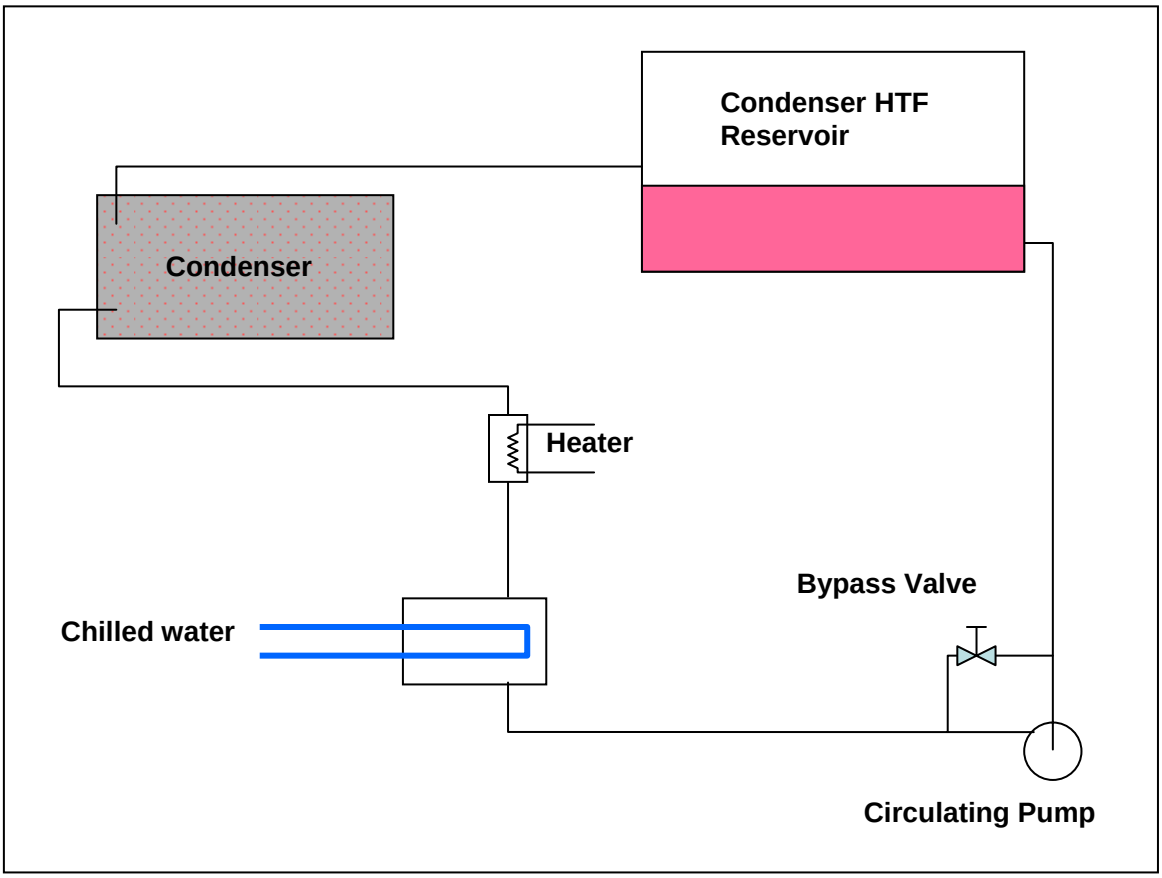

Figure 3.3 Condenser HTF Flow Loop for Vapor Compression Test Apparatus

After the HTF passes over the heater, it enters the condenser where it removes energy from the refrigerant loop. Upon leaving the condenser, the HTF returns to the 230 - liter container.

A thermocouple is located at the inlet to the condenser. Also, 10 junction thermopiles are used to monitor the temperature change that the HTF undergoes as it passes through the chilled water heat exchanger, the electrical resistance heater and the condenser. The flow rate of HTF is estimated by dividing the heat addition from the electric heater by the temperature change and the specific heat of the HTF.

The evaporator HTF loop is shown in Figure 3.4. The evaporator HTF is also drawn from a 230 - liter container containing a 50/50 mix of Dowtherm SR-1. It is circulated by a single speed pump and the flow rate is controlled by a manual bypass valve located in parallel with the pump. Down stream from the pump, the mass flow rate of HTF is measured by a Coriolis effect mass flow meter. Next, the temperature of the HTF is set by two electrical

resistance heaters which are capable of adding up to a total of 3 kW of heat transferred into the flow.

The flow is then split into two parallel circuits each controllable with a manual ball valve so that all of the HTF can be routed through either circuit or split between them. Each circuit passes through an evaporator to exchange heat with the refrigerant loop. A turbine meter is located prior to the entrance of the bypass evaporator and the flow through each circuit is deduced by subtracting this reading from that of the Coriolis mass flow meter located after the pump. It would be more desirable to place the turbine meter in the opposite circuit, so that the HTF flow into the test section could be measured directly; however, the physical constraints of the test system would not allow this. Also, the bypass evaporator was completely shut off during the test measurements, therefore there was no HTF flow through it and the test evaporator HTF flow was read directly from the coriolis flow meter.

After exiting the evaporators, the HTF then enters another heat exchanger where it is cooled by chilled water. The chilled water supply is a single speed system; therefore, ball valves are located upstream of and in parallel with the chilled water heat exchanger so that the flow of HTF may partially or entirely bypass the chiller. The HTF returns to the 230 - liter reservoir after passing this station.

Five type-T thermocouples are located and the entry and exit point of each evaporator. The temperature rise seen by the HTF as it passes the electrical resistance heaters is monitored with a 10 junction thermopile. Also, the temperature of the HTF is monitored with a thermocouple at the point where the flow splits between the two circuits.

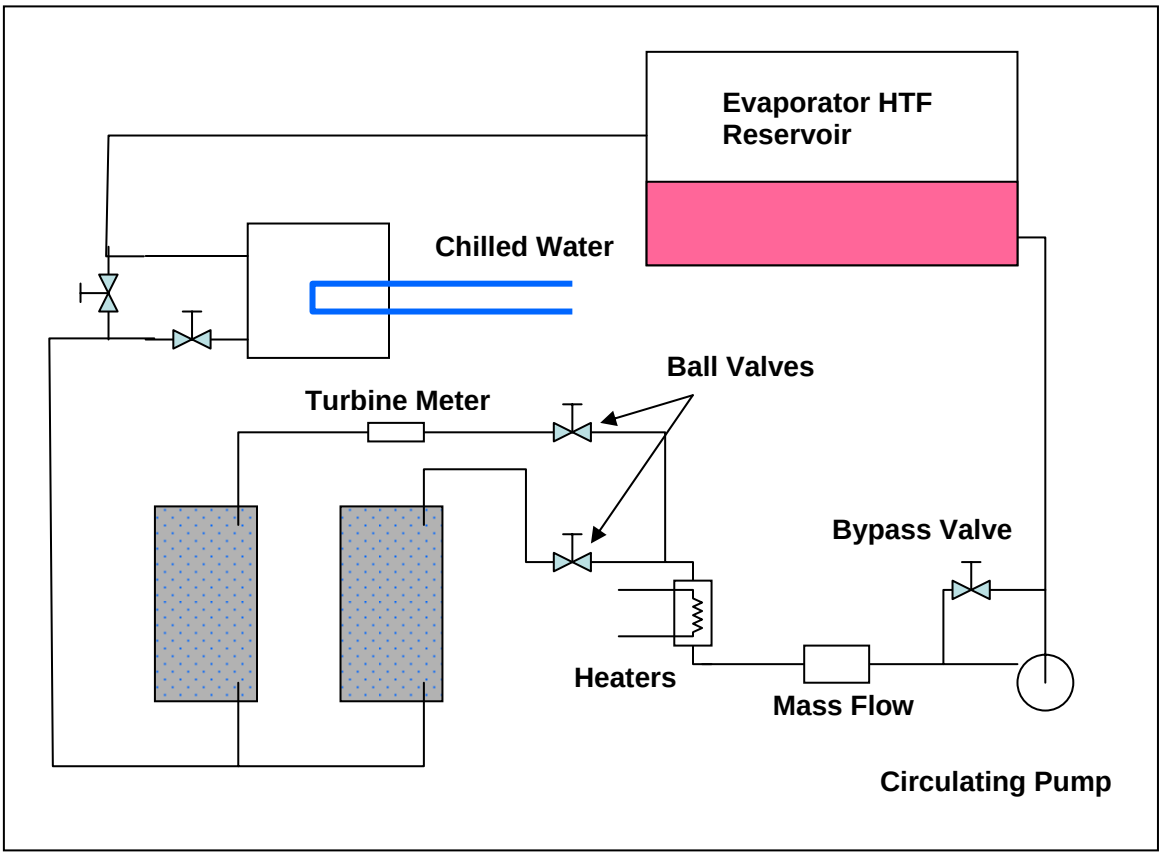

Figure 3.4 Evaporator HTF Flow Loop for Vapor Compression test Apparatus

All measurement devices are connected to a data acquisition and control unit. This system interfaces with a personal computer through a GPIB connection. A virtual instrument was scripted to monitor the system's pressures, temperatures and flow rates and to compute the enthalpy, entropy, subcooling, saturation properties, evaporator inlet quality and evaporator capacity. The evaporator HTF loop flow rates and temperatures are also monitored and the HTF-side evaporator capacity is calculated from these parameters and compared to the refrigerant-side capacity. All of the heaters in all three loops are also controlled by the virtual instrument.

All thermocouples used in this experimental setup were calibrated to within 0.15 ºC at 95 % confidence, all pressure transducers to within 0.2 % reading at 95 % confidence, and all flow rate measurement devices were calibrated to within 0.3 % reading at 95 % confidence.

CHAPTER 4
DRIE Silicon Prototype

The first method of prototyping this device was Deep Reactive Ion Etching (DRIE) of a Silicon-on-Insulator (SOI) wafer. An SOI wafer is a composite of three layers, consisting of two layers of silicon, with a layer of SiO_2 sandwiched between them. The reason that SOI wafers are useful is that DRIE will etch silicon approximately 200 times faster than SiO_2. SiO_2 therefore provides a good etch stop for the DRIE process. The flexibility provided by DRIE on a SOI wafer is ideal for fabricating a prototype of the device in this study.

It is very common for the two silicon layers to have very different thicknesses; the thicker of the two is called the base and the thinner is called the handle. In order to fabricate the first device from an SOI wafer using DRIE, the simplest method is using the handle of the SOI as the diaphragm and etching the base in such a way as to leave the piston attached to the center of the diaphragm. For the second device, it is desirable to use the thin handle layer as the cover plate with a pass through for the piston while using the thick base layer to provide a space between the two chips in the assembly. Figure 4.1 describes the process flow used to produce the piston/diaphragm device and Figure 4.2 describes the process flow used to produce the coverplate device.

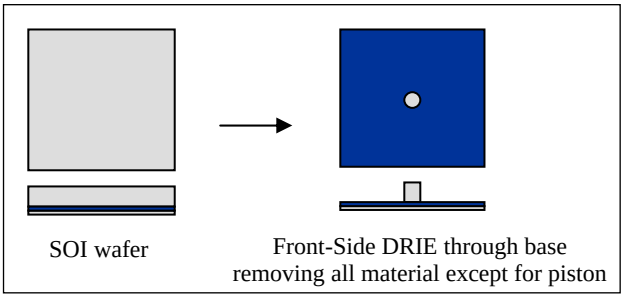

Figure 4.1 Process Flow used to Produce the Piston/Diaphragm Chip

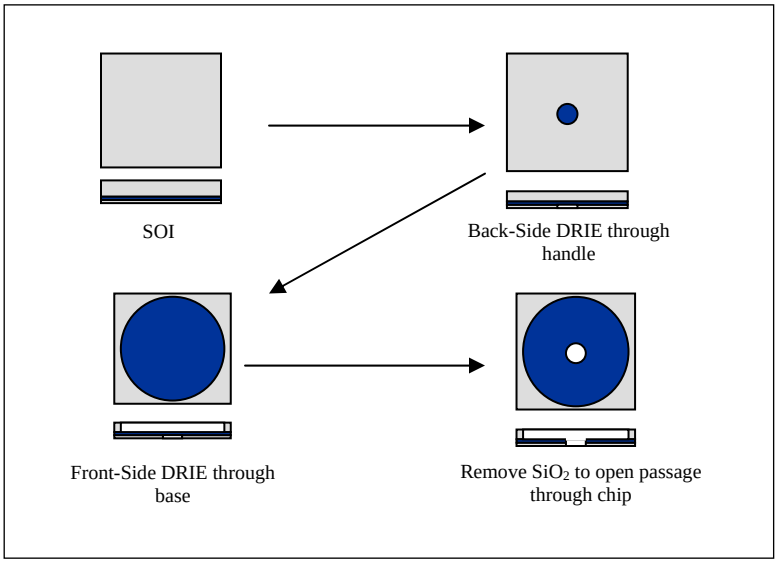

Figure 4.2 Process Flow used to Produce the Coverplate Chip

4.1 Design and Fabrication

For this fabrication run, 100 mm diameter SOI wafers were obtained. The base layers of these wafers were polished to a thickness of 450 μm, the handle was polished to a thickness of 75 μm, and the silicon dioxide layer between them was 1 μm thick.

The dimensions for this design are somewhat dictated by the specifications of the SOI wafers. In this case, the wafer dictates the diaphragm thickness of 75 μm and the space between the two pieces as well as the piston height is fixed to 450 μm. These specifications, incidentally, force the design to be slightly different than explained in the last section. This is because the piston height should be equal to the diaphragm thickness plus the gap spacing; therefore, the devices resulting from this fabrication run will be assembled such that the piston will be recessed 75 μm from the top of the coverplate when the diaphragm is not flexed. This could have been remedied by polishing one of the wafers by an additional 75 μm thereby reducing the gap to 375 μm. For the first fabrication run, however, this is acceptable because the actuation can still be demonstrated and the additional cost of polishing further is not warranted.

Given the constraints imposed by the specifications of the wafer, the dimensions of the features were calculated so that a safety factor of approximately 2 was maintained during operation. Since the material properties of single crystal silicon are directional, the following material properties were selected so as to result in the greatest stress on the diaphragm and they were input to the design spreadsheet [22]:

E = 186.5 GPa
σ_y = 1.8 GPa
ν = 0.21

In addition, the desired deflection was 200 μm, which in this case would move the tip of the piston 125 μm beyond the coverplate. The piston diameter was 1 000 μm. With these parameters, the diaphragm diameter was found to be 8 800 μm, which results in a safety factor of 1.8 relative to diaphragm failure.

4.1.1 Masks

The first step was to create the photolithography masks for the fabrication run. A computer aided drafting software package was used to generate the drawings needed for the masks. A total of 5 masks were needed for this fabrication run, which included one mask for each of the three DRIE etches outlined in the previous section and one mask for each etch to outline the borders of the devices on the wafers. These borders are necessary because they provide a line through which the wafer may be cut later to obtain the devices. On each of the five masks, an array of 25 (5 X 5) devices were drawn.

Mask # 1 outlined the borders for the piston/diaphragm devices. For this mask, the pattern consisted of a 5 X 5 array of square dark field boxes with a side of dimension 16 950 μm. The light fields of the masks were the lines that separated the squares; the widths of these lines were 100 μm.

Mask # 2 outlined the pattern for the second etch on the piston/diaphragm device. This pattern consists of a dark field circle, centered inside of a light field square. The circle has a diameter of 1 000 μm, as was the desired piston diameter. The square has a dimension of 12 000 μm on a side, which once fabricated will be wide enough to fit the coverplate device.

The squares on the array of devices were separated by a dark field of 4 950 μm. A drawing of the patterns on the masks used for the piston/diaphragm devices (Mask # 1 and Mask # 2) are shown in Figure 4.3

.

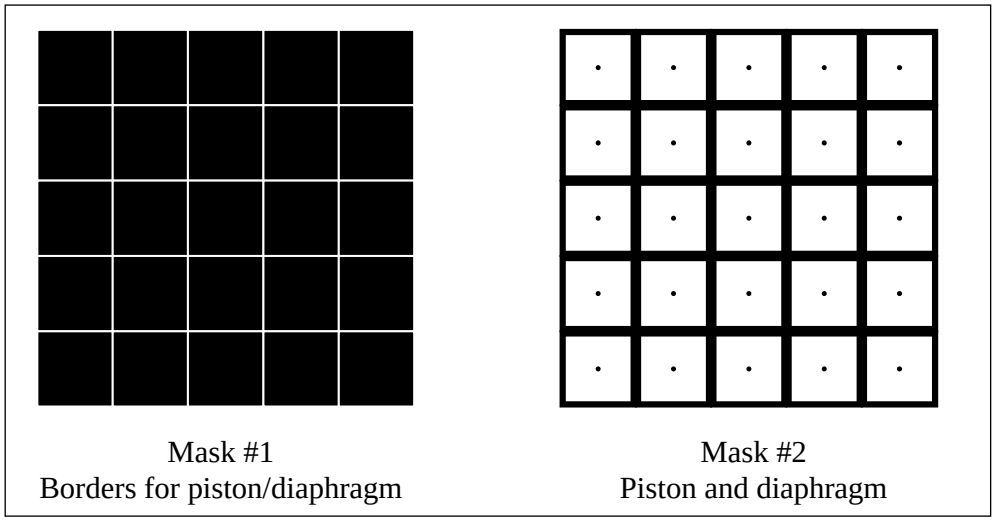

Figure 4.3 Masks used for Piston/Diaphragm Chip

Mask # 3 outlined the borders on the coverplate device. This mask is very similar in pattern to mask #1, however the dimensions are slightly different. For this mask, the sides of the dark field squares were 11 800 μm, and the light field lines were 5 150 μm thick. The dimension of these features are slightly smaller than that of Mask # 2 because the features produced with this mask will fit into the ones produced with Mask # 2.

The pattern on Mask # 4 is used to etch the hole through which the piston will move. This pattern was transferred to the handle side of the coverplate wafer. These holes are 1 100 μm in diameter, which is 100 μm larger than the piston.

The last mask, Mask # 5, was transferred onto the base side of the coverplate device. This pattern produces a large diameter hole (8 800 μm) which will provide a gap between the two devices after they are assembled. Figure 4.4 shows the patterns on the masks used for the coverplate device.

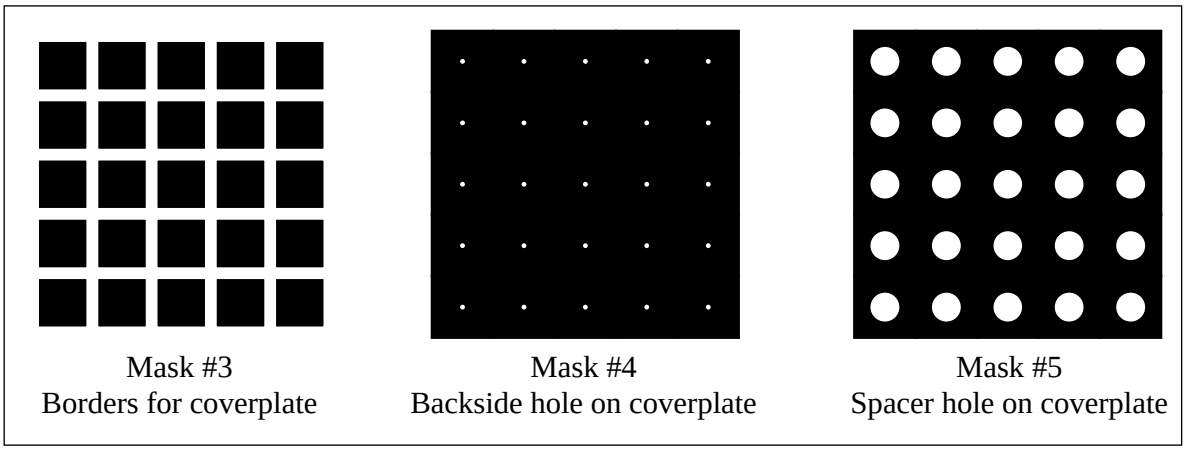

Figure 4.4 Masks used for Coverplate Chip

Once all of the mask patterns were drawn using the CAD package, the patterns were transferred onto blank masks with an Optical Pattern Generator. The fabricated masks were 125 mm X 125 mm glass chromium masks with a resolution of 0.6 μm.

4.1.2 Device Fabrication

Once the masks were produced they were used to transfer patterns onto the SOI wafers. The piston/diaphragm device was fabricated by spinning 1.6 μm of photoresist onto the base side of a wafer. Mask # 1 was used to expose the border pattern onto this photoresist using a contact aligner with a dose of 12.6 mW/cm^2 of UV light at 280 nm. Since this was the first pattern exposed, the mask was aligned to the primary flat. The photoresist was developed in MIF 300 for 60 s with high agitation.

The wafer was then placed inside of a DRIE chamber, and etched for a period of 60 s. The photoresist was dissolved in acetone and the wafer was cleaned. The depth of this etch was measured with a profilometer to be 3.5 μm. Regardless of the depth; however, this etch was clearly visible and could serve as a mark along which the wafer could be diced; which was the purpose of this feature.

The next step was to prepare the wafer for the deep etch. A different photoresist was used, which is much more viscous than the photoresist used for the first step. It was spun on at a speed of 2 000 RPM to leave a layer of 11.5 μm. Mask # 2 was aligned to the features left from the first DRIE with the MA6, and this photoresist was administered a dose of 390 mW/cm^2, then it was developed for 80 s in MIF 319.

The pattern from Mask#2 was ready to be etched into the wafer by the DRIE chamber. According to the tool's logbook, its selectivity had been repeatedly characterized to show that it etches silicon approximately 150 times faster than silicon dioxide and approximately 55 times faster than photoresist. The thickness of the photoresist was measured with the profilometer and was found as 11 μm; which is adequate since the desired etch depth was 450 μm.

The wafer was etched until silicon dioxide could be seen at the bottom of all etch pits, which took slightly longer than 3 hours (3:02:12). The end product can be seen below in Figure 4.5.

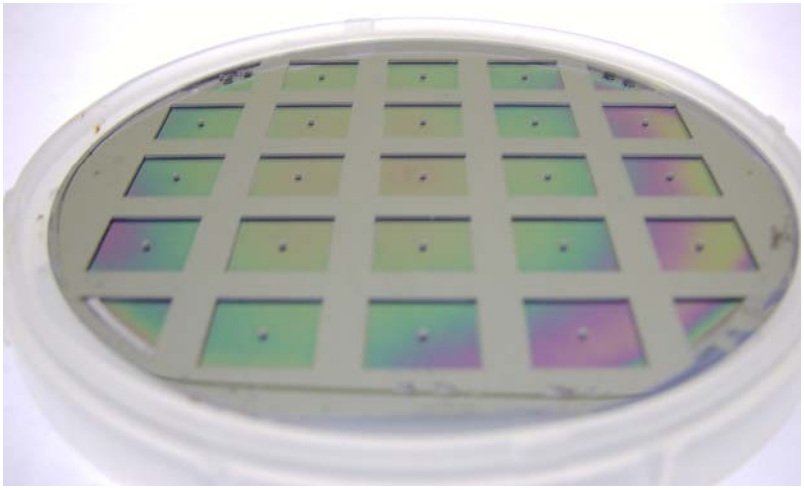

Figure 4.5 SOI Wafer after the Fabrication of Pistons and Diaphragms

The coverplate devices were fabricated next. A 1.6 μm layer of photoresist was spun onto the base side of the coverplate wafer, in the same manner as was done for the piston/diaphragm wafer. This photoresist was exposed with the contact aligner, using Mask # 3 and a dose of 12.6 mW/cm^2. It was then developed and etched in the DRIE chamber for a period of one minute.

The wafer was then cleaned and a layer of the same photoresist was spun onto the handle side. This layer was exposed using a back side contact aligner. This exposure system uses optical imaging to allow alignment with features on the back side of the wafer. With this tool, Mask # 4 was aligned to the features left from Mask # 3 on the opposite side of the wafer. The photoresist was exposed, developed, and etched in the DRIE chamber until the layer of buried silicon dioxide was exposed (20:08).

The wafer was then cleaned and an 11 μm layer of STR 1075 was spun onto the base side. It was exposed using the contact aligner with Mask # 5 and a dose of 390 mW/cm^2. The photoresist was developed and the wafer was etched in the DRIE chamber until the silicon dioxide was exposed in the bottom of the etch pit.

Once the fabrication of both wafers was complete, they were disassembled into the components. The wafers were diced by coating them with a very thick layer (approximately 1 mm thick from the deepest etched trenches) of photoresist. The photoresist provided an easily removable, thick, flexible layer which damped the vibrations that resulted from cutting the wafers. The wafers were then cut along the borders between the devices with a diamond-tip saw blade. After cutting the devices free from the wafers, they were soaked in acetone to remove the photoresist. Figure 4.6 shows photographs of the two chips after they have been cut from the wafers.

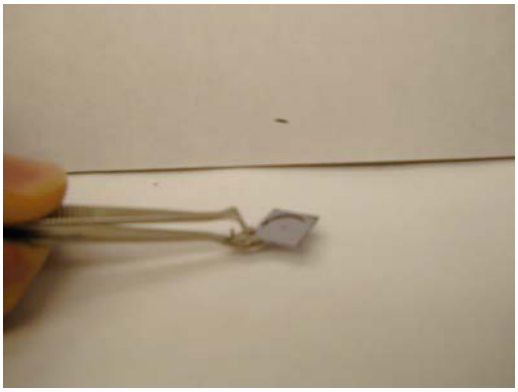

Figure 4.6a Coverplate Device

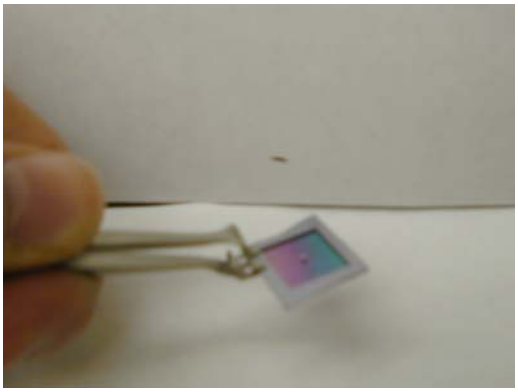

Figure 4.6b Piston/Diaphragm Device

The final fabrication step was to open the pass through hole in the coverplate device. The hole was blocked by a 1 μm thick layer of silicon dioxide. This layer of silicon dioxide was removed by dipping the device in a solution containing hydrofluoric acid (HF) for a few seconds until the SiO_2 was dissolved.

4.2 Assembly

At this point, one of each of the pieces was assembled into the first prototype. To do this, the two pieces were set together with an epoxy. This particular epoxy was formulated to work with refrigerants and was rated at pressures of up to 27.5 MPa. Figure 4.7 shows a photograph of the assembled devices.

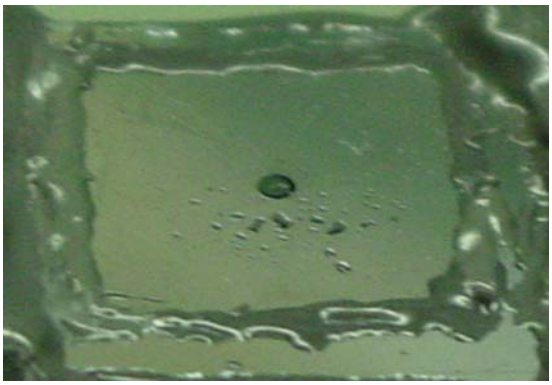

Figure 4.7 Assembled Device

Next, two small brass pieces were machined on a lathe. These pieces make up the small chamber that encapsulates the oil used to flex the membrane. The brass pieces were machined according to the specifications shown on Figures 4.8 and 4.9.

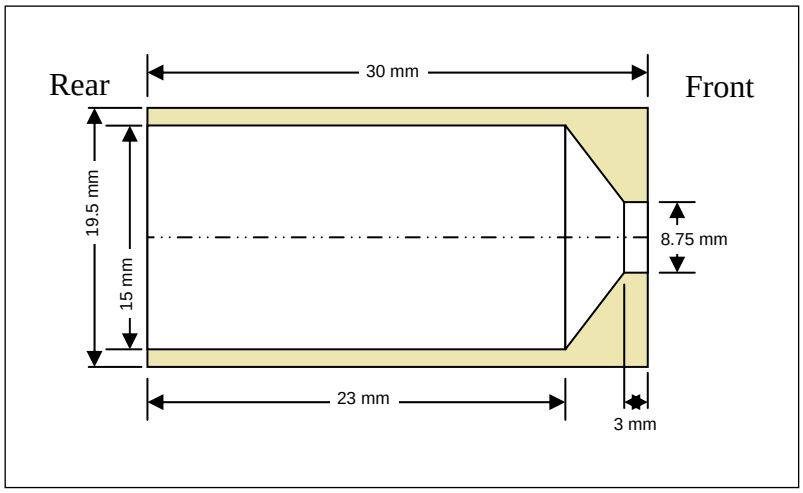

Figure 4.8 Specifications of Brass Capsule

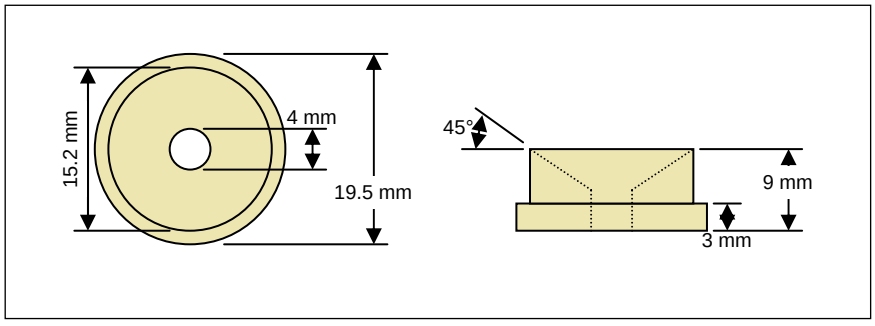

Figure 4.9 Specifications of Brass Capsule Cap

The devices were then mounted onto the brass capsule and secured with epoxy. A small 13.1 Ω electrical resistance heater was placed inside the capsule by running its wires through the cap and sealing the cap to the capsule.

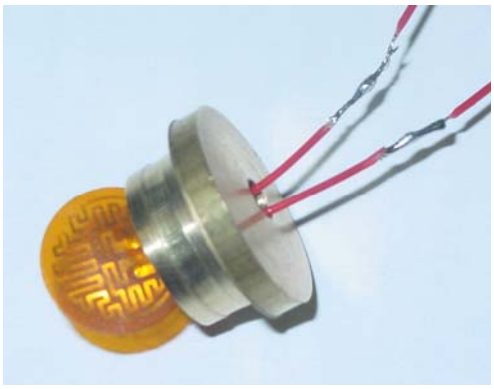

Figure 4.10 Heater and Cap Assembly

Next, the capsule was filled with polyalkalene glycol (PAG) 118 using a syringe. The capsule was filled with oil through the hole in the rear of the cap using 4.0 cm^3 of oil at a fill temperature of 22 °C. When the capsule was completely filled with oil, a type-T thermocouple probe was inserted through the hole and the capsule was sealed with epoxy. A picture of the final assembly is shown in Figure 4.11 below.

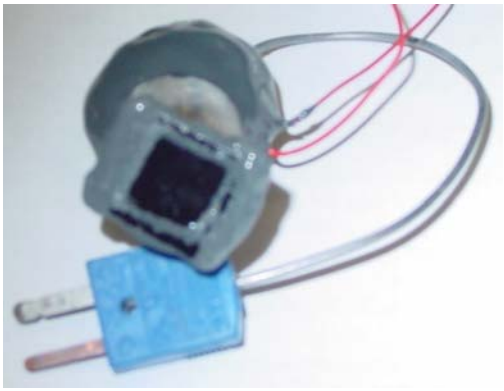

Figure 4.11 Final Assembly of Actuator

4.3 Characterization

Before measuring the movement of the piston, calculations were performed to estimate the displacement based on the oil temperature. This was done using the spreadsheet described earlier. The dimensions of the silicon pieces and brass oil reservoir were inserted into the spreadsheet along with the information regarding the oil in the capsule. Figure 4.12 depicts the prediction of the vertical movement of the piston in response to a changing oil temperature.

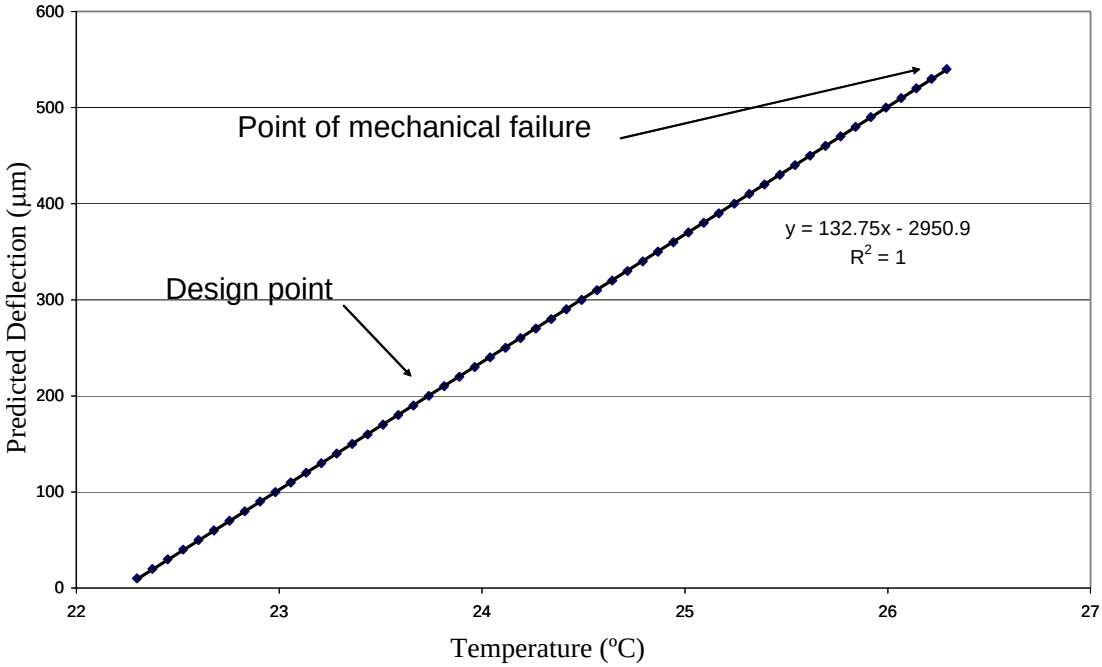

Figure 4.12 Performance Simulation for Displacement of Piston

The magnitude of the movement predicted by this model seems to be a little dangerous from a reliability point of view. The prediction is that, for a relatively small change in temperature (4.1 °C), the piston would move beyond its entire range of motion and the diaphragm would rupture.

There is, however, a major shortfall of the simulation model in that the epoxy holding the diaphragm to the oil reservoir has quite a bit of flexibility. As the pressure in the capsule increases, the epoxy will stretch and thus some of the additional volume in the capsule will be realized. There is, however, no means by which this amount may be accounted; therefore, it was left out of the simulations. This factor is helpful because it works to suppress the motion of the piston. If the motion is not as strong of a function of the oil temperature as predicted, the device will require a greater range of temperature to undergo this much motion; thereby making it easier to control. This is not an accident. The initial volume of the oil reservoir was determined through trial and error by noticing the effects of the epoxy and using a larger reservoir to attain the desired displacement.

The movement of the piston was then measured and correlated to the temperature of the oil in the capsule. For this measurement, the first step was to devise a method of measuring a small displacement that was perpendicular to the plane in which it may be viewed. The method used was to examine the device on a microscope, and focus the scope on a point on the piston. As the piston moved vertically, the focal point was tracked using the focus adjustment knob.

The focus adjustment knob on the microscope was divided by 100 tick marks per rotation. To obtain a conversion from these tick marks to actual distances, a calibration was performed. The profilometer measurements that were done on the piston/diaphragm chip verified that the distance from the top of the piston to the base was 450 μm; therefore, this chip was used as a reference for the calibration of the tick marks. Measurements from the bottom to

the top of the piston resulted in a conversion factor of 0.996 ticks/μm. This optical method can be used to distinguish features to within ± 10 μm.

The assembled device was then placed on the microscope stage. The heater wires were connected to a variable power source connected in parallel to a handheld multimeter. This allowed the voltage input to the heater to be controlled and monitored. The thermocouple which monitors the oil temperature was connected to a handheld thermocouple reader.

The position of the piston was recorded, along with temperature and voltage information, as heat was added to the capsule through the variable power source. The voltage was increased in small discrete increments with a minimum of 1 minute between readings. This allowed a range of data to be covered without capturing any transient effects. The temperature range that was used to collect data spanned the range between the ambient temperature in the laboratory and 32.2 °C.

Measurements were taken on three separate days; therefore, the starting point was not identical for each measurement. The position was recorded for each measurement and plotted as a position relative that at 23.9 °C. Figure 4.13 below shows the data taken on three separate occasions.

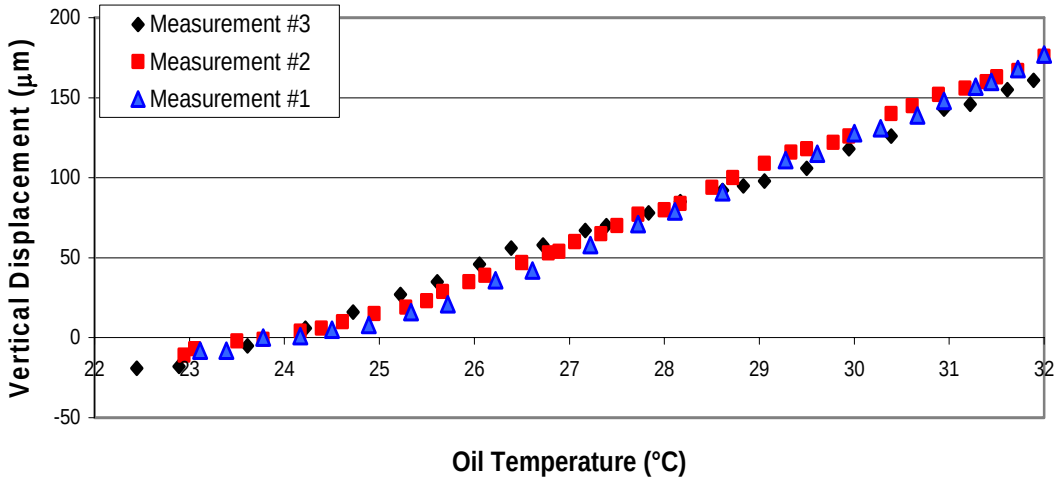

Figure 4.13 Characterization of Piston Displacement

This data demonstrated that the displacement of the piston was both linear and repeatable. The slope of a best fit line through all of the data points showed that the piston moved 20.98 μm/°C. This is much smaller of a slope that the 132.75 μm/°C predicted in the simulations; however, this is a reasonable expectation considering the effects of the epoxy's flexibility.

4.4 Attempted Testing in an R134a System

After the motion of the piston was characterized, installation and testing in the breadboard HVAC system was attempted. The device was mounted along a cut away section of a small gage tube and installed between the evaporator and condenser heat exchangers as the main pressure drop device in an R134a vapor compression cycle test apparatus.

A set of conditions were imposed on the cycle to represent the operating conditions of a household refrigerator. The temperature of the oil in the capsule was held at 23.9 °C while the

system parameters stabilized. Once steady state operation was achieved, the temperature of the oil in the capsule was elevated and the refrigeration cycle parameters were monitored. As heat was added into the capsule, it was expected that the piston would begin to obstruct the refrigerant flow path which would cause the mass flow to decrease, the liquid line pressure and temperature to increase, the evaporating temperature and pressure to decrease, and the capacity to decrease. None of this, unfortunately, occurred.

Once the oil temperature was raised to 29.4 °C, within the range of device characterization, the oil temperature began to decline very rapidly. A rapid decline in the oil temperature seemed to be the result of a ruptured diaphragm, which would allow refrigerant to mix directly with the oil in the capsule. This could occur if the piston was slightly misaligned with the tube to which it was mounted, and that the attempted actuation may have forced the piston into the tube wall. This would result in the piston being restrained, and eventually the rupturing of the diaphragm before any obstruction was introduced into the capillary tube. The device was removed from the system and examined. It was positioned with the tube in a vertical position, and oil droplets began to drip from the tube, indicating that the diaphragm had in fact ruptured.

4.5 Conclusions Drawn from Silicon Prototype

As this device was assembled from the last surviving set of silicon pieces, it was not possible to assemble and test another specimen. However, a lot of information was obtained through these tests, which is valuable for the second generation of such devices. The most important piece of information yielded from this experience is that such a device was possible to construct. Also, much of the knowledge gained through this fabrication and assembly may be carried over to the next generation of devices.

The first recommendation for design changes to the second generation of devices is to use a different material. The devices produced in this fabrication run were made out of silicon, which is a brittle material. This device can be made from silicon; however, at this stage of development it would be better to work with a more ductile material. Also, expensive processes and specialized wafers were needed to fabricate the features on these devices. Although the cost of fabrication of these parts may be feasible in large scale production, less expensive alternatives are possible if different materials are used.

The second recommendation is to change the design of the device so that the refrigerant flow path is fabricated as part of the device itself. This will eliminate any problems associated with trying to align the actuator to the refrigerant flow path, which is what ultimately caused the test specimen to fail in the HVAC system.

The third change is that the range of motion attainable by the piston should be larger and a higher factor of safety should be used. The features for this prototype were calculated based on the diaphragm experiencing a maximum stress equal to half of the yield stress when subject to a 200 μm extension and a large pressure differential occurring at its top. For the second generation, the minimum factor of safety will be doubled. Also, with the fabrication of the flow channel being part of the system, the range of motion of the piston will extend to the top of the flow channel. This will allow the device to completely stop the flow, rather than merely inducing more flow resistance.

Next, a different method of fixing the diaphragm to the oil reservoir is recommended. The epoxy used to hold the pieces together worked, but it had a large dampening effect on the

movement attainable by the piston due to its flexure. More importantly, a lot of difficulty was experienced with the epoxy in terms of containing the oil in the capsule.

Finally, an alternative method of benchmarking the performance of the device's ability to control fluid flow is desired. The reasons for this are explained in Chapter 3.

CHAPTER 5
Thick SU8-Nickel Micromolding Process

The second generation of the refrigerant expansion device is based on electroplating nickel into SU8 molds. There are many difficulties involved with working with SU8 in layers greater than 1 mm [29], the thickness necessitated by this design. In order to make this a viable option, extensive work was done to determine process parameters and tricks that would allow the formation of SU8 molds in excess of 1 mm.

The biggest problem that occurs in thick layer SU8 processing is that the material's stress becomes very large when it is cross linked [30-32]. This often causes the SU8 layer to buckle, shatter, or lose adhesion and detach from the substrate. As SU8 is deposited in thicker and thicker layers, the stresses generated during cross linkage become more pronounced and the likelihood of failure increases.

The available processing information from the manufacturer [33] gives detailed steps that instruct the user on how to build structures as tall as 260 μm. A manual [34] outlines a procedure for up to 430 μm tall SU8 layers. There is also a lot of information on the internet dedicated to the sharing of processing information of SU8 [35]. Many journal articles also share a lot of processing tips that help improve SU8 deposition [36-48]. These manuals and web sites often report conflicting information, but the suggestions provided were a good starting point. Very little, however, has been reported for thicker deposition of SU8. Researchers in Switzerland have successfully deposited and patterned SU8 in excess of 1200 μm [49, 50], and Sandia National Laboratory has published work showing deposition of up to 950 μm [51]; however, the recipes that they developed are proprietary and could not be obtained.

As an example, the process flow for 260 μm tall SU8-2100 features from the manufacturer's manual is described as follows:

1) Wafer pretreat: Whenever possible, the substrate should be undergo a piranha etch/clean (H2SO4 + H2O2); or at minimum a soak in isopropanol. Afterwards, a dehydration step is necessary, which typically consists of 5 min on a hot plate at 200 °C.

2) Coat: Liquid SU8 can easily be applied to a wafer through normal spin coating. However, SU8 is a very thick liquid (the kinematic viscosity of SU8-2100 at room temperature is 0.045 m^2/s, one order of magnitude greater than that of honey) and can be difficult to dispense. Therefore, it is typically poured directly onto the wafer rather than dispensed from a pipette. A spin rate of 1000 RPM will leave a layer of 260 μm on the wafer.

3) Soft bake: After the SU8 has been applied to the wafer; it must be heated to evaporate the solvent and solidify the SU8. Most photoresists achieve best results with this step performed in an oven, it has been widely reported that a hot plate soft bake is better for SU8. This is because an oven bake tends to form a crust on the SU8 surface, which will hinder the mass transfer of solvent out of the SU8. The wafer should be slowly ramped up and down from the soft bake temperature. The manufacturer states that the soft bake for a 260 μm layer requires 60 min on a hot plate at 95 °C, although other resources claim that as much as 5 h is necessary.

4) Exposure: A weak acid is formed when exposed to UV illumination. This acid reacts with the SU8 molecules and causes them to cross link and form a rigid polymer. Because of this mechanism, SU8 is relatively insensitive to overexposure. The exposure dose reported by manufacturer for a 260 μm layer is 400 mJ/cm^2, although other sources recommend a minimum of twice this dose and it has been reported the increasing the dose will typically result in better adhesion to the substrate.

5) Post Expose Bake: To promote the chemical reaction of the SU8 molecules cross linking, a post exposure bake is necessary. The manufacturer recommends a post exposure bake of 15 minutes on a 95 °C hot plate for a 260 μm layer. This can be a very tricky step because the SU8 begins to forms a high stress solid with a very large coefficient of thermal expansion once the molecules begin to cross link. The recommendation is to slowly ramp the temperature up and down to minimize the thermal gradients within the SU8, thereby reducing the stress caused by these thermal gradients.

6) Develop: SU8 is developed in a solution of PGMEA (propylene glycol methyl ether acetate). The developer dissolves SU8 that is not cross linked. It also seems to cause a high degree of stress in the SU8. For very thick layers, this is a very delicate step because the stress caused during the development can easily cause the SU8 to shatter. If this occurs, it will take place the instant that the very first drop of PGMEA comes into contact with the SU8; if there are no problems getting the wafer into the developer, catastrophic failure is not likely. The manufacturer recommends an agitated bath of PGMEA for 20 min to develop a layer of 260 μm thick.

7) Rinse: After the layer is developed, it should be rinsed in isopropanol. This also helps to determine if the development step is complete because undeveloped SU8 will form a milky residue if it comes into contact with isopropanol; therefore if this is present, it should be returned to the developer.

With the basic process steps outlined, substantial effort was put forth to fine tune this process so that it could be used in a process flow similar to LIGA. The basic process involves depositing and patterning SU8, and then filling in the cavities by electroplating a metal into it. Afterwards, the SU8 is removed and the metal structure is free. Figure 5.1 outlines the basic process flow.

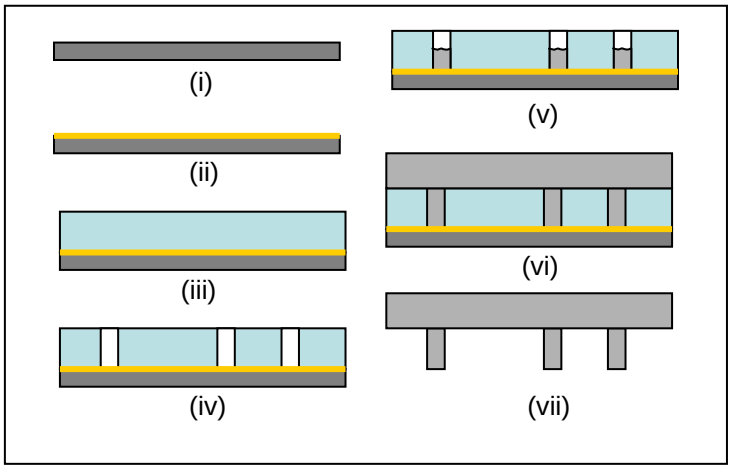

Figure 5.1 Basic Fabrication Process Goal for SU8

We begin with a clean substrate (i). Then it is coated with a layer of metal to be used as an electrical conductor for a plating base (ii). A thick layer of photoresist is deposited on top (iii), and then exposed and developed to leave the desired pattern (iv). Next, the substrate is submersed in an electrolyte solution with a mass of the plating metal. An electrical power source is connected to the plating metal (anode) and the plating base on the substrate (cathode) such that the plating metal undergoes oxidation:

$$Metal \rightarrow Metal^{n+} + ne^{-}$$

And metal is deposited on the cathode through reduction (iv):

$$Metal^{n+} + ne^{-} \rightarrow Metal$$

As the metal deposits, it will eventually grow out of the mold (vi). At this point, it may be polished to a desired level if required. Finally, the photoresist and the substrate are removed (vii) from the metal piece or pieces.

To build upon this basic process, there are a few obstacles to overcome. First, in order to fabricate the components that are required for this device, multiple layers must be deposited and patterned. With traditional LIGA, this is not a difficult task. The solution is simply to polish the deposited metal layer to the appropriate level, then repeat the process steps with a different pattern. This is not possible with thick SU8 photoresist because it has such a high stress and it does not have very good adhesion with metals, i.e. the subsequent layer of SU8 will not stick to the electroplated metal and will ultimately detach from the substrate entirely.

Also, if a thick (>500 μm) layer of SU8 is deposited onto a metal layer, it will often lose adhesion during electroplating. This doesn't seem to be much of a problem when a thin layer of SU8 is used; but the adhesion cannot overcome the stress associated with thick layers. Therefore, the SU8 can not be deposited on top of the plating base.

Another issue is that once a thick layer of SU8 is developed it is difficult, if not impossible, to deposit a second thick layer of SU8 on top. See Figure 5.2. The main reason for this is that SU8 contracts slightly when developed, which is a source of a great amount of tensile stress. The magnitude of this stress can be inferred from the curvature that is introduced to the substrate [52]. For SU8 layer thicknesses in the range of 1 mm, these stresses are on the order of 25 MPa to 30 MPa, which is close to the maximum stress for SU8 of 34 MPa [53]. If another thick layer is deposited on top of one which is already developed, then it is unlikely that the stack of SU8 will survive.

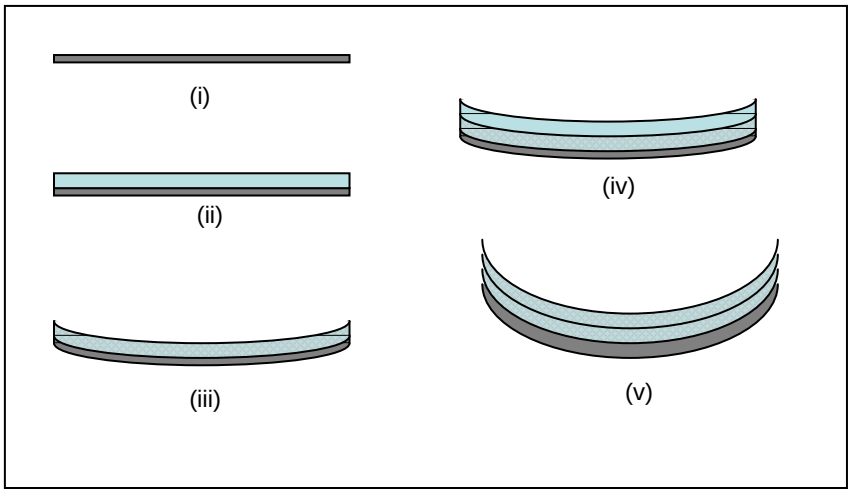

Figure 5.2 Buckling Mechanism for Multiple SU8 Layer Stacks. (i) Bare wafer. (ii) SU8 deposited on surface. (iii) SU8 developed. (iv) Second layer of SU8 deposited. (v) Second layer of SU8 developed.

A third issue is that SU8, when cured, is very resilient to chemicals. This makes it an excellent material for many applications where it is a permanent structure. However, removing

SU8 has proven to be very difficult. Recently, some researchers [54-56] have reported that SU8 can be etched by certain plasma or reactive ion etch (RIE) recipes; however, the results have shown etch rates between (1 and 4) μm per minute. With layer thicknesses of greater that 1 mm, these etch procedures would take an exceedingly long time and result in very expensive equipment usage. Similar etch rates have been found with wet etching techniques [57], and selectivity is an issue.

Given these constraints, modifications to the recipe were developed to fabricate devices > 1 mm out of nickel. First, the SU8 must be deposited onto bare silicon, instead of a metallic plating base as is common for traditional LIGA based processes. The adhesion between SU8 and silicon dioxide or metals is not as good as with silicon. It can be deposited onto many different materials, however, when the stresses become large, it will detach. SU8 adheres best to silicon; therefore, this offers the most protection against separation. For this reason, it is also necessary that the wafer be soaked in HF to remove any silicon dioxide.

Secondly, it is necessary to use either a thick wafer or multiple wafers bonded together. The large stresses cause significant wafer bowing. Using a thick wafer drastically reduces the amount of bowing, because the radius of curvature of the wafer is proportional to the square of the thickness. It has been found that a 100 mm diameter, 900 μm thick silicon wafer can withstand the stress induced by the deposition of 1200 μm of SU8 unlike a standard 500 μm wafer of this diameter.

Third, most of the stress occurs when SU8 reacts with PGMEA; therefore, all layers of SU8 must be developed in one single shot. Once thick layers of SU8 are deposited and developed, they are too unstable to undergo further processing (at least processes which introduce large stresses such as additional SU8 deposition). By developing all of the layers at once, the interstitial stresses between layers will be minimized.

In order to construct tall molds with varying features at different depths, the process steps 2-4 outlined in the beginning of this chapter (coat, pre-expose bake, expose) may be iterated. It is unnecessary to perform a post exposure bake (step 5) until after the final layer has been exposed. This is because each pre-expose bake for a subsequent layer will have the same effect. Also, it is not desirable to superfluously undergo additional thermal cycling.

In order to satisfy the single development rule, the geometry of the device itself is limited. The geometry must be constrained so that split-level features cannot include any overhangs. See Figure 5.3.

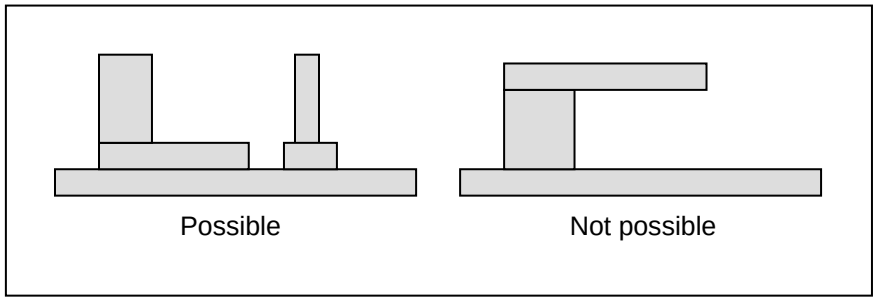

Figure 5.3 Geometrical Constraint for Nickel Device.

The reason for this constraint is that the SU8 molds must be made in such a way that every layer has a wider open area than the layer beneath it. This is because SU8 is a negative photoresist and it becomes a permanent structure when exposed to UV light. If a layer of SU8 is exposed, all layers directly beneath it will also receive UV radiation. Therefore, it is only possible to expose areas that lie directly on top of other exposed areas.

Researchers at the Swiss Federal Institute [58, 59] have developed three methods of forming overhangs and enclosed channels with SU8. Brief process flows are shown in Figures 5.4 - 5.6.

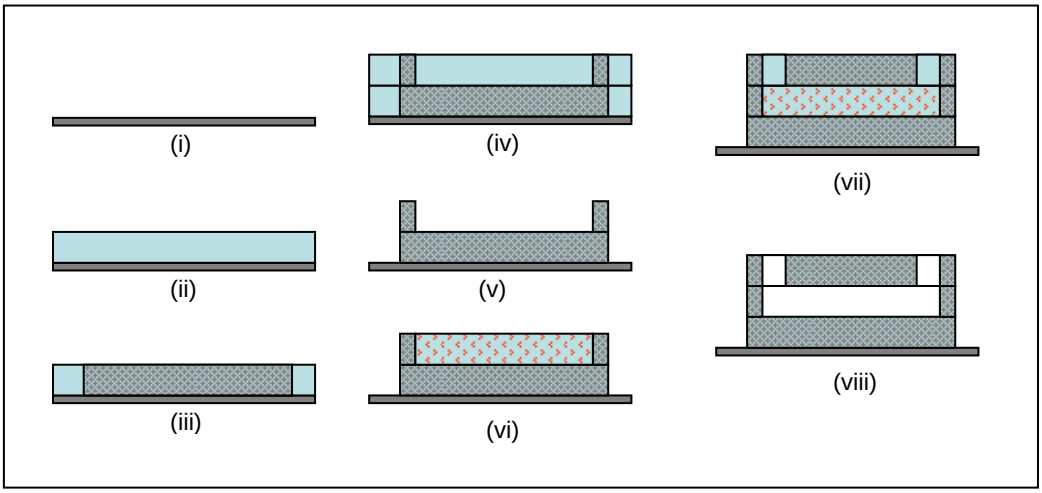

Figure 5.4 Fill Process for SU8 Overhangs or Channels

For the fill process, SU8 is deposited onto a substrate, patterned, and developed (i-v). Next, a sacrificial layer of dissolvable material is used to fill the trenches of the SU8 structures (vi). Another layer of SU8 is deposited on top of the stack, then it is exposed and developed, and the filler material is dissolved (vi-vii). This is not a feasible option for very thick layers because it involves multiple development steps.

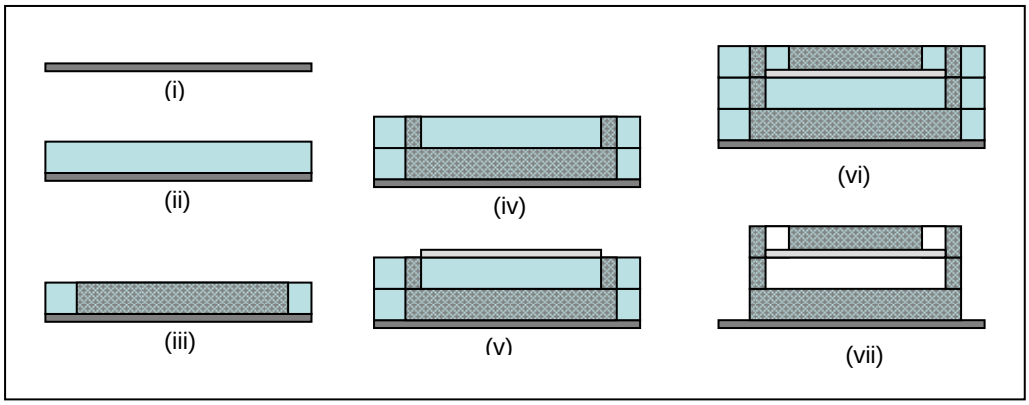

Figure 5.5 Mask Process for SU8 Overhangs or Channels

For the mask process, SU8 is deposited onto a substrate and patterned, but not developed (i-iv). Next, a layer of metal is deposited and patterned on top of the SU8 (v). This metal layer blocks the UV light from reacting with the unexposed SU8 beneath. Another layer of SU8 is deposited on top of the stack, and then exposed and all layers are developed (vi-vii). This is not a feasible option for very thick layers either because the high stress SU8 will not adhere to the metal layer.

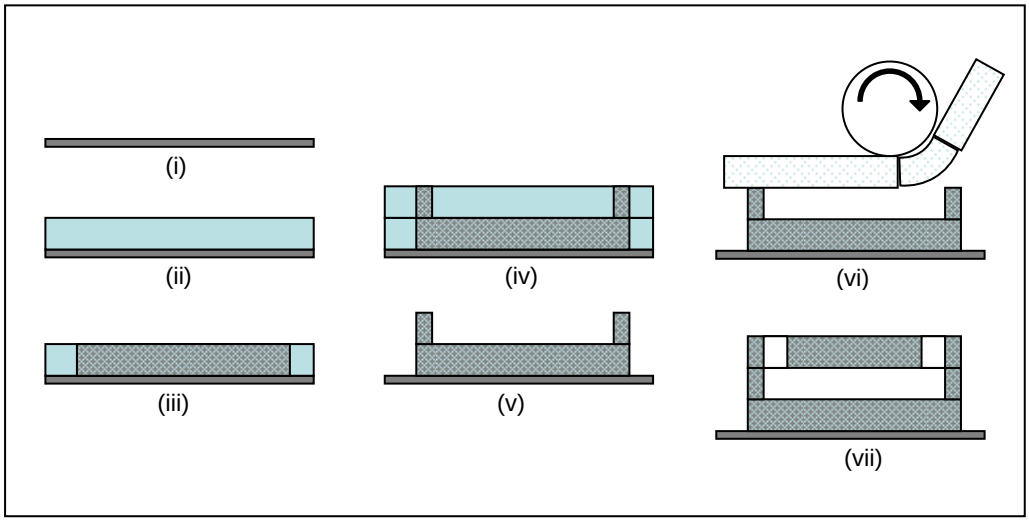

Figure 5.6 Lamination Process for SU8 Overhangs or Channels

For the lamination process, SU8 is deposited onto a substrate, patterned, and developed (i-v). Next, a layer of film laminate photoresist is deposited on top of the SU8 (vi). The laminate film is exposed and developed so that it forms the top portion of the structure or the overhangs (viii). Therefore, the structures are not completely made of SU8. This is a very useful process flow for fabricating microfluidic structures, but it has limitations for micromolding. The major limitation is that laminate photoresists have poor chemical resistance to electrolyte solutions, which are needed for electroplating. Therefore, the lamination process is not a feasible option either.

In order to deposit a metal with an electroplating process, a conductive layer must be present. Since SU8 cannot be deposited onto a metal, the metal must be deposited on top of the SU8 mold. Of the available methods for metal deposition, the process must have very good step

coverage to coat within the trenches of the molding. The simplest way to achieve the required metal deposition is by sputtering.

Finally, the last step requires that the metal devices are somehow freed from the SU8 molding. The easiest way to remove SU8 is to take advantage of SU8's instability and the fact that it does not exhibit the best adhesion to metal. The simplest method of pushing this material beyond its limit is to rapidly raise its temperature. This thermal shock causes the SU8 to lose adhesion to the metal, thus it can be easily removed. It has been found through experience that if the substrate is placed on a 500 °C hotplate, the metal will be ejected from the SU8 within 5 s to 10 s while it is still cold to touch. The SU8 is destroyed during this process, but the silicon wafer is left in tact. This is quite beneficial because the wafer may be polished, cleaned, and used again.

In order to use this method, an additional layer of SU8 is needed to completely cover the substrate. This sacrificial layer of SU8 is required so that the metal is fixed only to SU8 and not to the substrate. Therefore the metal is not restrained to the wafer while the SU8 is attempting to eject it.

All of the rules outlined thus far are necessary to successfully deposit layers of SU8 in excess of 1 mm total thickness. However, following these steps alone does not result in a good pattern transfer, and additional fabrication steps are necessary to deposit a thick layer of SU8 with good uniformity. This is because the edge bead resulting from the fabrication process outlined is extraordinarily large. It is impossible to accurately measure the magnitude of this problem because no good tool for this measurement exists.

In order to gauge the magnitude of the problem, a layer of 500 μm of SU8 was deposited onto a wafer prepared using the method outlined thus far. Calipers were used to measure the thickness of a layer of SU8 and wafer in a few locations, although it was impossible to reach to the center of the wafer with the calipers. In general, using the 500 μm recipe would result in an outer ridge-edge bead thickness of approximately 500 μm. However, this ridge is generally 2 cm to 3 cm wide, and the thickness of the SU8 inside the bead is much smaller; typically 100 μm to 150 μm. A typical pattern is shown below in Figure 5.7.

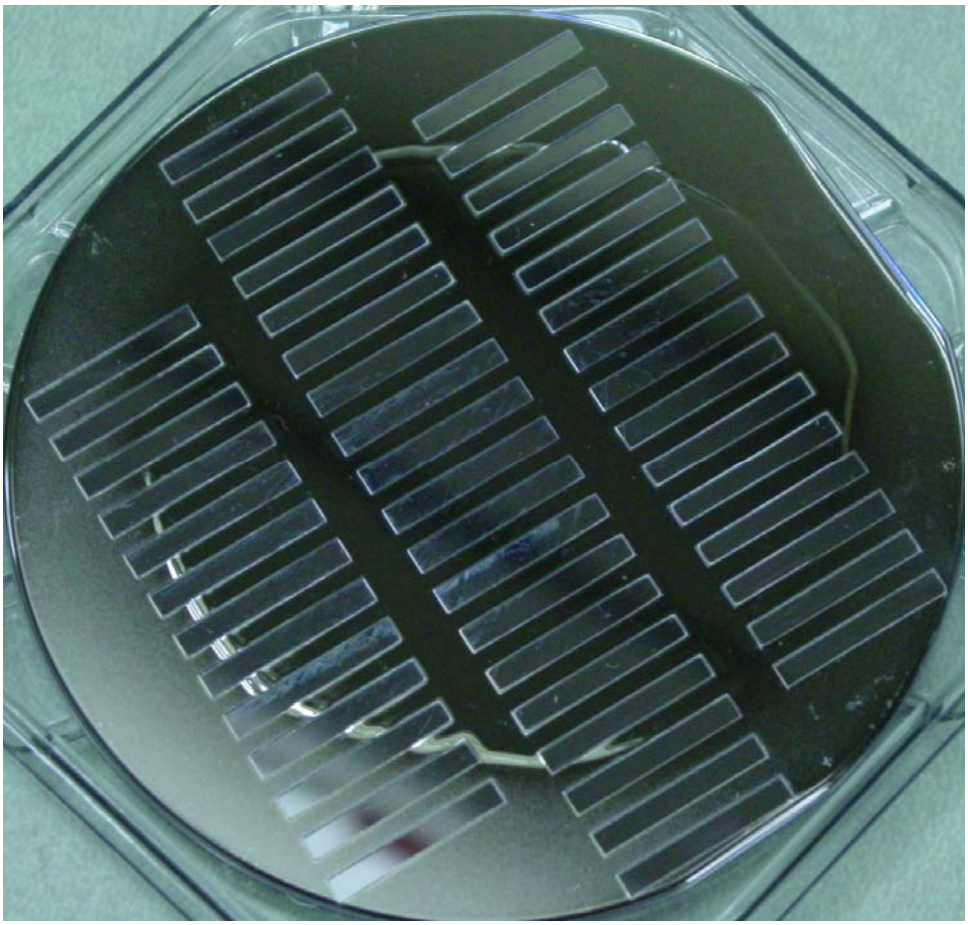

Figure 5.7 Typical Thick Layer SU8 Edge Bead Distortion

This is quite problematic not only because any resulting structure height is greatly altered; but because light passing through a mask placed on top of this will scatter terribly, resulting in a very poor pattern transfer. Furthermore, any subsequent fabrication steps will be distorted because this layer will be uneven.

Eliminating this edge bead, and the problems caused by it, is a rather challenging task. Conventional edge bead removal is generally performed by treating the photoresist near the edge with a solvent. This will not work with SU8 because it is a negative photoresist. Grinding the SU8 edge bead to the correct thickness is not a feasible option either because in order to do this, the SU8 layer must be developed and it was found that, once developed, thick SU8 cannot withstand further processing.

After trying a few different options, a procedural modification was devised which resulted in much more uniform SU8 deposition. The additional fabrication steps to deposit one layer of thick SU8 are outlined in Figures 5.8 and 5.9.

Initially, the SU8 is deposited onto a wafer using the guidelines set forth thus far. The bare wafer 5.8 (a) is cleaned, then SU8 is spun onto the wafer according to the spin-spread rates at a given temperature and the wafer undergoes a soft bake to drive off the solvents. This results in a deposition pattern similar to that shown in Figure 5.8 (b). After the soft bake, a mask is placed over the wafer and held in contact. A region that is not in contact with the mask is clearly visible through the mask at this point 5.8 (c). Once the mask and the wafer are secured together, an opaque layer of black electrical tape is used to cover all parts of the mask that lie directly

above areas that are not in contact with the SU8 5.8 (d). Next, the SU8 is exposed through the mask/black tape assembly.

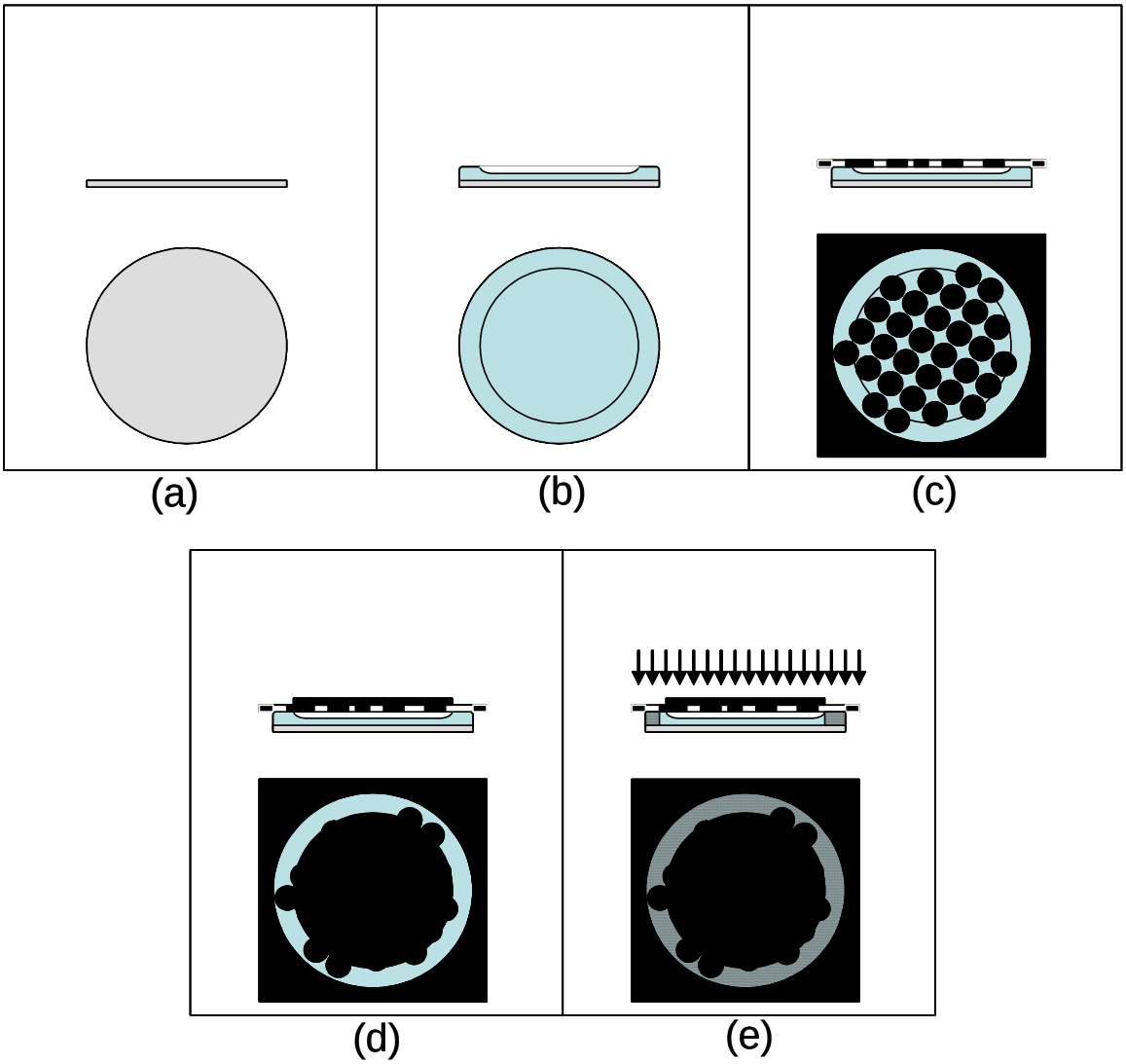

Figure 5.8 Process Steps to Eliminate Edge Bead

At this point, the form of the SU8 that remains on the wafer is that of an exposed ridge, of appropriate thickness, with a thin, unexposed area in the middle, 5.9 (a). Next, a small puddle of SU8 in a less viscous formulation, SU8-2025, is placed in the center of this area 5.9 (b). It is important that no air bubbles are entrained in the SU8-2025 in this step. Next, this puddle is spread out evenly over the surface of the wafer, using a glass plate or another object that is smooth and long enough to span across the entire wafer 5.9 (c). At this point, the exposed SU8 is in the shape of a dish which contains a puddle of liquid, low viscosity SU8-2025. The wafer is then placed flat in an oven at a low baking temperature for a long period of time to allow the solvents to be expelled from the SU8-2025; 75 ºC for a period of 15 h to 16 h works well.

When it is removed from the oven, the thickness of the SU8 is fairly constant across the surface of the wafer. At this point, the remaining portions of the SU8 need to be exposed to a dose of UV radiation. The mask is realigned to the pattern left from the first exposure, except

this time there is no black tape on the mask. The SU8 is given a dose of UV radiation, Figure 5.9 (e), and then undergoes its post expose bake.

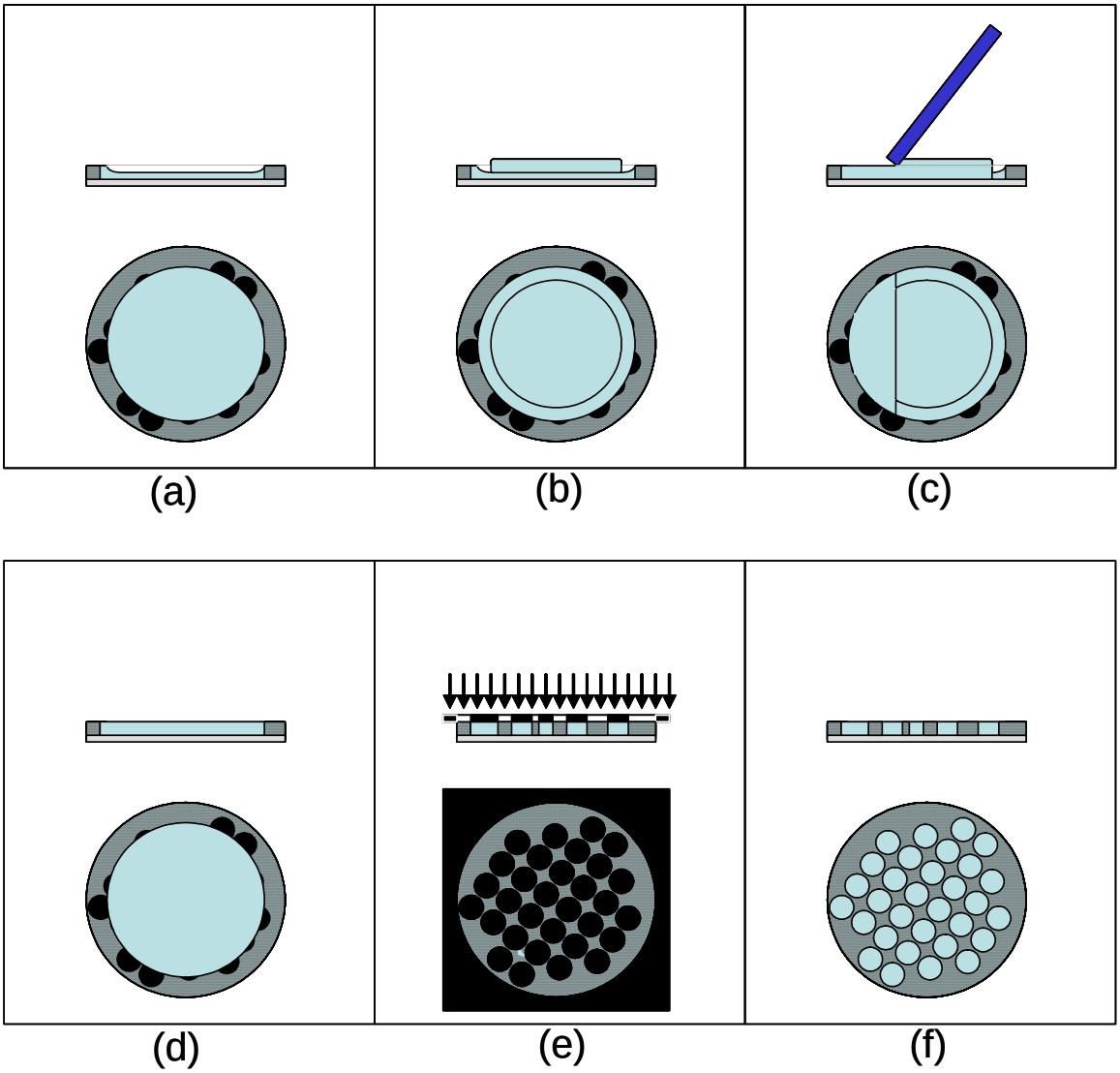

Figure 5.9. Process Steps to Eliminate Edge Bead Continued

Altogether, these additional process steps roughly double the total amount of bake time needed to process a wafer, but the resulting pattern transfer and the yield are far superior to those fabricated without these additional steps. A typical product of thick layer SU8 deposition using these additional fabrication steps is shown below in Figure 5.10.

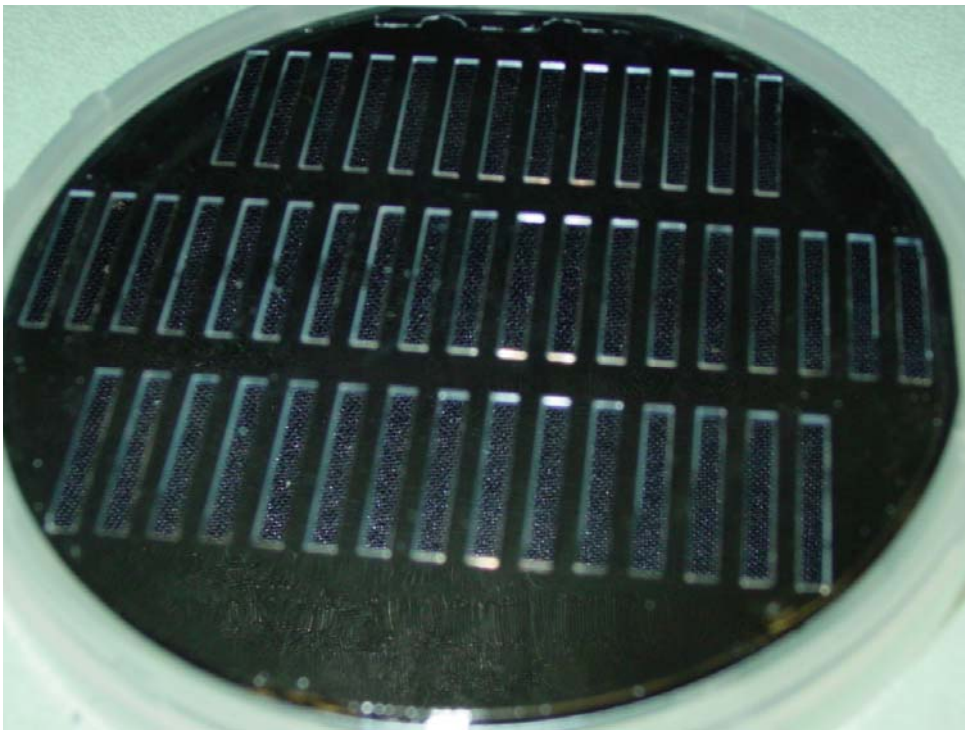

Figure 5.10 Typical Thick Layer SU8 Deposition Using Additional Fabrication Steps

CHAPTER 6
SU8 Nickel Micromolded Device

In the previous chapters, processes have been developed that will allow the fabrication of the refrigerant expansion device out of a metal using SU8 micromolds. Based on the findings of the device fabricated with DRIE and the limitations of SU8 micromolding, a number of changes were incorporated into this new design.

6.1 New Design

Nickel was selected as a new material because it is an easy metal to use for thick layer electroplating and it is substantially more ductile than silicon, which lowers the risk of catastrophic failure in a harsh environment. The electrodeposition method used to deposit nickel in this manner is also much less expensive than the fabrication techniques required to construct similar features from silicon. The most significant change to the design of the device is that the refrigerant flow passage is now incorporated directly into the device. This change eliminates many of the problems that occur during device assembly.

As a consequence of the design and fabrication process changes, the new design must be fabricated in three pieces, the diaphragm/piston section, the flow channel section, and the flow channel cap section.

The diaphragm/piston section is comprised of a thin circular membrane with a cylindrical piston located in its center and a ring on its perimeter to add stability. A sketch of this piece is shown in Figure 6.1.

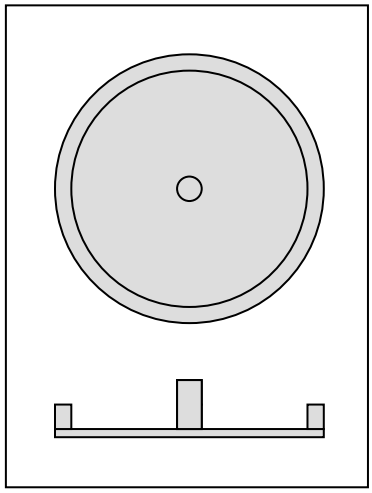

Figure 6.1 Sketch of Piston/Diaphragm Piece

Next, the flow channel section is comprised of a flat, circular mass of material with a pass through hole in the center. On one side of this piece are two vertical walls, separated by a gap such that they lie on either side of the pass through hole. These walls and the portion of the disk that lies between them make up the bottom and sides of the refrigerant flow passage. The flow passage extends a short distance beyond the perimeter of the circular disk so that connections to fluidic conduits may be made later. A sketch of the flow channel section piece is shown in Figure 6.2.

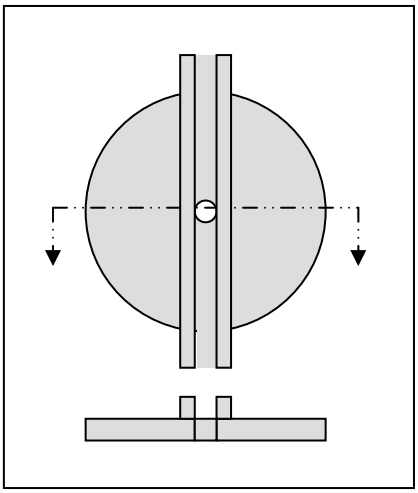

Figure 6.2 Sketch of Flow Channel Piece

The third piece is the flow channel cap section which is simply a piece of material that seals the top of the refrigerant flow channel. This piece is comprised of a section which spans the length of the flow channel and contains a wall on either side to clasp onto the channel. A sketch of this piece is shown in Figure 6.3.

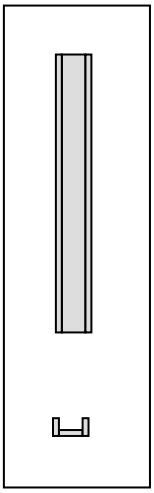

Figure 6.3 Sketch of Flow Channel Cap Piece

The three pieces are assembled as shown in Figure 6.4.

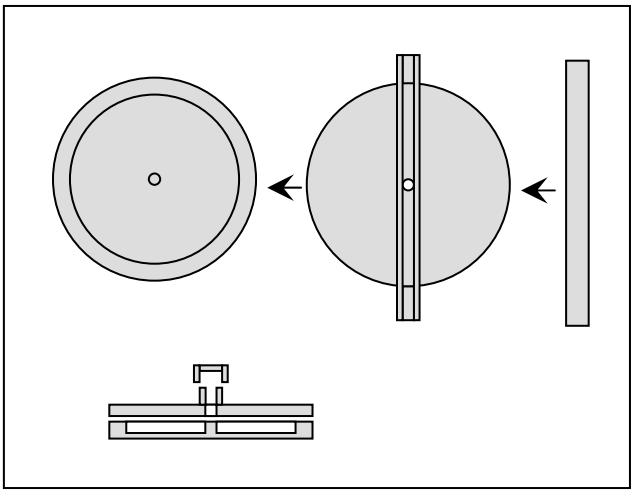

Figure 6.4 Assembly of the Micromolded Pieces

The first step to fabricating these pieces is to calculate the dimensions that are required to allow the device to operate through its desired range of motion. The flow channel was designed to be of rectangular cross section with a height of 500 μm and a width of 1 000 μm. In order to close off this channel, the piston must have a 500 μm range of motion.

A spreadsheet, similar to that generated for the silicon prototype, was created to calculate the required dimensions of the nickel pieces. The mechanical properties of electroplated nickel were acquired from [60]. Young's modulus and the yield strength of electroplated nickel were found to be substantially different from cast nickel, and these properties are also affected by the current density used during the electrodeposition. The properties used for this analysis corresponded to a current density of 12.7 mA/cm^2, which is equivalent to a current of 1 A over the surface area of a 100 mm diameter wafer. The value of Poisson's ratio was taken to be 0.31 [61]. The values used for this analysis are:

E = 18.8 GPa
σ_y = 770 MPa

The calculations detailed in section 5 of this report were repeated with these material properties. The radius of the diaphragm was chosen to be 6 200 μm and the selected thickness was 150 μm. The required deflection of 500 μm was held constant on this spreadsheet, as this was the minimum acceptable height of the refrigerant flow channel, and it is desired to ultimately close this channel with the piston. These dimensions result in a factor of safety of 3.5.

6.2 Fabrication

The three pieces which make up the device were fabricated using the nickel micromolding procedure. A total of 7 photolithography masks were created for the three pieces. The masks used for this work were produced by high resolution (5 080 dpi) printing of the mask layers onto transparency film.

The diaphragm/piston piece was fabricated in the following manner. This device has three distinct layers; therefore, it required a three-mask process. The first mask defines the top half of the piston; the second mask defines the bottom half of the piston and the ring attached to the perimeter of the diaphragm; and the third mask defines the diaphragm. Since SU8 is a

negative tone photoresist, the final pieces that are to be formed of metal were drawn as dark fields on the photolithography masks. An array of 31 identical devices was able to fit onto each mask, given the dimensions of the features. Drawings of the three masks used to fabricate the molds for this piece are shown in Figure 6.5.

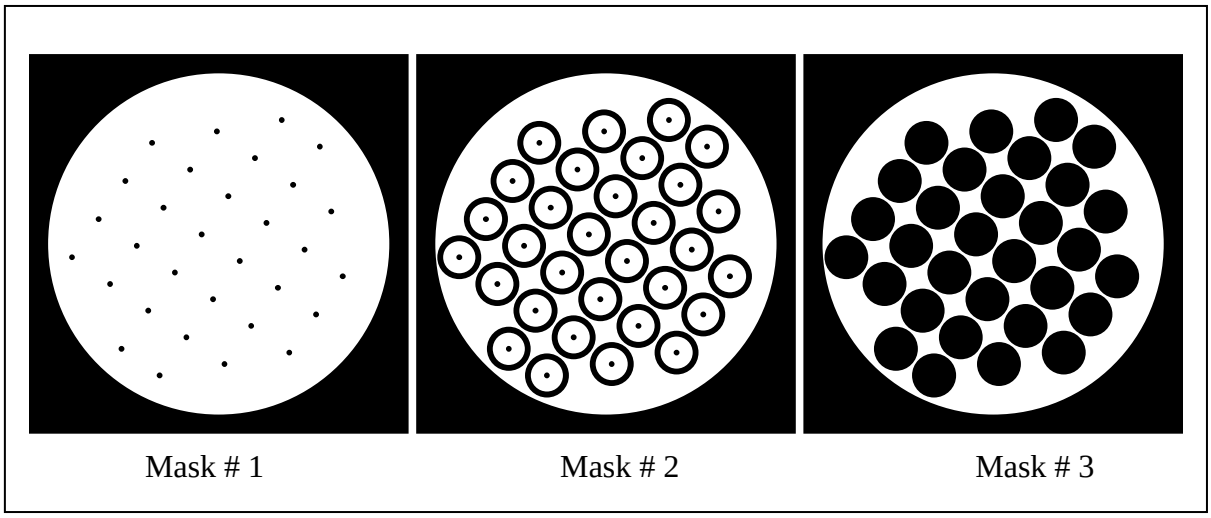

Figure 6.5 Masks used to Fabricate Molds for Piston/Diaphragm Piece

The flow channel piece and the flow channel cap piece each contain two distinct layers; therefore, a two-mask process is required to fabricate these molds. The masks for the flow channel piece are shown in Figure 6.6. Using this arrangement an array of 31 devices was able to fit on each mask. The mask designated Mask # 4 defines the area which sits atop the diaphragm/piston piece, with a small opening in the center to define the pass through. Mask # 5 defines the area which will make up the side walls of the refrigerant flow passage.

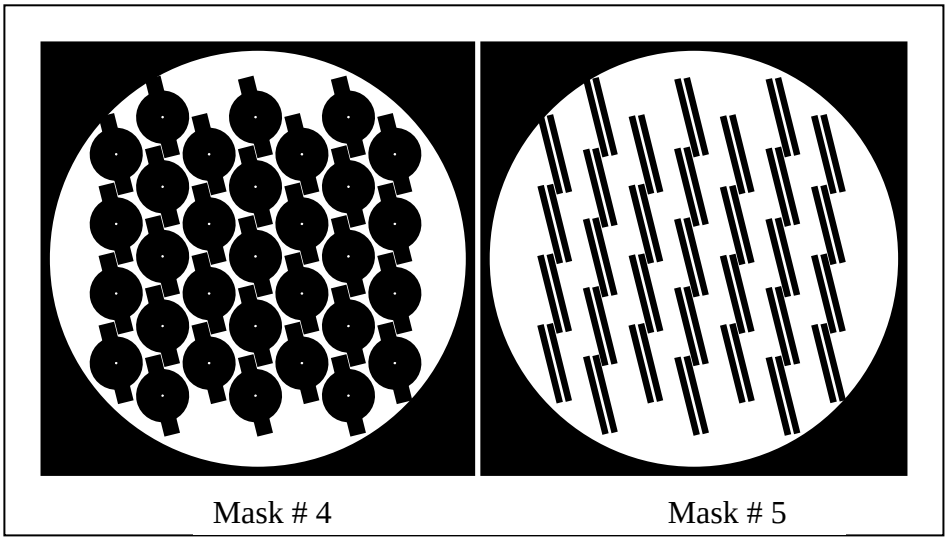

Figure 6.6 Masks used to Fabricate Molds for Flow Channel Piece

The masks needed to fabricate the flow channel cap piece are shown Figure 6.7. The area needed to fabricate this piece is significantly less than the other pieces; therefore, more of them

can be made during a process run. Using this arrangement an array of 47 devices was able to fit on each mask. The mask designated Mask # 6 defines the walls of the flow channel cap. Mask # 7 defines the area which will seal the top of the refrigerant flow passage.

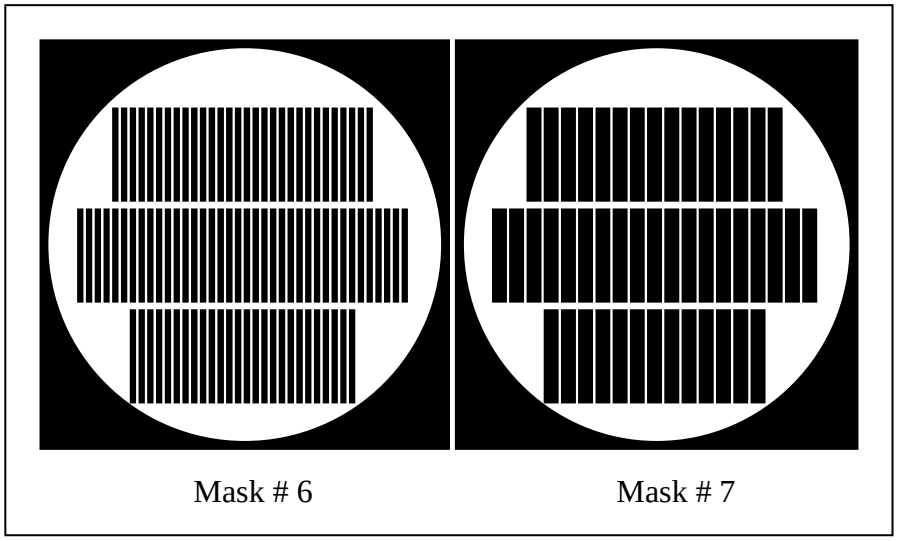

Figure 6.7 Masks used to Fabricate Molds for Flow Channel Cap Piece

In the following recipes, all liquid SU8 was brought to a temperature of 25 ºC prior to dispensing onto the wafers. Also, all temperature changes imposed on the wafer (baking ramp-up and cool-down) were done at a rate of 0.2 ºC/s or less to avoid problems with rapid temperature change. The process flow for this device began with soaking 900 μm thick silicon wafers in hydrofluoric acid for 10 min to remove any silicon dioxide. The wafers were then rinsed with de-ionized water and allowed to dehydrate on a hot plate for 30 min at 120 °C. Figure 6.8 depicts the process flow for fabricating the molding for the piston/diaphragm pieces. A 40 μm thick layer of SU8-2025 was spun onto the wafer at 2 000 RPM, soft baked for 10 min on a level hot plate at 95 ºC, and flood exposed with 1.77 J/cm^2 of UV radiation with no mask (i). This step coated the entire wafer with a 40 μm thick layer of cross linked SU8 so that the metal layers (to be deposited later) will not contact the silicon and can be easily removed.

After the "sacrificial" layer of SU8 was deposited, a layer of SU8-2100 was spun onto the wafer at 1 000 RPM, and soft baked (soft bake # 2) at 95 ºC for 1 h, to deposit a 250 μm thick ridge of SU8 onto the wafer. After soft bake # 2, the spin on process (SU8-2100 at 1000 RPM) was repeated, and the wafer was soft baked again (soft bake # 3) at 95 ºC for 1 h.

At this point, the wafer was covered with an exposed 40 μm layer of SU8. On top of this was an unexposed layer of SU8, with a thickness of 500 μm near the outer edge and much thinner near the center (ii). The wafer was sandwiched between Mask # 1 and a glass plate. The two glass plates were held in together using 8 binder clips along their outer edge. Upon securing the clips, a clearly visible distinction could be made between SU8 in contact with the mask and the areas where SU8 was not in contact with the mask (iii). Opaque, black electrical tape was placed over the areas where the SU8 was not in contact with the mask, so that only the thicker, outer edge of the SU8 could be seen through the mask (iv). A dose of 5.4 J/cm^2 was administered to the SU8 on the wafer (v). Next, the mask was removed and a puddle of low viscosity SU8-2025 was placed in the center of the wafer (vi). The SU8-2025 was then smoothed into place using a glass plate (vii) and placed into a low temperature oven at 75 ºC for

18 h. Upon removing the wafer from the oven, it could be seen that the resulting layer of SU8 was level. The wafer was once again sandwiched between Mask # 1 and a glass plate, using 8 binder clips. This time, the Mask # 1 was aligned to the previous exposure, and no black tape was necessary because all of the SU8 was seen to be in contact with the mask. The wafer was then given a 5.4 J/cm^2 dose of ultraviolet radiation (viii). This completed the patterning of the first 500 μm thick layer of the micromold (ix).

Next, fabrication steps (ii) through (viii) were repeated using Mask # 2 (x). This time, Mask # 2 was aligned to the features left by Mask # 1 for the first exposure (with black tape), and to the features left by itself for the second exposure. This completed the patterning of the second 500 μm thick layer of the micromold.

Finally, a layer of SU8-2100 was spun onto the wafer at 1 850 RPM, corresponding to a thickness of 150 μm. The wafer was then soft baked at 95 ºC for 35 min. Following the soft bake, the wafer was sandwiched between Mask # 3 and a glass plate, black tape was placed over the non-contact areas, and the wafer was given a dose of 3.3 J/cm^2. The wafer was then filled in with SU8-2025 in the same manner and placed in an oven overnight for 24 h at 75 ºC. The wafer was then realigned to Mask # 3 and administered the same dose of 3.3 J/cm^2 (xi), and placed back into the oven at 75 ºC for 19 h. This completed the final lithography step for the mold fabrication.

The wafer was then developed in PGMEA. Development of molds this tall is a very slow process as well. The wafers were submerged in PGMEA and agitated. The progress was periodically checked with isopropyl alcohol and the developer solution was changed every 20 min. During this process run, development took approximately 1 h and 20 min (xii).

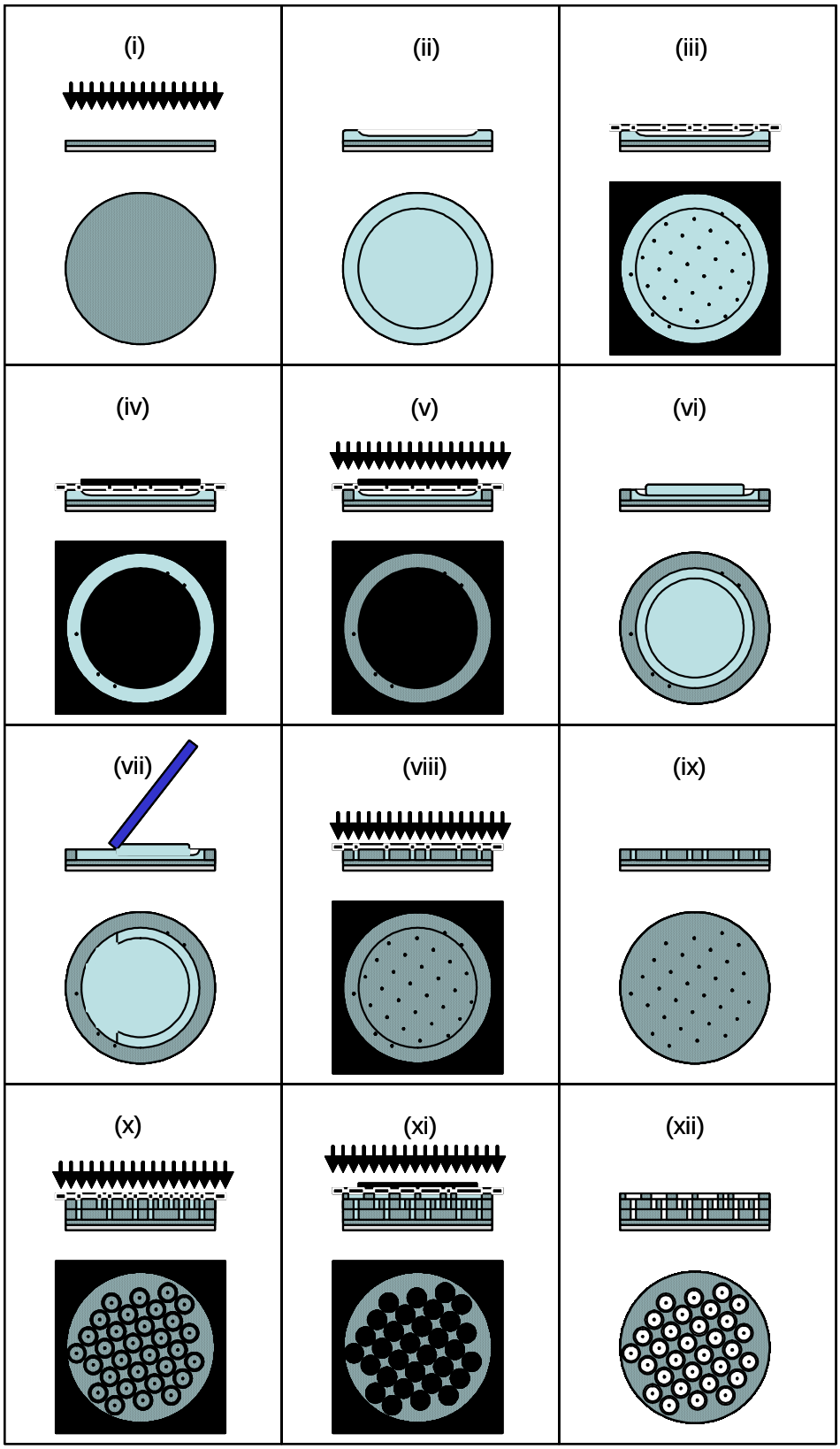

Figure 6.8 Process Flow for Fabrication of Piston/Diaphragm Molding

The same process was used to fabricate the flow channel pieces and the flow channel cap pieces with the exception that the top layer (step xi) was not needed for these devices as they are two-layer devices. The other difference is that these two wafers were given a slightly longer post exposure bake of 24.5 h.

Once the molding was completed, a 4800 $\mathring{A}$ layer of gold was sputtered over the entire surface of the cross linked SU8. Gold was selected for this purpose because it is a good electrical conductor and its deposition rate through sputtering is very fast in comparison to other metals (approximately 500 $\mathring{A}$/min). Also, it has been noted that gold has the worst adhesion to SU8; therefore, it will make it easier to eject the fabricated parts from the SU8 molds.

The next step was to deposit nickel into the molding. A large beaker containing a solution of 51 % nickel sulfamate was warmed to 65 °C on a hot plate. The wafer containing the molding was placed in the beaker along with a 100 mm X 150 mm X 3 mm strip of alloy 200 nickel (>99.5 % Ni). Electrical wires were secured to the nickel strip and to the gold layer with alligator clips. These wires were connected to a DC power supply as shown in Figure 6.9.

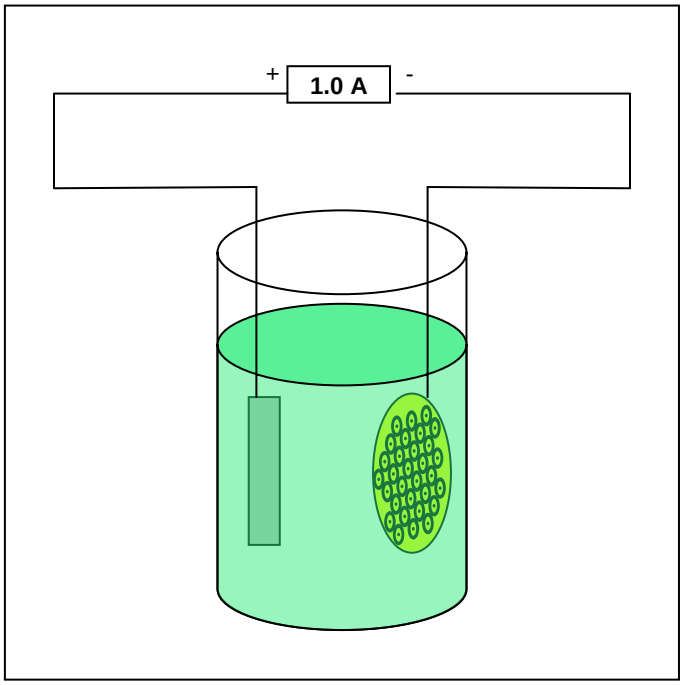

Figure 6.9 Electroplating Apparatus

A steady DC current of 1.0 A was held between the base plate and wafer. An estimate of the time required to fill the molds was calculated at this current for the piston/diaphragm piece. The estimate was based on assumptions that the volume of nickel transferred from the anode to the cathode was equivalent to 1 150 μm in thickness over the entire surface of the wafer, that 2 electrons were transferred through the power source in order to deposit each atom of nickel, and the atomic packing density of nickel (face centered cubic) is 74 %. The resulting estimate showed it would take 73.5 h of electroplating to fill the molds; therefore, the electroplating process was run for 91 h to ensure that enough nickel had been deposited. Similarly, estimated electroplating times were calculated for the flow channel piece and the flow channel cap piece based on a 1 000 μm thick layer deposition. It was estimated that these devices would take

approximately 64 h to electroplate at a current of 1 A; therefore, the process was performed for 80 h.

After the molds had been filled, the nickel was polished down until SU8 was exposed. At this point, the nickel devices were removed from the mold by placing the wafer on a 500 °C hot plate for 10 s. This thermal shock caused the SU8 to fracture and eject the nickel pieces.

6.3 Feature Characterization

The features of the micromolded pieces were measured and compared to expectations. A general observation about the SU8 molding is that the effects of edge beading were vastly improved by the additional fabrication steps. For this fabrication run, the yield of usable product was generally around 70 %. The exact tolerances of the best pieces were generally good; the main hindrance to better pattern transfer was the number of exposure alignments. This can, however, be improved by using proper alignment equipment in the future; although, it may not be necessary for many applications.

Since this fabrication process is experimental, each piece is inherently unique. Therefore for the sake of brevity, a full characterization of only one of each of the pieces that were assembled to form the device will be presented in this section. Obviously the best devices on each wafer were used for the assembly; therefore, this section does not represent the characterization of the average device on the wafer. The features fabricated during this process run are larger than what can be measured using a profilometer; therefore, although less accurate, a micrometer was used to measure most of the results. The accuracy of the micrometer was +/- 3 μm. Features that are not measurable with a micrometer due to their geometry or orientation were characterized using the microscope focus dial method.

6.3.1 Piston/Diaphragm Piece

Figure 6.10 shows a photograph of the top of a piston. The intended geometry of the piston was to be that of a cylinder 1 000 μm tall, with a diameter of 950 μm. The diameter at the top of the post measured 900 μm and 913 μm along two different chords. The red circle shown on this figure outlines the intended feature geometry.

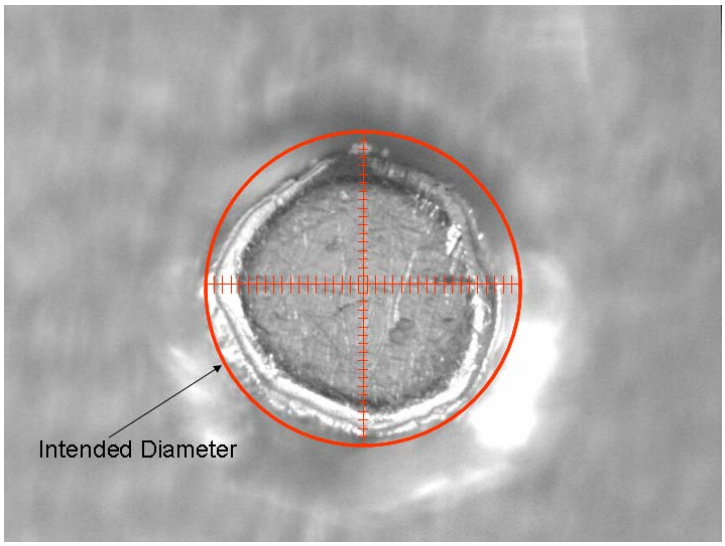

Figure 6.10 Characterization Photograph: Top of Piston

It can be seen from this photograph that the opening in the SU8 mold was slightly larger than intended. This is because SU8 is a negative type photoresist, and any misalignment or scattering will result in areas near the dark fields receiving some UV radiation. Also, there is some difficulty developing the SU8 near the bottom of the trenches, which correspond to features at the top of the piston. Since the edges at the bottom of the SU8 trenches are sharp internal corners, it is difficult to dissolve and remove all of the unexposed SU8. This results in rounded edges near the top of the micromolded features. Figure 6.11 is a photograph of the piston, taken from an angle to show the profile.

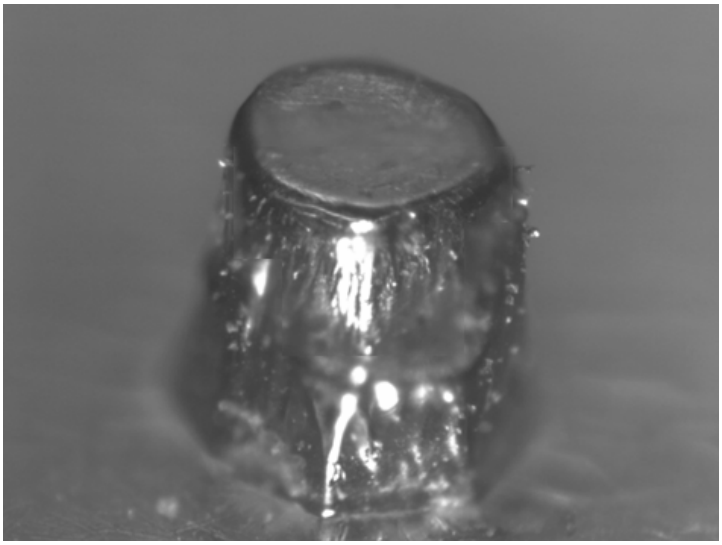

Figure 6.11 Side Profile of Piston

The figure shows that the top of the piston is slightly thinner than the bottom, and that the edges are rounder near the top of the piston. Notice that the orthogonal geometry near the bottom of the piston gives way to a smooth section near the top.

The next feature of this device to be analyzed is the ridge which stabilizes the perimeter of the diaphragm. The ridge was intended to be 500 μm in width and 500 μm tall. Measurements were taken around the ridge at the locations shown in Figure 6.12.

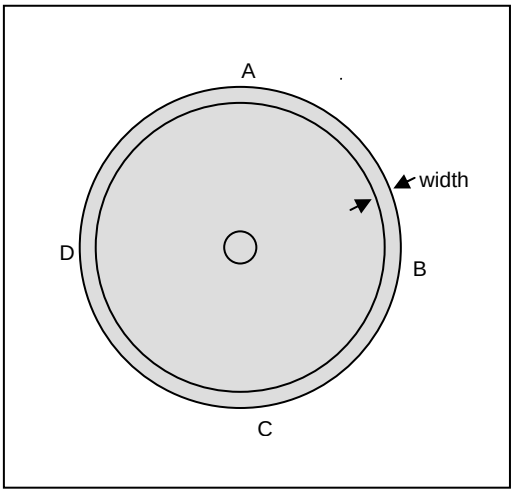

Figure 6.12 Locations of Characterization Measurements for Piston/Diaphragm Piece

The width of the ridge was measured with a micrometer to be 500 μm, 520 μm, 500 μm, and 540 μm in locations A, B, C, and D, respectively. The reason why this feature is wider than intended in some locations is because of the photolithography masks. The pattern transfer was quite good here, but the method used to make the masks has some limitations.

The layouts for the masks were drawn using a commercially available CAD package and then exported as encapsulated postscript files. Next, these postscript files were then printed on transparency film at a resolution of 5 080 dpi. The limitations of postscript format are such that it cannot comprehend smooth curves and they are consequently represented as a series of triangles. Therefore, some of the smoothness of the curves is lost. Figure 6.13a is a magnified clipping from the postscript file used to make Mask # 2. It is apparent from this file that images of smooth curves will not be transferred as such. The resulting image transfer is illustrated by Figure 6.13b, which shows a portion of one of the ridges.

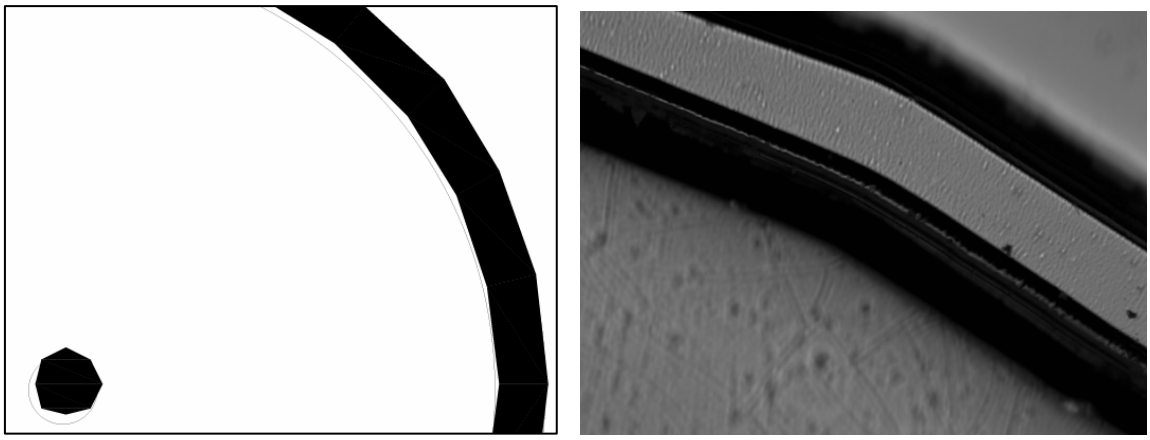

Figure 6.13 a) Portion of Mask #2 b) Resulting Curvature of Ridges

This affected every non-rectilinear feature, although it is most pronounced in the example shown above. For the purposes of this device, however, this is quite acceptable. There is no reason why this would affect the performance of the device, but it is necessary to document for the purpose of SU8 micromolding procedure development.

The next feature that was examined was the thickness of the membrane. This could not be measured directly; therefore, it was calculated as the difference between the ridge height on the inner and outer edges. The height of the outer edge was measured with a micrometer. The height of the inner edge was measured using the microscope adjustment dial. The measurements at locations shown in Figure 6.12 are tabulated in Table 6.1 below.

Table 6.1 Measurements of Diaphragm Thickness

Location	Outer Ridge Height (μm)	Inner Ridge Height (μm)	Diaphragm Thickness (μm)
A	655	495	160
B	650	500	150
C	645	505	140
D	648	497	151

The value of the diaphragm's thickness varied a little bit from location to location. This is mainly because the diaphragm was manually polished to its final thickness. The average of the thickness measurements is 150.25 μm, and this is very close to the intended value of 150 μm.

The height of this piston was also very close to the intended height. This is because a significant amount of the fabrication effort was centered around zeroing in on the parameters that would yield the appropriate SU8 thickness. The piston height was measured by subtracting the diaphragm thickness from the overall height of the piston and diaphragm, measured with a micrometer. The piston height plus diaphragm thickness is 1 143 μm, therefore the piston itself is 993 μm tall.

6.3.2 Flow Channel Piece

The features of the flow channel piece were measured in locations indicated by the points in Figure 6.14. For this device, all features were measured using a micrometer.

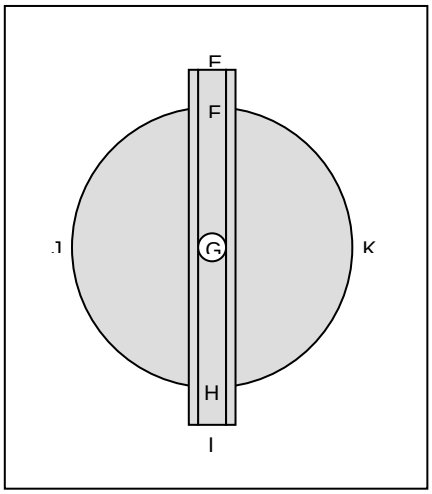

Figure 6.14 Locations of Characterization Measurements for Flow Channel Piece

The measurements of plate thickness, wall height, and wall width at these locations are tabulated in Table 6.2. The target value for each of these features was 500 μm. The target value for the channel width was 1 000 μm.

Table 6.2 Measurements for Flow Channel Piece

Location	Plate Thickness (μm)	Channel Width (μm)	Left Wall		Right Wall	
			Height (μm)	Width (μm)	Height (μm)	Width (μm)
E	450	1050	400	400	375	300
F	450	1080	400	400	375	300
G	NA	1100	300	300	300	300
H	360	1080	390	300	400	300
I	320	1100	400	300	400	300
J	500					
K	500					

The measured plate thickness was slightly thinner than the target thickness of 500 μm near one of the edges. This is again because the back ends of these devices were polished manually, and there is a degree of difficulty in keeping the wafer perfectly parallel to the sand paper. This should not affect the performance of the device, since the affected area is merely a point of connection to the tubing that supplies the flow through the device.

Figure 6.15a shows a photograph of one of the channel walls. It can be seen from this photograph that the walls have a slight trapezoidal shape to them where the top of the flow channel wall is thinner than the bottom. This is likely the result of the same factors explained for the piston being too narrow. Distortion of the channel walls for this piece, and also those on the flow channel cap piece, will not affect the performance of the device. This is because these pieces are used to establish a gap between the top and bottom of the flow channel. As long as a 500 μm gap can be maintained on each end of the channel, the flow channel itself will be 500 μm tall, regardless of the lengthwise profile of the walls.

Figure 6.15b is a picture of the center hole of this piece. The opening of this hole, measured with a micrometer, is 1 092 μm in the direction perpendicular to the channel walls and 1 078 μm in the direction parallel to the walls. The intended shape was to be a circular opening with a diameter of 1 000 μm. The main cause of this slight distortion is due to the pattern on the photolithography mask. This is inferred from the shape of the hole. The edge looks more like a series of straight lines than a continuous curve.

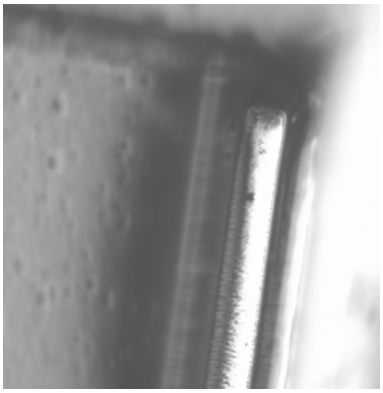

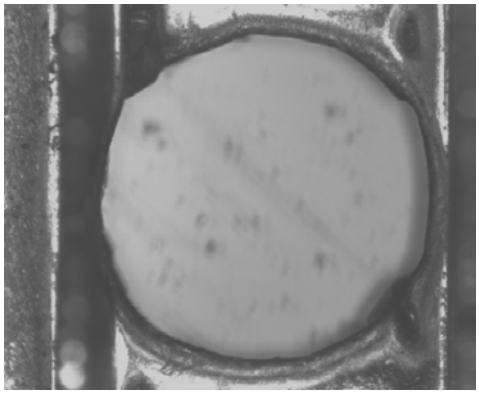

Figure 6.15 a) Photograph of Channel Wall b) Photograph of Channel Through Hole

Figure 6.16 is a photograph of the top of the piston from the piston/diaphragm piece assembled to the through port on the flow channel piece. As detailed earlier, the target diameter for the piston was 950 μm and that of the port was 1 000 μm; while the diameters as fabricated are between 900 μm and 913 μm for the piston and between 1 078 μm and 1 092 μm for the port.

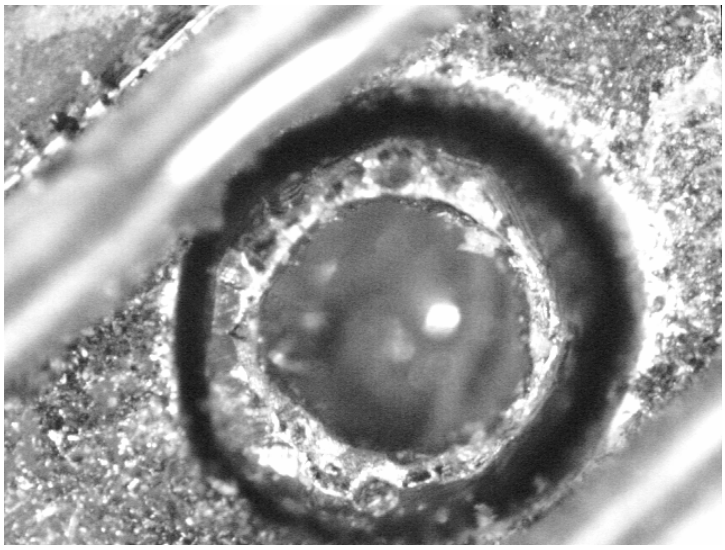

Figure 6.16 Piston and Port Assembly

In all instances, the distortion that occurs with SU8 would not prevent the device from functioning. This is because SU8 is a negative photoresist, therefore any errors due to alignment or scattering will cause cured SU8 to be present where it is not wanted. Also, any problems due to underdevelopment will also leave SU8 where it is not wanted. Ultimately, any imperfections in the pattern transfer will result in the nickel pieces having structures that are thinner than desired and open areas being wider than desired. If this were not the case, then a less than perfect pattern transfer could result in nickel pieces that would not properly assemble. In the case shown above in Figure 6.16, the gap left between the piston and the edges of the port is between 82.5 μm and 96 μm, depending on location; the desired gap is 25 μm uniformly around the piston. Therefore, the piston will still be able to enter the flow passage, but it will not have the ability to completely seal it off.

6.3.3 Flow Channel Cap Piece

The features of the flow channel cap piece were measured in locations indicated by the points in Figure 6.17. For this device, all features were measured using a micrometer.

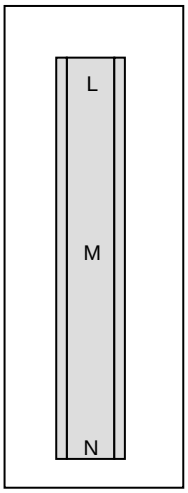

Figure 6.17 Locations of Characterization Measurements for Flow Channel Cap Piece

The measurements of wall height and thickness at these locations are tabulated in Table 6.3. The target value for each of these features is 500 μm.

Table 6.3 Measurements for Flow Channel Cap Piece

Location	Left Wall		Right Wall	
	Height (μm)	Width (μm)	Height (μm)	Width (μm)
L	440	300	500	350
M	500	300	500	350
N	500	300	500	350

The features on this piece showed similar distortions as the channel walls on the flow channel piece, which is to be expected. Again, these distortions should not affect the performance of the device, since the walls merely serve as a spacer.

6.4 Assembly

Many different options were examined before a method of assembling this prototype was devised. The assembly procedure used for the silicon prototype proved undesirable because it was difficult to seal the oil cavity with epoxy. Also, once a working prototype was assembled, the epoxy that held the silicon pieces to the oil cavity proved to be quite flexible which substantially degraded the motion of the piston. Ultimately, such a device would most likely be assembled using a technique similar to [62], but an alternative method must be used for this device due to the mask layouts.

Soldering the pieces to each other and to the oil cavity was an attractive option; however, this presented obstacles which needed to be overcome. Soldering offers a great deal of comfort in terms of creating a seal between the pieces that can withstand high pressure. The difficulty of soldering these pieces together lies in keeping molten solder from flowing into the thin flow channel. The flow channel is a conduit that is approximately 500 μm tall by 1 000 μm wide, which makes it a good conduit for capillary forces to draw molten solder.

Using a laser to weld the pieces together offers the benefits of superior seals between the pieces and to the capsule. The drawbacks associated with this method are the start up time and

cost associated with devising a good method of guiding the laser around the perimeter to create a quality, uniform seal. For this reason, energy and time was focused towards solving the difficulties of soldering these pieces.

Rather than machining an oil capsule for this prototype, commercially available fittings were used. This allows for the possibility of disassembly and repair should the oil leak from the cavity. The cavity was made from two Swagelok fittings; the top portion is a 9.5 mm to 9.5 mm tube to female NPT fitting and the bottom portion is a 1.6 mm tube to 6.3 mm male NPT fitting.

The top portion of the oil capsule is shown below in Figure 6.18a. The left hand side of this fitting is a 9.5 mm compression fitting, which has an outer diameter of 12,700 μm. The size of the piston/diaphragm molded piece was designed to fit on top of this opening. The bottom portion of the capsule is shown in Figure 6.18b. The left hand side of this fitting fits into the other fitting. The right hand side allows a connection to a 1.6 mm tube, which will be used for a thermocouple probe. When these two pieces are assembled, a void of approximately 2.0 mL to 2.5 mL is left between them, which will be filled with oil when the assembly is complete.

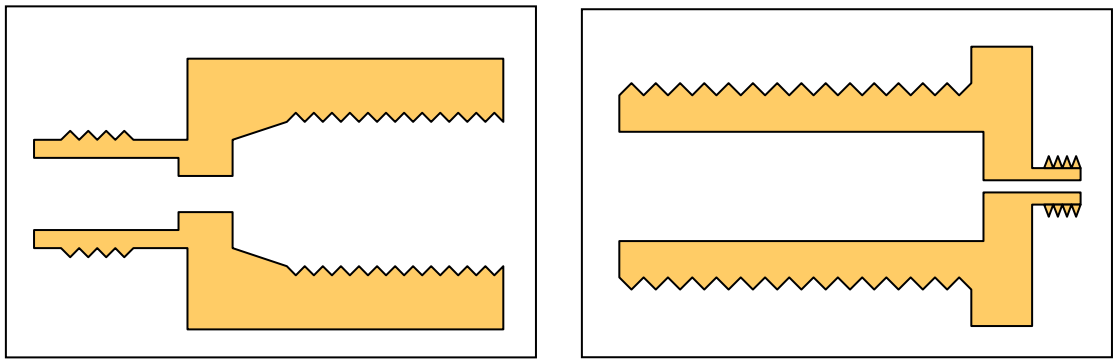

Figure 6.18 a) Top Portion of Oil Capsule b) Bottom Portion of Oil Capsule

In order to properly solder these pieces together and to the top of the oil capsule, they had to be held together, therefore they were spot welded. Welding does not work very well between nickel and brass due to conflicting material properties. Also it is not possible to form a seal that would withstand high pressure in the manner; however, this did work well enough to hold the pieces together so that the assembly could be soldered.

The capsule and pieces were soldered together using a hot plate. Soldering flux was carefully painted into the crevices where solder was desired using a thin wire. Ground up chards of silver solder was then placed on and around the soldering flux and the assembly was placed onto the hot plate. The assembly was monitored while it heated towards the melting point of the solder. Once the solder melted, it was drawn into the crevices and the assembly was quickly removed from the hot plate.

Visual inspection showed that this method formed a continuous seal in all areas. The capsule top was then pressure tested by connecting 1 MPa of compressed air to the back end and submersing the assembly in water. No bubbles were present, indicating that the diaphragm/piston piece was well connected to the capsule. This portion of the assembly is shown below in Figure 6.19.

Figure 6.19 Oil Capsule Top Connected to Flow Restrictor

For the next step, a 14.4 Ω electric resistance heating element was placed into the bottom portion of the oil capsule and its wires were fed through a 1.5 mm diameter hole that was drilled through the rear of the fitting. The heater wires were secured into the hole with refrigerant epoxy. The bottom portion of the oil capsule is shown below in Figure 6.20.

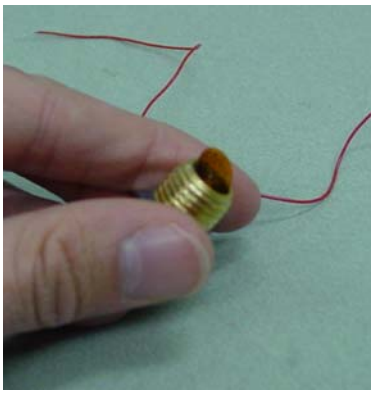

Figure 6.20 Bottom Portion of the Oil Capsule, Including Heater

Next, the two portions of the capsule were fixed together. The reservoir was then filled with 2.1 mL of polyalkalene glycol at a temperature of 24.3 °C, through the compression fitting hole. A thermocouple, calibrated to an uncertainty of 0.1 °C with 95 % confidence, was then secured into this hole.

The measurements taken from the device characterization and the amount and initial temperature of oil were used in a prediction of performance spreadsheet. Figure 6.21 shows the predicted displacement of the piston in this assembly.

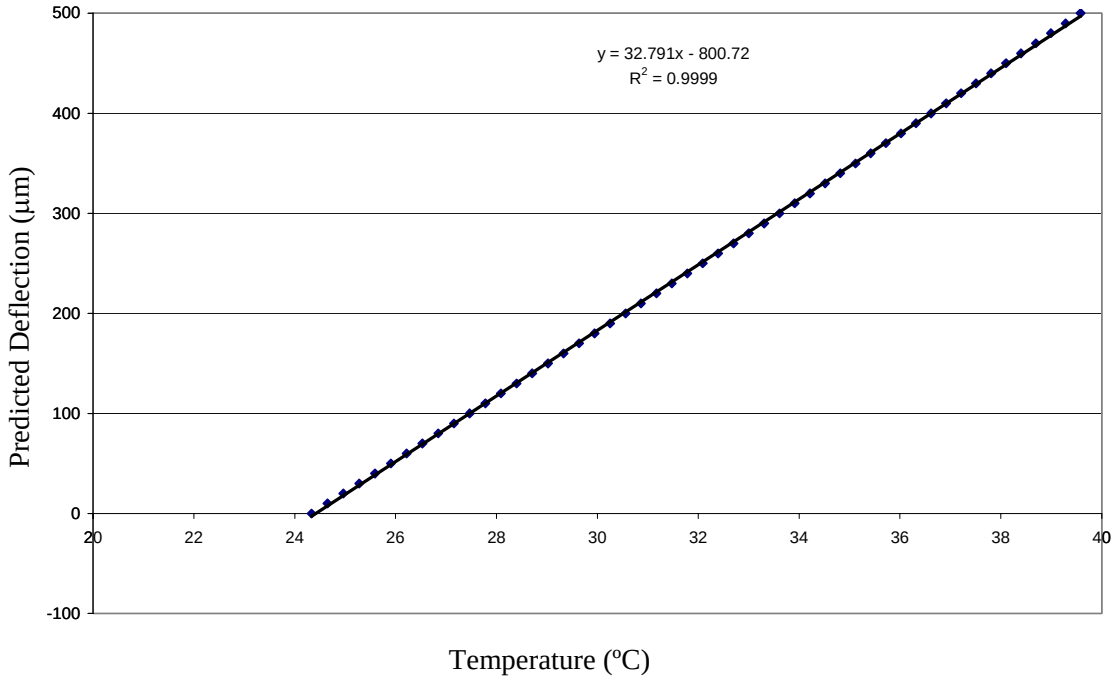

Figure 6.21 Predicted Displacement of Piston

According to the prediction curve, the tip of the piston should reach the top of the flow channel when the oil reservoir temperature is 39.6 °C. There should be some flexibility in the other components surrounding the oil reservoir, but not nearly to the extent that was seen while testing the silicon prototype, since this prototype was soldered together. In the interest of avoiding problems with the piston pushing against the top of the channel, it is not desired to test the device far beyond this point.

6.5 Measured Piston Actuation

Figure 6.21 served as a tool to estimate the motion of the piston while testing the prototype's ability to control flow. In order to truly know the position of the piston, it is necessary to have a measured curve of the relationship between oil temperature and piston position. However, this could only be found through destructive testing. Therefore, after all of the flow experiments were carried out with this device, the flow channel cap piece was cut from the prototype and measurements were taken using the microscope method described in Chapter 4 of this report. Figure 6.22 shows the results of these measurements.

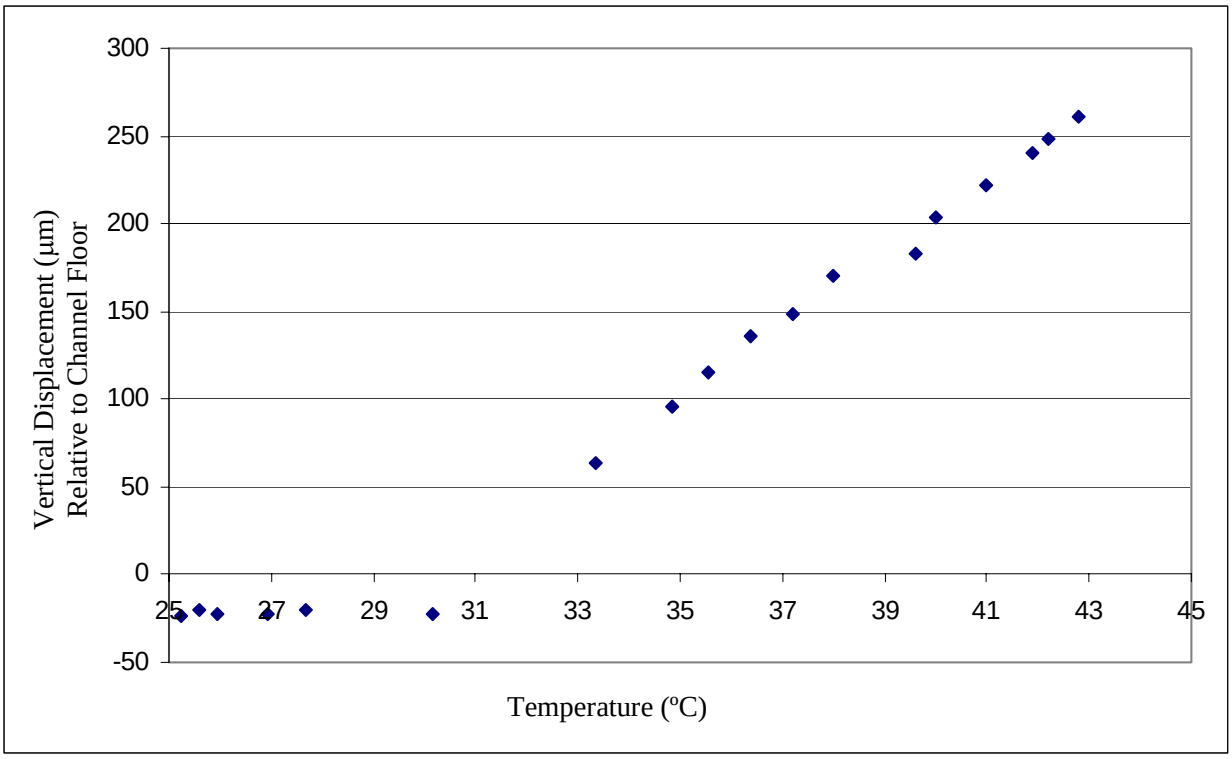

Figure 6.22 Characterization of Piston Displacement for Nickel Micromolded Prototype

There are a few useful bits of information that came from these measurements. First, the results of these measurements show that the piston does not exhibit significant motion until the oil temperature is warmed past approximately 30 ºC. The most logical explanation for this is that a small air bubble is likely present within the capsule, and that the expanding oil must first collapse this bubble before a significant amount of pressure can be applied to the diaphragm.

The second piece of information is the relationship between oil temperature and displacement. Once the piston begins to move with changes in the oil temperature the relationship is linear, as was expected, but the slope of the curve is different than the predicted slope. The measured slope was determined from a best fit straight line through the points above 30 ºC oil temperature. The slope of this line is 20.19 μm /ºC, which is about 2/3 of the predicted slope.

The third piece of information is that, when unactuated, the top of the piston lies approximately 20 μm to 25 μm below the surface of the channel floor. This gap is likely due to the space occupied by the solder between the diaphragm piece and the flow channel piece.

CHAPTER 7
Temporal Response Analysis

The speed at which the device actuates is a rather complicated feature to analyze. It is dependent on the properties of the oil in the reservoir, the properties of the materials making up the capsule, the mass of these materials, the geometry of the capsule, the heater input, and the ambient conditions outside of the capsule.

There are many tradeoffs that must be considered when designing the capsule. As an example, if the amount of oil contained within the capsule is decreased, the thermal mass of this system decreases which tends to speed up the device's response time. Concurrently, the temperature change which must be realized to flex the diaphragm increases, which typically slows down the device's response time. All in all, most design parameters influence the response time in more than one way, and every aspect must be taken into account.

From an initial design and testing point of view, there exists a tradeoff between controllability and response. At this stage of development, controllability is far more important. Although a fast responding device may ultimately be desired, this may be counterproductive to the initial design and testing phase because the user must be able to react faster than the device. Therefore, at this stage of design, the device was designed and assembled in such a way that the oil reservoir and chamber have a large thermal capacitance; i.e., the device will respond slowly to heat input.

What follows in this chapter is an analysis to predict the response time of the device as it was designed. Ultimately, this type of analysis would be used as a design tool which would enable an engineer to speed up the device's response.

7.1 Overview

Since this device is made up of multiple materials, has multiple boundary conditions, and a complex geometry, an analytical solution is impossible to determine. Therefore, a numerical approach is used to determine how fast the oil in the reservoir will change temperature in response to a change in the heater output. Before this can be determined, it is necessary to ascertain the physics of this situation. A sketch of the capsule is shown below in Figure 7.1

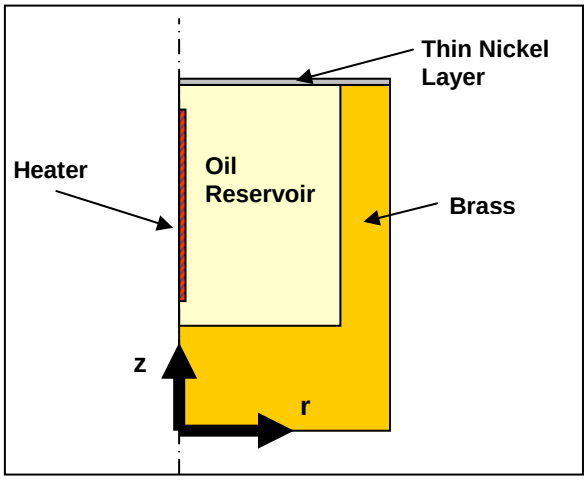

Figure 7.1 Sketch of Capsule

The capsule is approximated by a cylindrical vessel and it is assumed that there are no rotational effects; therefore, a 2-dimensional analysis is adequate. The capsule containing the oil consists of a brass piece that makes up the bottom and sides, and a thin nickel membrane at the top. A heater is located near the center of the capsule. The outer edge of the brass part of the capsule is exposed to ambient conditions. The top of the membrane is exposed to the fluid that is passing through the device.

As the heater is powered up, heat is dissipated into the oil reservoir. This raises the temperature of the oil, which changes its density and flexes the membrane outward. As the temperature of the oil is raised, it dissipates heat to the ambient through the brass portion and to the fluid in the channel through the nickel membrane. At some point, the temperature will stabilize; i.e. the energy input from the heater will balance with the dissipation through the brass and nickel sides of the capsule.

The first step is to identify the mode of heat transfer that is occurring within the capsule. The oil inside the capsule is a liquid and there are no forced currents; therefore, the initial assumption is that energy is being transferred through natural convection. Certain thermodynamic properties of this particular oil are not known; therefore, they are approximated by the properties of glycerin [63].

$$\nu = 0.00831 \frac{\mathrm{m}^2}{\mathrm{s}}$$

$$k = 0.282 \frac{\mathrm{W}}{\mathrm{mK}}$$

$$C_p = 2261 \frac{\mathrm{J}}{\mathrm{kgK}}$$

The Grashof number is calculated in order to verify or reject the occurrence of natural convection in the capsule. The oil capsule has dimensions of 12.6 mm in diameter and 24 mm in height. The characteristic length is found by the ratio of the capsule volume to that of the internal surface area, or one quarter of the diameter, L_c=3.15 mm. The temperature differences within this capsule are typically 10 K to 20 K; cautiously estimating the Grashof number based on a temperature difference of 100 K results in:

$$\mathrm{Gr} = \frac{g\beta\Delta T L_c^{\,3}}{\nu^2} = \frac{\left(9.8\frac{\mathrm{m}}{\mathrm{s}^2}\right)\left(0.0003775\frac{1}{\mathrm{K}}\right)(100\mathrm{K})(0.00315\mathrm{m})^3}{\left(0.00831\frac{\mathrm{m}^2}{\mathrm{s}}\right)^2} = 1.7\times10^{-4}$$

Natural convection can be neglected for Gr $<10^4$ [64]. Since this situation represents eight orders of magnitude below this limit, it is safe to assume that the energy is transferred through the oil solely through conduction.

7.2 Derivation of Nodal Equations

The heat conduction equation in 2-dimensional radial coordinates without heat generation is shown below for points within a single, continuous medium:

$$\frac{1}{r}\frac{\partial}{\partial r}\left(kr\frac{\partial T}{\partial r}\right)+\frac{\partial}{\partial z}\left(k\frac{\partial T}{\partial z}\right)=\rho C_p\frac{\partial T}{\partial t}$$

By assuming that the material properties do not change within the limits of a medium (oil, brass, or nickel), this equation becomes:

$$\frac{1}{r}\left(\frac{\partial T}{\partial r}+r\frac{\partial^2 T}{\partial r^2}\right)+\frac{\partial^2 T}{\partial z^2}=\frac{1}{\alpha}\frac{\partial T}{\partial t}$$

Next, the coordinates are discretized $(r,z)\rightarrow(m\Delta r,n\Delta z)$ and the equation can be written in the form:

$$\frac{1}{m\cdot\Delta r}\left(\frac{T_{(m+1,n)}-T_{(m,n)}}{m\cdot\Delta r}+m\cdot\Delta r\frac{T_{(m+1,n)}+T_{(m-1,n)}-2T_{(m,n)}}{(\Delta r)^2}\right)+\left(\frac{T_{(m,n+1)}+T_{(m,n-1)}-2T_{(m,n)}}{(\Delta z)^2}\right)=\frac{1}{\alpha(\Delta t)}\left(T_{(m,n)}\Big|_{t+\Delta t}-T_{(m,n)}\Big|_t\right)$$

Or more apt for computer calculations:

$$T_{(m,n)}\Big|_{t+\Delta t}=T_{(m,n)}\Big|_t+\frac{\alpha(\Delta t)}{(a\cdot\Delta r)^2}\left(T_{(m+1,n)}-T_{(m,n)}+m^2\left(T_{(m+1,n)}+T_{(m-1,n)}-2T_{(m,n)}\right)\right)+\frac{\alpha(\Delta t)}{(\Delta z)^2}\left(T_{(m+1,n)}+T_{(m-1,n)}-2T_{(m,n)}\right)$$

This is the general form that can be used to calculate the temperature distribution as time is marched forward. In addition to the relationship derived above, special relationships must be derived for nodes that are aligned to a change in medium, i.e., the oil-brass interface, oil-nickel interface, and the brass-nickel interface.

For medium changes that occur along a horizontal line, the relationship is derived as follows, where A and B represent the two media:

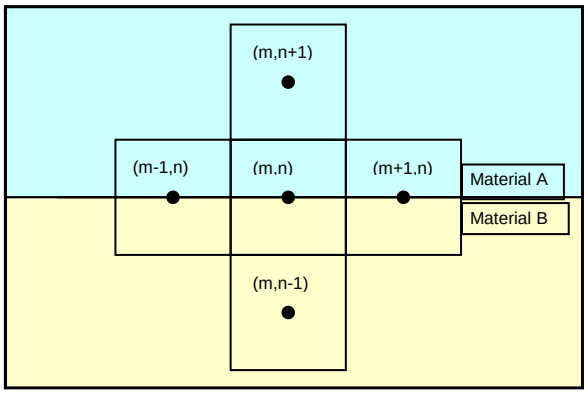

Figure 7.2 Nodal Network for Horizontal Medium Change

The energy transferred into and out of the node in the radial direction is:

$$\frac{1}{2}(k_A+k_B)\left\{\left(m-\frac{1}{2}\right)\Delta r\Delta\Theta\Delta z\right\}\frac{1}{\Delta r}\left(T_{(m-1,n)}-T_{(m,n)}\right)-\frac{1}{2}(k_A+k_B)\left\{\left(m+\frac{1}{2}\right)\Delta r\Delta\Theta\Delta z\right\}\frac{1}{\Delta r}\left(T_{(m,n)}-T_{(m+1,n)}\right)$$

which is simplified to:

$$(\Delta r\Delta\Theta\Delta z)\frac{(k_A+k_B)}{2\Delta r}\left\{\left(m-\frac{1}{2}\right)\left(T_{(m-1,n)}-T_{(m,n)}\right)-\left(m+\frac{1}{2}\right)\left(T_{(m,n)}-T_{(m+1,n)}\right)\right\}.$$

The energy transferred into and out of the node in the vertical direction is:

$$k_B\left(m\Delta r\Delta\Theta\Delta r\right)\frac{1}{\Delta z}\left(T_{(m,n-1)}-T_{(m,n)}\right)-k_A\left(m\Delta r\Delta\Theta\Delta r\right)\frac{1}{\Delta z}\left(T_{(m,n)}-T_{(m,n+1)}\right)$$

which is simplified to:

$$\left(\Delta r\Delta\Theta\Delta z\right)\frac{m\Delta r}{\left(\Delta z\right)^2}\left\{k_B\left(T_{(m,n-1)}-T_{(m,n)}\right)-k_A\left(T_{(m,n)}-T_{(m,n+1)}\right)\right\}.$$

The energy stored in the node is:

$$\rho C_P\forall\frac{\Delta T}{\Delta t}=\rho C_P\left(m\Delta r\Delta\Theta\right)\left(\Delta r\right)\left(\Delta z\right)\frac{\Delta T}{\Delta t}=\left(\Delta r\Delta\Theta\Delta z\right)\left\{\frac{m\Delta r}{2}\left(\rho_A C_{P_A}+\rho_B C_{P_B}\right)\right\}\frac{\left(T_{(m,n)}\Big|_{t+\Delta t}-T_{(m,n)}\Big|_t\right)}{\Delta t}$$

Canceling similar terms and assembling these terms results in the following relationship:

$$\left\{\frac{m\Delta r}{2}\left(\rho_A C_{P_A}+\rho_B C_{P_B}\right)\right\}\frac{\left(T_{(m,n)}\Big|_{t+\Delta t}-T_{(m,n)}\Big|_t\right)}{\Delta t}=\frac{\left(k_A+k_B\right)}{2\Delta r}\left\{\left(m-\frac{1}{2}\right)\left(T_{(m-1,n)}-T_{(m,n)}\right)-\left(m+\frac{1}{2}\right)\left(T_{(m,n)}-T_{(m+1,n)}\right)\right\}$$

$$+\frac{m\Delta r}{\left(\Delta z\right)^2}\left\{k_B\left(T_{(m,n-1)}-T_{(m,n)}\right)-k_A\left(T_{(m,n)}-T_{(m,n+1)}\right)\right\}$$

which can then be rewritten as:

$$T_{(m,n)}\Big|_{t+\Delta t}=T_{(m,n)}\Big|_t+\frac{\left(k_A+k_B\right)\Delta t}{m\left(\Delta r\right)^2\left(\rho_A C_{p_A}+\rho_B C_{p_B}\right)}\left\{\left(m-\frac{1}{2}\right)\left(T_{(m-1,n)}-T_{(m,n)}\right)-\left(m+\frac{1}{2}\right)\left(T_{(m,n)}-T_{(m+1,n)}\right)\right\}$$

$$+\frac{2\Delta t}{\left(\rho_A C_{p_A}+\rho_B C_{p_B}\right)\left(\Delta z\right)^2}\left\{k_B\left(T_{(m,n-1)}-T_{(m,n)}\right)-k_A\left(T_{(m,n)}-T_{(m,n+1)}\right)\right\}$$

This relationship can then be used to calculate the temperature distribution along a change of medium that takes place in the horizontal direction.

Similarly, a relationship is needed to calculate the heat transfer along a set of points that correspond to a change of medium in the vertical direction.

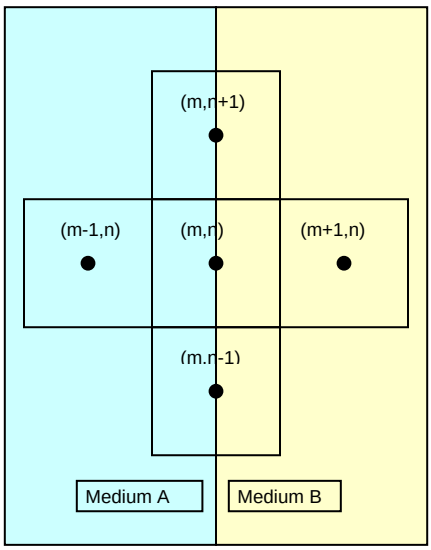

Figure 7.3 Nodal Network for Vertical Medium Change

The energy transferred into and out of the node in the radial direction is:

$$k_A\left[\left(m-\frac{1}{2}\right)\Delta r\Delta\Theta\Delta z\right]\frac{1}{\Delta r}\left(T_{(m-1,n)}-T_{(m,n)}\right)-k_B\left[\left(m+\frac{1}{2}\right)\Delta r\Delta\Theta\Delta z\right]\frac{1}{\Delta r}\left(T_{(m,n)}-T_{(m+1,n)}\right)$$

which is simplified to:

$$(\Delta r\Delta\Theta\Delta z)\left\{\frac{k_A}{\Delta r}\left[\left(m-\frac{1}{2}\right)\left(T_{(m-1,n)}-T_{(m,n)}\right)\right]-\frac{k_B}{\Delta r}\left[\left(m+\frac{1}{2}\right)\left(T_{(m,n)}-T_{(m+1,n)}\right)\right]\right\}.$$

The energy transferred into and out of the node in the vertical direction is:

$$\frac{1}{2}(k_A+k_B)(m\Delta r\Delta\Theta\Delta r)\frac{1}{\Delta z}\left(T_{(m,n-1)}-T_{(m,n)}\right)-\frac{1}{2}(k_A+k_B)(m\Delta r\Delta\Theta\Delta r)\frac{1}{\Delta z}\left(T_{(m,n)}-T_{(m,n+1)}\right)$$

which is simplified to:

$$\frac{m(k_A+k_B)\Delta r}{2(\Delta z)^2}(\Delta r\Delta\Theta\Delta z)\left(T_{(m,n-1)}+T_{(m,n+1)}-2T_{(m,n)}\right).$$

The energy stored in the node is:

$$\rho C_P\forall\frac{\Delta T}{\Delta t}=(\Delta r\Delta\Theta\Delta z)\left\{\frac{m\Delta r}{2}\left(\rho_A C_{P_A}+\rho_B C_{P_B}\right)\right\}\frac{\left(T_{(m,n)}\Big|_{t+\Delta t}-T_{(m,n)}\Big|_t\right)}{\Delta t}$$

Canceling similar terms and assembling these terms results in the following relationship:

$$\left\{\frac{m\Delta r}{2}\left(\rho_A C_{P_A}+\rho_B C_{P_B}\right)\right\}\frac{\left(T_{(m,n)}\Big|_{t+\Delta t}-T_{(m,n)}\Big|_t\right)}{\Delta t}=\left\{\frac{k_A}{\Delta r}\left[\left(m-\frac{1}{2}\right)\left(T_{(m-1,n)}-T_{(m,n)}\right)\right]-\frac{k_B}{\Delta r}\left[\left(m+\frac{1}{2}\right)\left(T_{(m,n)}-T_{(m+1,n)}\right)\right]\right\}$$

$$+\frac{m(k_A+k_B)\Delta r}{2(\Delta z)^2}\left(T_{(m,n-1)}+T_{(m,n+1)}-2T_{(m,n)}\right)$$

Which is rewritten as:

$$T_{(m,n)}\Big|_{t+\Delta t}=T_{(m,n)}\Big|_t+\frac{2\Delta t}{m(\Delta r)^2\left(\rho_A C_{p_A}+\rho_B C_{p_B}\right)}\left\{k_A\left[\left(m-\frac{1}{2}\right)\left(T_{(m-1,n)}-T_{(m,n)}\right)\right]-k_B\left[\left(m+\frac{1}{2}\right)\left(T_{(m,n)}-T_{(m+1,n)}\right)\right]\right\}$$

$$+\frac{(k_A+k_B)\Delta t}{\left(\rho_A C_{p_A}+\rho_B C_{p_B}\right)(\Delta z)^2}\left(T_{(m,n-1)}+T_{(m,n+1)}-2T_{(m,n)}\right)$$

This relationship can then be used to calculate the temperature distribution along a change of medium that takes place in the vertical direction. Within the geometry shown in Figure 7.1, there also exists two points where a change of medium occurs in corners. The first of these points is shown below in Figure 7.4

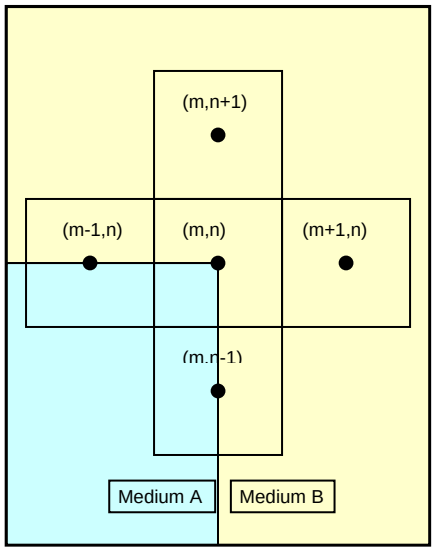

Figure 7.4 Nodal Network for Upper-Corner Medium Change

For this situation the energy transferred into and out of the node in the radial direction is:

$$\frac{1}{2}\left(k_A+k_B\right)\left[\left(m-\frac{1}{2}\right)\Delta r\Delta\Theta\Delta z\right]\frac{1}{\Delta r}\left(T_{(m-1,n)}-T_{(m,n)}\right)-k_B\left[\left(m+\frac{1}{2}\right)\Delta r\Delta\Theta\Delta z\right]\frac{1}{\Delta r}\left(T_{(m,n)}-T_{(m+1,n)}\right)$$

which is simplified to:

$$\left(\Delta r\Delta\Theta\Delta z\right)\left\{\frac{\left(k_A+k_B\right)}{2\Delta r}\left[\left(m-\frac{1}{2}\right)\left(T_{(m-1,n)}-T_{(m,n)}\right)\right]-\frac{k_B}{\Delta r}\left[\left(m+\frac{1}{2}\right)\left(T_{(m,n)}-T_{(m+1,n)}\right)\right]\right\}.$$

The energy transferred into and out of the node in the vertical direction is:

$$\frac{1}{2}\left(k_A+k_B\right)\left(m\Delta r\Delta\Theta\Delta r\right)\frac{1}{\Delta z}\left(T_{(m,n-1)}-T_{(m,n)}\right)-k_B\left(m\Delta r\Delta\Theta\Delta r\right)\frac{1}{\Delta z}\left(T_{(m,n)}-T_{(m,n+1)}\right)$$

which is simplified to:

$$\frac{m\Delta r}{\left(\Delta z\right)^2}\left(\Delta r\Delta\Theta\Delta z\right)\left\{\frac{\left(k_A+k_B\right)}{2}\left(T_{(m,n-1)}-T_{(m,n)}\right)-k_B\left(T_{(m,n)}-T_{(m,n+1)}\right)\right\}.$$

The energy stored in the node is:

$$\rho C_P\forall\frac{\Delta T}{\Delta t}=\left(\Delta r\Delta\Theta\Delta z\right)\left\{\frac{m\Delta r}{4}\left(\rho_A C_{P_A}+3\rho_B C_{P_B}\right)\right\}\frac{\left(T_{(m,n)}\Big|_{t+\Delta t}-T_{(m,n)}\Big|_t\right)}{\Delta t}$$

Canceling similar terms and assembling these terms results in the following relationship:

$$\left\{\frac{m\Delta r}{4}\left(\rho_A C_{P_A}+3\rho_B C_{P_B}\right)\right\}\frac{\left(T_{(m,n)}\Big|_{t+\Delta t}-T_{(m,n)}\Big|_t\right)}{\Delta t}=\left\{\frac{\left(k_A+k_B\right)}{2\Delta r}\left[\left(m-\frac{1}{2}\right)\left(T_{(m-1,n)}-T_{(m,n)}\right)\right]-\frac{k_B}{\Delta r}\left[\left(m+\frac{1}{2}\right)\left(T_{(m,n)}-T_{(m+1,n)}\right)\right]\right\}$$

$$+\frac{m\Delta r}{\left(\Delta z\right)^2}\left\{\frac{\left(k_A+k_B\right)}{2}\left(T_{(m,n-1)}-T_{(m,n)}\right)-k_B\left(T_{(m,n)}-T_{(m,n+1)}\right)\right\}$$

which is rewritten as:

$$T_{(m,n)}\Big|_{t+\Delta t}=T_{(m,n)}\Big|_t+\frac{4\Delta t}{m\left(\Delta r\right)^2\left(\rho_A C_{P_A}+3\rho_B C_{P_B}\right)}\left\{\frac{\left(k_A+k_B\right)}{2}\left[\left(m-\frac{1}{2}\right)\left(T_{(m-1,n)}-T_{(m,n)}\right)\right]-k_B\left[\left(m+\frac{1}{2}\right)\left(T_{(m,n)}-T_{(m+1,n)}\right)\right]\right\}$$

$$+\frac{4\Delta t}{\left(\rho_A C_{P_A}+3\rho_B C_{P_B}\right)\left(\Delta z\right)^2}\left\{\frac{\left(k_A+k_B\right)}{2}\left(T_{(m,n-1)}-T_{(m,n)}\right)-k_B\left(T_{(m,n)}-T_{(m,n+1)}\right)\right\}$$

This relationship can then be used to calculate the temperature distribution when a change of medium takes place in an upper internal corner. The relationship for the lower internal corner is derived next, Figure 7.5 shows this situation.

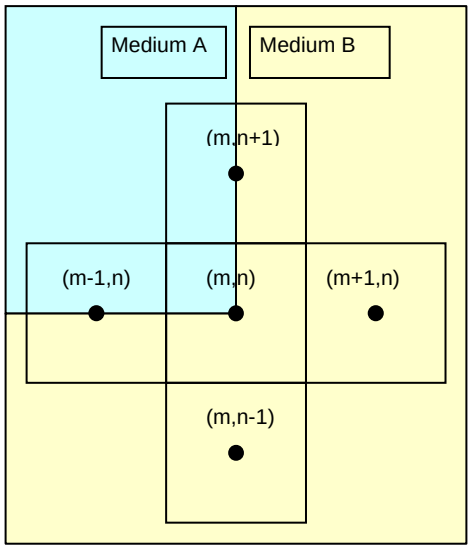

Figure 7.5 Nodal Network for Lower-Corner Medium Change

For this situation the energy transferred into and out of the node in the radial direction is the same as the previous case:

$$\left(\Delta r\Delta\Theta\Delta z\right)\left\{\frac{\left(k_A+k_B\right)}{2\Delta r}\left[\left(m-\frac{1}{2}\right)\left(T_{(m-1,n)}-T_{(m,n)}\right)\right]-\frac{k_B}{\Delta r}\left[\left(m+\frac{1}{2}\right)\left(T_{(m,n)}-T_{(m+1,n)}\right)\right]\right\}$$

The energy transferred into and out of the node in the vertical direction is:

$$k_B\left(m\Delta r\Delta\Theta\Delta r\right)\frac{1}{\Delta z}\left(T_{(m,n-1)}-T_{(m,n)}\right)-\frac{\left(k_A+k_B\right)}{2}\left(m\Delta r\Delta\Theta\Delta r\right)\frac{1}{\Delta z}\left(T_{(m,n)}-T_{(m,n+1)}\right)$$

which is simplified to:

$$\frac{m\Delta r}{\left(\Delta z\right)^2}\left(\Delta r\Delta\Theta\Delta z\right)\left\{k_B\left(T_{(m,n-1)}-T_{(m,n)}\right)-\frac{\left(k_A+k_B\right)}{2}\left(T_{(m,n)}-T_{(m,n+1)}\right)\right\}.$$

The energy stored in the node is again:

$$\rho C_P\forall\frac{\Delta T}{\Delta t}=\left(\Delta r\Delta\Theta\Delta z\right)\left\{\frac{m\Delta r}{4}\left(\rho_A C_{P_A}+3\rho_B C_{P_B}\right)\right\}\frac{\left(T_{(m,n)}\Big|_{t+\Delta t}-T_{(m,n)}\Big|_t\right)}{\Delta t}.$$

Canceling similar terms and assembling these terms results in the following relationship:

$$\left\{\frac{m\Delta r}{4}\left(\rho_A C_{P_B}+3\rho_B C_{P_B}\right)\right\}\frac{\left(T_{(m,n)}\Big|_{t+\Delta t}-T_{(m,n)}\Big|_t\right)}{\Delta t}=\left\{\frac{\left(k_A+k_B\right)}{2\Delta r}\left[\left(m-\frac{1}{2}\right)\left(T_{(m-1,n)}-T_{(m,n)}\right)\right]-\frac{k_B}{\Delta r}\left[\left(m+\frac{1}{2}\right)\left(T_{(m,n)}-T_{(m+1,n)}\right)\right]\right\}$$

$$+\frac{m\Delta r}{\left(\Delta z\right)^2}\left\{k_B\left(T_{(m,n-1)}-T_{(m,n)}\right)-\frac{\left(k_A+k_B\right)}{2}\left(T_{(m,n)}-T_{(m,n+1)}\right)\right\}$$

which can be rewritten as:

$$T_{(m,n)}\Big|_{t+\Delta t} = T_{(m,n)}\Big|_{t} + \frac{4\Delta t}{m(\Delta r)^2\left(\rho_A C_{P_B} + 3\rho_B C_{P_B}\right)}\left\{\frac{(k_A+k_B)}{2}\left[\left(m-\frac{1}{2}\right)\left(T_{(m-1,n)}-T_{(m,n)}\right)\right]-k_B\left[\left(m+\frac{1}{2}\right)\left(T_{(m,n)}-T_{(m+1,n)}\right)\right]\right\}$$

$$+\frac{4\Delta t}{\left(\rho_A C_{P_B} + 3\rho_B C_{P_B}\right)(\Delta z)^2}\left\{k_B\left(T_{(m,n-1)}-T_{(m,n)}\right)-\frac{(k_A+k_B)}{2}\left(T_{(m,n)}-T_{(m,n+1)}\right)\right\}$$

This relationship can then be used to calculate the temperature distribution when a change of medium takes place in a lower internal corner.

Next, the nodes along the centerline (r = 0) require a special derivation. For this case, a heat generation term is also included because it is assumed that the heater will reside along the centerline (see Figure 7.6 below). In this analysis, a simplification was used that assumes the heat generation occurs wholly within the centerline nodes. This is not completely accurate, but it is good for modeling purposes. Inaccuracies derived from this assumption are due to the resulting heat generating nodes which form a heater that is smaller than the actual heater. This will result in a warmer centerline temperature in the oil because the modeled heat flux must be greater than the actual heat flux to result in the same output.

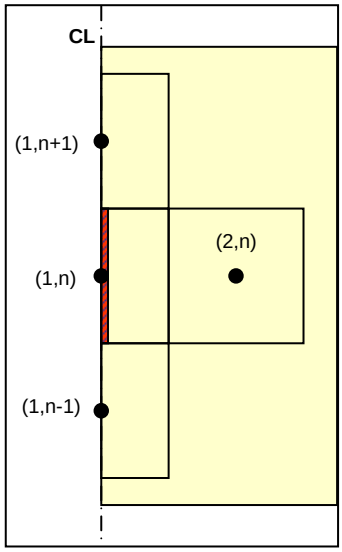

Figure 7.6 Nodal Network for Nodes Along Centerline

For this situation, symmetry dictates that there is no energy transferred into or out of the cells from the left hand side; therefore, the energy transferred in the radial direction is simply:

$$k\left(\frac{\Delta r}{2}\Delta\Theta\Delta z\right)\frac{1}{\Delta r}\left(T_{(2,n)}-T_{(1,n)}\right)$$

The energy transferred into and out of the node in the vertical direction is:

$$k\left(\frac{\Delta r}{8}\right)(\Delta\Theta\Delta r)\frac{1}{\Delta z}\left(T_{(1,n-1)}-T_{(1,n)}\right)-k\frac{\Delta r}{8}(\Delta\Theta\Delta r)\frac{1}{\Delta z}\left(T_{(1,n)}-T_{(1,n+1)}\right)$$

which is simplified to:

$$\frac{k\Delta r}{8(\Delta z)^2}(\Delta r\Delta\Theta\Delta z)\left(T_{(1,n-1)}+T_{(1,n+1)}-2T_{(1,n)}\right).$$

The energy input to the node through the heater is simply:

$$\dot{q}_{gen} = q'''\forall = q'''\left(\frac{\Delta r}{8}\right)\left(\Delta r \Delta\Theta \Delta z\right).$$

The energy stored in the node is again:

$$\rho C_P \forall \frac{\Delta T}{\Delta t} = \rho C_P \left(\frac{\Delta r}{8}\right)\left(\Delta r \Delta\Theta \Delta z\right)\frac{\left(T_{(m,n)}\Big|_{t+\Delta t} - T_{(m,n)}\Big|_t\right)}{\Delta t}.$$

Canceling similar terms and assembling these terms results in the following relationship:

$$\left(\frac{\Delta r}{8\alpha}\right)\frac{\left(T_{(m,n)}\Big|_{t+\Delta t} - T_{(m,n)}\Big|_t\right)}{\Delta t} = \frac{1}{2\Delta r}\left(T_{(2,n)} - T_{(1,n)}\right) + \frac{\Delta r}{8\left(\Delta z\right)^2}\left(T_{(1,n-1)} + T_{(1,n+1)} - 2T_{(1,n)}\right) + q'''\left(\frac{\Delta r}{8k}\right),$$

can be rewritten as:

$$T_{(m,n)}\Big|_{t+\Delta t} = T_{(m,n)}\Big|_t + \frac{4\alpha\Delta t}{\left(\Delta r\right)^2}\left(T_{(2,n)} - T_{(1,n)}\right) + \frac{\alpha\Delta t}{\left(\Delta z\right)^2}\left(T_{(1,n-1)} + T_{(1,n+1)} - 2T_{(1,n)}\right) + q'''\left(\frac{\alpha\Delta t}{k}\right)$$

This relationship can then be used to calculate the temperature distribution along the centerline with heat generation.

Finally, relationship for the last case of a change of medium along the centerline is analyzed. For this case, the heat generation term is left out because the heater in the capsule resides only in the oil. See Figure 7.7 below.

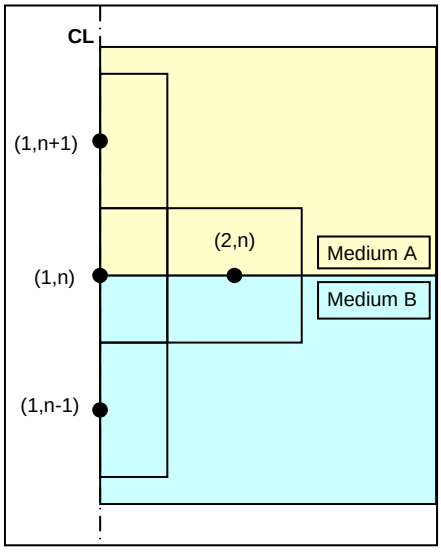

Figure 7.7 Nodal Network for Nodes Along Centerline with Medium Change

For this situation the energy transferred in the radial direction is:

$$\frac{\left(k_A + k_B\right)}{2}\left(\frac{\Delta r}{2}\Delta\Theta\Delta z\right)\frac{1}{\Delta r}\left(T_{(2,n)} - T_{(1,n)}\right).$$

The energy transferred into and out of the node in the vertical direction is:

$$k_B\left(\frac{\Delta r}{8}\right)\left(\Delta\Theta\Delta r\right)\frac{1}{\Delta z}\left(T_{(1,n-1)} - T_{(1,n)}\right) - k_A\frac{\Delta r}{8}\left(\Delta\Theta\Delta r\right)\frac{1}{\Delta z}\left(T_{(1,n)} - T_{(1,n+1)}\right),$$

which is simplified to:

$$\frac{\Delta r\left(\Delta r\Delta\Theta\Delta z\right)}{8\left(\Delta z\right)^2}\left[k_B\left(T_{(1,n-1)}-T_{(1,n)}\right)+k_A\left(T_{(1,n+1)}-T_{(1,n)}\right)\right].$$

The energy stored in the node is again:

$$\rho C_P\forall\frac{\Delta T}{\Delta t}=\frac{\left(\rho_A C_{P_A}+\rho_B C_{P_B}\right)}{2}\left(\frac{\Delta r}{8}\right)\left(\Delta r\Delta\Theta\Delta z\right)\frac{\left(T_{(m,n)}\Big|_{t+\Delta t}-T_{(m,n)}\Big|_t\right)}{\Delta t}.$$

Canceling similar terms and assembling these terms results in the following relationship:

$$\frac{\left(\rho_A C_{P_A}+\rho_B C_{P_B}\right)}{2}\left(\frac{\Delta r}{8}\right)\frac{\left(T_{(m,n)}\Big|_{t+\Delta t}-T_{(m,n)}\Big|_t\right)}{\Delta t}=\frac{\left(k_A+k_B\right)}{4\Delta r}\left(T_{(2,n)}-T_{(1,n)}\right)$$

$$+\frac{\Delta r}{8\left(\Delta z\right)^2}\left[k_B\left(T_{(1,n-1)}-T_{(1,n)}\right)+k_A\left(T_{(1,n+1)}-T_{(1,n)}\right)\right]$$

which is rewritten as:

$$T_{(m,n)}\Big|_{t+\Delta t}=T_{(m,n)}\Big|_t+\frac{4\left(k_A+k_B\right)\Delta t}{\left(\rho_A C_{P_A}+\rho_B C_{P_B}\right)\left(\Delta r\right)^2}\left(T_{(2,n)}-T_{(1,n)}\right)$$

$$+\frac{2\Delta t}{\left(\rho_A C_{P_A}+\rho_B C_{P_B}\right)\left(\Delta z\right)^2}\left[k_B\left(T_{(1,n-1)}-T_{(1,n)}\right)+k_A\left(T_{(1,n+1)}-T_{(1,n)}\right)\right]$$

This relationship can then be used to calculate the temperature distribution along the centerline at interfaces between two media.

7.3 Nodal Spacing and Code Structure

Now that relations have been established for each type of node in the domain, the node size and time step must be determined. Numerical codes involving forward marching in time require that each nodal solution have some dependence on its solution at the previous time step; therefore, the selection of an appropriate time step is critical for stability [59]. For simplicity, the node size is selected such that the radial increments are equal to the vertical increments, i.e. $\Delta r=\Delta z$. Then the dependence of a future time step's solution on the previous time step is found by gathering temperature terms for the (m,n) node.

$$T_{(m,n)}\Big|_{t+\Delta t}=T_{(m,n)}\Big|_t\left(1-\frac{\alpha\left(\Delta t\right)}{\left(m\cdot\Delta r\right)^2}-\frac{2\alpha\left(\Delta t\right)}{\left(\Delta r\right)^2}+\frac{2\alpha\left(\Delta t\right)}{\left(\Delta z\right)^2}\right)+other\_terms$$

And checking the stability criterion at the limiting nodes along m=1, the relation of the previous time step to the future time step is:

$$T_{(m,n)}\Big|_{t+\Delta t}=T_{(m,n)}\Big|_t\left(1-\frac{5\alpha\left(\Delta t\right)}{\left(\Delta r\right)^2}\right)$$

In order to have stable iterations throughout the code, the time step must be selected such that

$$\left(1-\frac{5\alpha\left(\Delta t\right)}{\left(\Delta r\right)^2}\right)>0$$

$$\therefore\Delta t<\frac{\left(\Delta r\right)^2}{5\alpha}$$

To begin this analysis, a nodal distance must be selected. Since the smallest feature on this device is the thickness of the membrane, at 150 μm, this is the largest possible node size. According to the relationship derived above, considering nodal spacing of 150 μm and the thermal properties of brass (the highest thermal diffusivity of all materials used here), the maximum allowable time step is 133 μs. Thus a time step of 100 μs will be used. Using the maximum spacing of 150 μm by 150 μm nodes, the grid for this device is represented by an array 52 nodes wide and 216 nodes tall, for an overall total of 11 232 nodes.

A C++ code was created to simulate the transient thermal response of the capsule [65]. The flowchart for this code consists is rather simplistic, it is seen below in Figure 7.8. The raw code can be found in Appendix A.

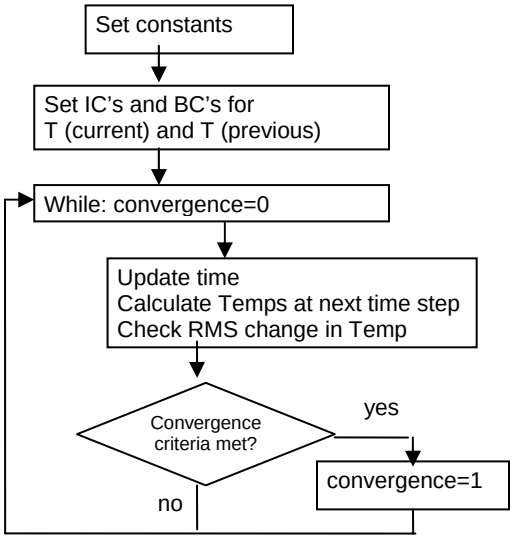

Figure 7.8 Flowchart for Code Execution

At the onset of the program, all of the initial of the constants are set. Next, the temperatures at the boundaries are set and the initial temperature distribution is read from a file. Then the code enters a loop in which all temperatures within the domain are calculated at the next time step. As the code iterates through the time steps, the root mean square (rms) temporal change and the total running time are calculated. Either of these parameters may be used to determine the stopping condition. For the first set of runs, the rms temperature change was used for the convergence test. According to the physics of the simulated situation, the temperature distribution will always change as it asymptotically approaches a solution. Once the rms change becomes less than a specified level ($1.5X10^{-8}$ for this code which corresponds to a rate of change of less than 0.0001 °C/s) the convergence parameter is set to a value that will kick it out of the loop.

Once the code has converged on a temperature distribution, it calculates the average oil temperature. Since this system is in cylindrical coordinates, the average oil temperature is calculated by weighting the temperature at each node by its distance from the z-axis.

For these simulations, constant temperature boundaries were fixed: 5 °C at the top of the nickel membrane (due to the flashing refrigerant) and 25 °C at the outer edges of the brass

portion (ambient condition). For the first test of this code, an initial temperature distribution was imposed, with 20 °C throughout the device. The output from the code was the steady state temperature distribution, the time required to bring the system to steady state from the imposed isothermal initial condition, and the average oil temperature.

The output of this run showed convergence at time = 490.27040 s with an average oil temperature of 21.302 °C. The steady state temperature distribution is shown below in Figure 7.9.

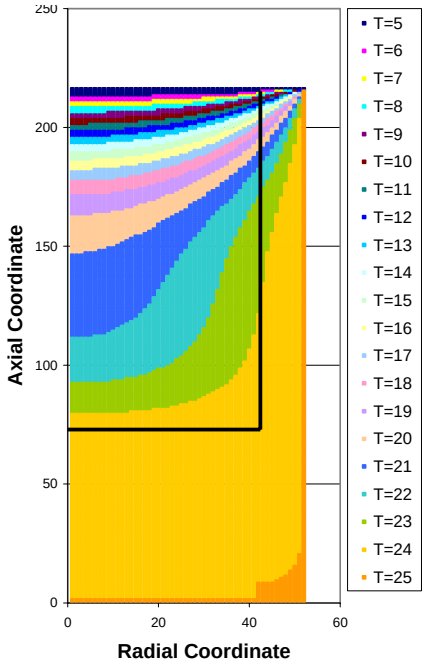

Figure 7.9 Steady State Temperature Distribution

The solid dark line on this figure denotes the transition between the brass capsule and the oil contained in the reservoir. The nickel membrane at the top is difficult to delineate due to the very steep temperature gradients in its vicinity.

After the results were inspected, the next step was to verify that the nodal spacing was appropriate. To perform this task, the grid spacing was divided in half. The code was modified for 75 μm by 75 μm grid spacing. For this nodal spacing, the maximum allowable time step is 33.15 μs; therefore, a time step of 30 μs was used.

Because the steady state criteria in the original code was based on the root mean square of the temperature change of all the nodes, a change in the grid spacing, time step and number of nodes would change the steady state criteria. Therefore, a better comparison between the two codes is made by marching forward for an equivalent time period. This modified code was marched out in time for the same amount of time that was determined to bring the system to steady state for the grid with 150 μm by 150 μm nodes. The average oil temperature was found to be 21.255 ºC, which is 0.047 °C colder than the previous solution, and the temperature distribution plot looks identical to that shown in Figure 7.9. This demonstrates that the solutions are close enough to continue with the 150 μm by 150 μm grid spacing.

7.4 Transient Response Experiments

Once this code was developed, it was used to analyze the device's response to thermal input from the heater in the capsule. For this task, a series of simulations were performed with the heater load set to four levels of heat dissipation: 0.25 W, 0.50 W, 0.75 W, and 1.00 W. At the onset of each of these simulations, the initial power-off temperature distribution found in the previous section was fed into the code as the starting point. The temperature distribution was calculated in response to steady heat input and was output from the code at discrete time intervals. Figure 7.10 shows some of the results from the simulation of the device's response to a 1 W input from the heater.

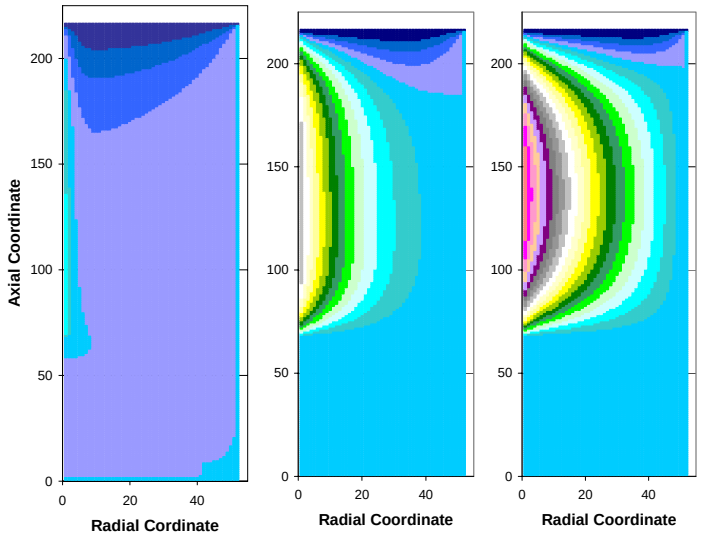

t = 1 s t = 60 s t = 180 s

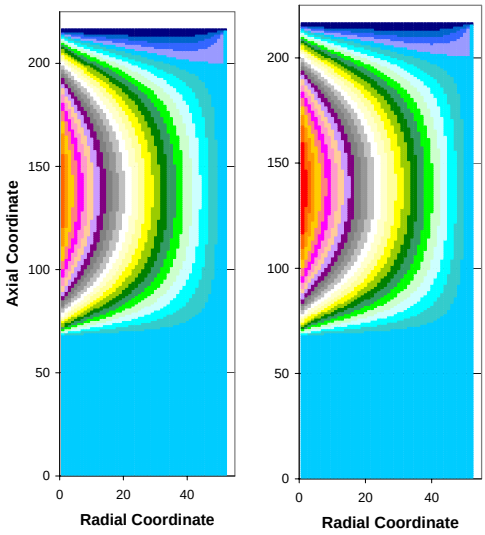

+

t = 300 s t = 720 s

Figure 7.10 Time Elapsed Temperature Distribution at 1 W of Heat Generation

The overall average oil temperature (the variable of interest in this section) was calculated from each temperature distribution returned from the code. Figure 7.11 below shows how the average oil temperature relates to time and the heater output.

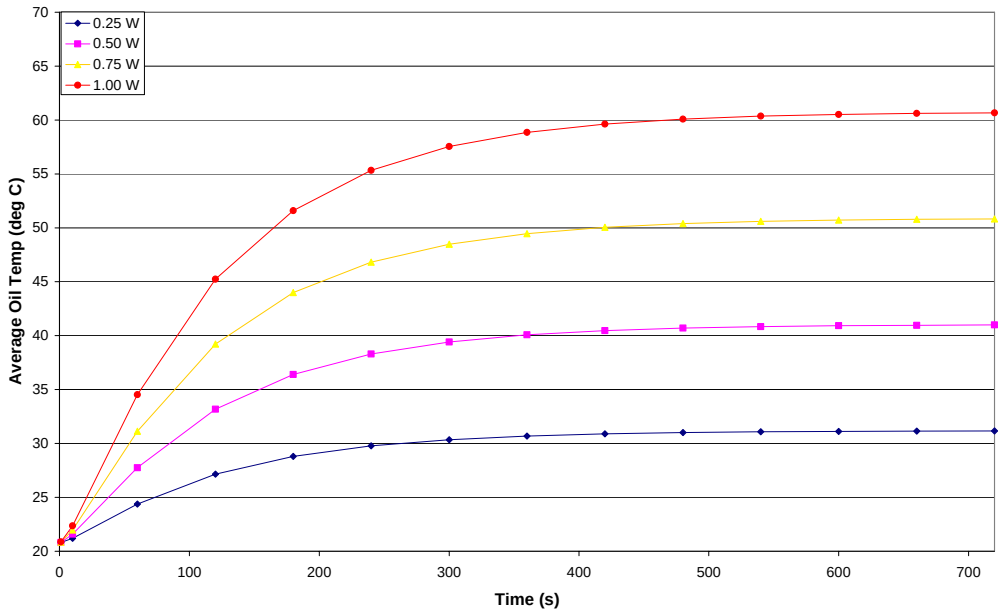

Figure 7.11 Transient Thermal Response of Device to Heat Input

The generalized functional form of this response somewhat resembles that of a simple exponential decay, which was expected. There exists an effect, however, which causes slight deviations from this functional form. It is caused by differences in the material properties. Since the heater is centered in the oil, which has a much lower thermal diffusivity than the brass and nickel sections, there exists a time lag between the heater switch and the point where the remainder of the system reacts to the addition of this energy. This can be seen in Figure 7.12, which shows the first 120 s of transient response. Notice that the thermal response tends to be concave upwards during the first 10 s to 15 s, until the temperature gradients within the oil capsule are established.

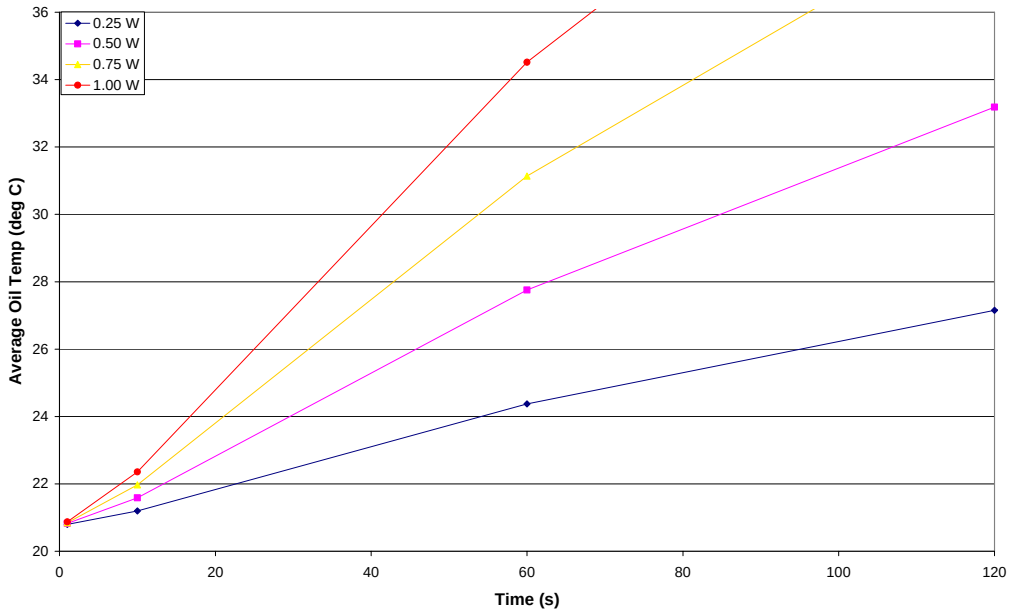

Figure 7.12 Immediate Response of Device to Heat Input

The temperatures that would be acquired at steady state and the time constant of the system were determined by curve fitting. For these fits, the initial two data points (at time = 1 s and 10 s) were left out, so that the time lag brought about by the large differences in material property would be left out. The device's time response must be of the following functional form:

$$T = \Theta - (\Theta - \Theta_0)\exp(-(t-\varepsilon)/\tau)$$

In which case Θ_0 is the steady state temperature with no power input, Θ is the steady state temperature at a given power input, ε is the time lag necessary to establish the thermal gradients, and τ is the device's thermal time constant. The time constant was found first by plotting the natural log of $(\Theta - \Theta_0)$ against the time, and adjusting the steady state temperature until the locus of points could be fit with a straight line having the resulting R^2 greater than 0.9999999. The slope of this best fit straight line is equal to the device's thermal time constant, τ.

Using the thermal time constant, the steady state power on temperature, and the steady state power off temperature, the time lag term is determined from a least squares fit of the functional form. Table 7.1 shows the results of these curve fits.

Table 7.1 Curve Fit Parameters for Device's Time Response

Heat Input (W)	Steady State Temp (ºC)	Time Constant (s)	Time Lag (s)
0.00	21.30229	N/A	N/A
0.25	31.176	114.21817	17.482
0.50	41.033	114.21049	14.768
0.75	50.890	114.20765	13.849
1.00	60.747	114.2063	13.385

The thermal time constant for system response to steady input, τ, is approximately 114.21 s, as was determined for each set of data. The time lag is more significantly pronounced at the lowest heater input, due to the lower driving potential. The steady state oil temperature is proportional to the heater output, which was also expected, and can be approximated by:

$$\Theta = 21.30229 + 39.450 * Q$$

Where Q (W) is the heat generated by the heater. This parameter is directly tied to the displacement of the piston on top of the nickel membrane, as outlined in Chapter 6. Therefore, we can combine the relationship between the oil temperature and the piston displacement with those derived in this section.

7.5 Summary

This section outlined a method for predicting the transient response of the heater-oil reservoir system. Since this device is comprised of a complex geometry and three different materials, an analytic solution is not possible. Therefore, a numerical code was developed to simulate the time dependent response of the system to steady thermal input from the heater. Derivations of each type of nodal equation were presented in this section, as well as a code structure and demonstration of the code developed for the device as designed. In the future, a design engineer can use this approach to determine the transient response with different design parameters.

CHAPTER 8
Numerical Simulations

Computationally describing the expansion of a refrigerant as it passes through a short tube, or in this case a short tube with an obstruction, is not possible with current methods. The problem involves multiphase fluid mechanics, with the liquid phase experiencing metastable conditions and vapor phase flowing at or near its sonic velocity. The full physics of this situation are not well understood today. Most of the information used to predict refrigerant expansion is based on black-box or grey-box modeling of experimental data.

In order to predict the functionality of this device, however, a physically based description of the device's performance must be computed. For this reason, a Computational Fluid Dynamics (CFD) based analysis was performed with the device's geometry, for a single phase gaseous fluid passing through the flow channel. A commercially available CFD package was used to perform the simulations at various levels of actuation. These calculations were used to generate a tool for the prediction of the device's performance over a range of conditions. The results of these simulations were then compared to the laboratory results for gaseous flow through the prototype.

The software package consists of three modules. The pre-processing software is a general purpose geometry and grid generation software package. The solver solves the appropriate differential equations specified by the user over the domains generated with the pre-processing package. The post processing software is an interactive graphics program that allows the user to view the results of the CFD simulations.

8.1 Initial Simulations

Initial simulations were performed with the CFD package to verify the methodology. The task was to find the mass flow rate of compressed air through the device as it entered at a pressure of 316 kPa and 300 K, and exited at a lower pressure of 202 kPa, while the device was in the fully open or unactuated position. These are representative of conditions that could be easily observed under laboratory conditions.

The first task was to generate the domain over which to solve the equations of mass, momentum, and energy conservation. The unactuated flow channel can be described as a rectangular channel, 500 μm tall by 1 000 μm wide, with a length of 19 600 μm. Each end of the flow channel is abruptly connected to a 6.35 mm diameter section of tubing. By selecting the geometry of an unactuated device, it was possible to take advantage of two planes of symmetry, which drastically reduced the computational time. The computational domain for this simulation can be seen below in Figure 8.1.

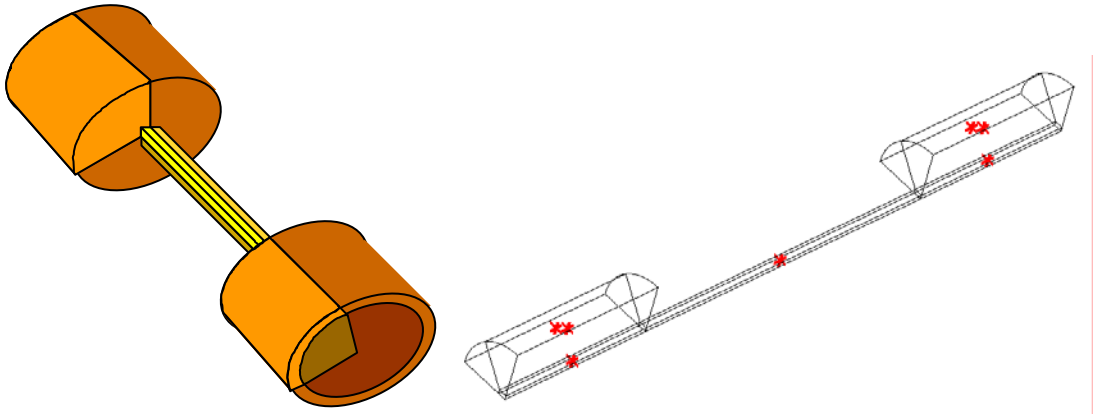

Figure 8.1 Portion of Device used for Initial CFD Simulations

After utilizing symmetry to reduce the computational domain, the remaining flow field was divided into 7 volumes, three forming the flow inlet (termed i1, i2, and i3), three forming the outlet (termed e1, e2, and e3), and one representing the channel. The domain that represented the flow channel was of rectangular shape, with a length of 19 600 μm, width of 500 μm and a height of 250 μm. The inlet and exit plane volumes (i1 and e1) were of the same cross sectional area, but had a length of 10 000 μm. These volumes were a projection of the flow channel into the pipe connections. Finally, the remaining 4 volumes can each be described as a 45 degree sweep of the connected pipe, minus the volume occupied by volumes i1 and e1.

A mesh was generated which divided each entity by 25 points, so that 24 evenly spaced sections were bounded on each entity. Altogether, this created a mesh of 96 768 cells over which to solve for the flow field.

Once the geometry was constructed and the mesh was generated, the data file was imported into the CFD solver environment. The problem types of "flow" and "heat transfer" were selected so that the continuity of mass, momentum, and energy equations were computed. The heat transfer calculations were combined into the analysis so that the temperature distribution (and therefore the density) would be more accurate.

Gravitational and transient effects were turned off. The fluid was set to "air" which obtains information from the package's database. The density was calculated using the ideal gas law, and the dynamic viscosity of air was computed using Sutherland's law.

Next, the boundary conditions were set. For this problem, the inlet surfaces of volumes i1, i2, and i3 were held at a constant pressure of 316 kPa and a temperature of 300 K. At the opposite end of the flow field, the exit planes of the volumes e1, e2, and e3 were held at a constant pressure of 202 kPa. All wall surfaces were modeled as adiabatic and given the boundary condition of zero velocity. All symmetry planes were given the boundary conditions of zero gradients for all properties and velocities. The interface planes between all of the volumes were left unbounded and were to be determined by the solver. The initial conditions used are shown in Table 8.1.

Table 8.1 Initial Conditions used for Preliminary Simulations

	U_x (m/s)	U_y (m/s)	U_z (m/s)	P (kPa)	T (K)
i1	10	0	0	316	300
i2	10	0	0	316	300
i3	10	0	0	316	300
Flow channel	150	0	0	251	280
e1	100	0	0	202	260
e2	10	0	0	202	260
e3	10	0	0	202	260

The solver was set to calculate the velocity and density with an upwind spatial differencing. The convergence criteria were set to a maximum residual of 0.0001 for the each component of velocity, pressure and enthalpy. The inertial relaxation parameters for the velocity, pressure correction, and enthalpy were continuously manipulated throughout each simulation; therefore, it would not be accurate to state the number of iterations required for convergence. The process time is a much more informative bit of information. The process time for this situation was approximately 30 s per iteration on a personal computer with a 3.0 GHz processor.

The critical piece of information obtained from this exercise is the mass flow rate through the device. The output data file from the simulation showed the mass flow rate into the device as 6.8687E-5 kg/s. Multiplying by 4, the total mass flow rate through an entire device was found to be 2.74748E-4 kg/s.

The convergence of these calculations were rather time consuming; therefore, another simulation was run with the same configuration, except this time the heat transfer model was turned off. The heat transfer model was initially used so that the temperature field would be solved and this information would be used to calculate the density of air at each node using the ideal gas law. Upon examining the results of the CFD simulation, it was investigated whether including the temperature effects on density was necessary, considering the large pressure effect on the air density.

The next simulations were performed in the same manner, using an isothermal flowfield with all nodes held at 300 K. The end result was a mass flow rate through the device of as 6.86263E-5 kg/s. Multiplying by 4, the total mass flow rate through an entire device was found to be 2.745052E-4 kg/s, which is less than a 0.1 % difference from the calculations that included the heat transfer analysis. The computational time, however, was vastly improved. Each iteration took approximately 8 s, roughly one quarter of the time of the previous simulation. More importantly, with the elimination of the heat transfer analysis, the number of iterations was drastically decreased.

One more test was required before this simulation tool could be properly used. This test was needed to determine whether the mesh was fine enough for this flow situation. In order to test this, another mesh was generated with the same geometry. This time, however, the grid was doubled so that each entity was divided by 50 points into 49 sections. This increased the number of cells by a factor of 8 to 774 144. The data file for this configuration was very large, 108 MB.

This mesh was brought into the solver and ran with the same initial conditions, boundary conditions, and convergence criteria as the previous problem. The convergence of this problem

was extremely slow; the iterations each took approximately 2 minutes of computational time. The largest obstacle to overcome with this problem was memory allocation; this problem required a minimum of 1.1 GB of random access memory to avoid the use of hard disk space for file usage.

The end result of this simulation showed that the mass flow through the device was 6.92669E-5 kg/s, which is less than one percent above the previous calculation. Therefore, it was determined that 25 nodes per entity would be adequate for these simulations, and this mesh structure would be used for the remainder of this analysis.

8.2 Verification of Initial Simulation

Now that the initial simulations have been performed, it is necessary to verify the CFD results with a physical model. Intuitively, this problem does not have an exact analytical solution, which is why the CFD analysis was performed; however, with a few assumptions, the results of portions of the CFD work can be checked against an analytical model.

The CFD results show that the flow through the channel is subsonic throughout the entire domain. This can be easily verified by examining some of the pressures input to the CFD solver. The flow situation occurring within the flow channel is adiabatic frictional flow without area change, Fanno flow. Therefore, since the flow begins from stagnant air, the maximum flow rate would result in a Mach number of unity at the flow channel exit; below this flow rate, the flow will be subsonic throughout the entire channel [66].

If the flow rate of air through the channel were at this maximum flow rate, then the pressure at the flow channel outlet would have to be greater than or equal to 202 kPa, the pressure at the exit plane of the downstream tube fitting. With the known bound on the static pressure and a Mach number of one, the stagnation pressure can be calculated:

$$P_0 = P\left[1+\frac{\gamma-1}{2}M^2\right]^{\gamma/\gamma-1}$$

$$P_0 \geq 202\text{kPa}\left[1+\frac{1.4-1}{2}(1)^2\right]^{1.4/1.4-1} \geq 382.37\text{kPa}$$

In order for sonic conditions to exist at the exit of the flow channel, the exit stagnation pressure must be greater than 382.37 kPa. This is not possible because the stagnation pressure at the inlet of the upstream tube fitting is 316 kPa, and stagnation pressure can only decrease with friction. Therefore, the flow is in fact subsonic throughout the entire domain.

At this point, it is not possible to analytically determine the mass flow rate through the device; therefore, the approach is to approximate the flow properties based on the one dimensional analytic equations, the mass flow rate of 2.74748E-4 kg/s returned from the CFD solver, and the other known properties. It is known that, since the flow is entirely subsonic, the channel exit pressure is 202 kPa. And, since there is no heat addition, the stagnation temperature is known to be 300 K. Based on these properties and the mass flow rate, a one dimensional analysis can be used to calculate the exit Mach number as shown below.

The mass flow rate is related to the static temperature, static pressure and Mach number

$$\dot{m} = \rho U A_{cs} = \rho C M A_{cs}$$
$$= \left(\frac{P}{RT}\right)\left(\sqrt{\gamma RT}\right) M A_{cs}$$

The static temperature is related to the stagnation temperature through the one dimensional isentropic relationship:

$$T = \frac{T_0}{\left(1 + \frac{\gamma - 1}{2} M^2\right)}$$

Therefore, the mass flow rate is related to the static pressure, Mach number and stagnation temperature through the following relationship:

$$\dot{m} = P M A_{cs} \sqrt{\frac{\gamma\left(1 + \frac{\gamma - 1}{2} M^2\right)}{\mathrm{R} T_0}}$$

Substituting the known values results in a flow channel exit Mach number of 0.647951. With this Mach number, the flow channel exit static temperature is found from the one dimensional relationship:

$$T = \frac{T_0}{\left(1 + \frac{\gamma - 1}{2} M^2\right)} = \frac{300\mathrm{K}}{\left(1 + \frac{1.4 - 1}{2}(0.647951)^2\right)} = 276.76\mathrm{K}$$

And the stagnation pressure at the flow channel exit is found from the one dimensional relationship:

$$P_0 = \frac{P}{\left(1 + \frac{\gamma - 1}{2} M^2\right)^{\left(-\gamma/\gamma - 1\right)}} = \frac{202\mathrm{kPa}}{\left(1 + \frac{\gamma - 1}{2}(0.647951)^2\right)^{\left(-1.4/1.4 - 1\right)}} = 267.8608\mathrm{kPa}$$

The speed of sound at the flow channel exit is:

$$C = \sqrt{\gamma RT} = \sqrt{(1.4)\left(287 \frac{\mathrm{J}}{\mathrm{kgK}}\right)(276.76\mathrm{K})} = 333.47 \frac{\mathrm{m}}{\mathrm{s}}$$

And the one dimensional approximation of the velocity at the flow channel exit is:

$$U = MC = 0.647951 * 333.47 \frac{\text{m}}{\text{s}} = 216.0721 \frac{\text{m}}{\text{s}}.$$

The static pressure that would result if the flow length were increased until choking conditions occur, P^*, is calculated from the relationship:

$$P^* = PM \left[\frac{1 + \frac{\gamma - 1}{2} M^2}{(\gamma + 1)/2} \right]^{1/2}$$

$$= (202\text{kPa})(0.647951) \left[\frac{1 + \frac{1.4 - 1}{2}(0.647951)^2}{(1.4 + 1)/2} \right]^{1/2} = 124.397\text{kPa}$$

At this point, all of the parameters for a one dimensional approximation are known at the flow channel exit. However, it is not possible to use this information for a closed form analytical solution because the integrals involved do not have exact solutions; therefore, the flowfield must be numerically integrated backwards from the exit plane to the flow channel entrance.

The sequence used to solve the parameters in this flowfield is as follows. First, the static density is calculated from the static temperature and static pressure using the ideal gas law. Second, the velocity is calculated from the mass flow rate, cross sectional area, and the density. The third step is to calculate the dynamic viscosity using Sutherland's Law with the static temperature. The fourth step is to calculate the kinematic viscosity using the dynamic viscosity and the density. The fifth step is to calculate the Reynolds number from the kinematic viscosity, the velocity, and the hydraulic diameter. The sixth step is to calculate the smooth tube friction factor using the Reynolds number and the relationship:

$$f = \frac{0.3164}{\text{Re}^{1/4}}$$

Next, the downstream pressure gradient due to friction is calculated from:

$$\frac{dP}{dx} = f \frac{\rho}{D_h} \frac{U^2}{2}$$

Finally, the static pressure at a location one incremental element upstream is then calculated by:

$$P_{upstream} = P_{downstream} + \frac{dP}{dx} \Delta x$$

With this upstream pressure and the Fanno frictional choking pressure, P^*=124.397 kPa, the upstream Mach number is calculated. Once the Mach number is known, the static

temperature and the stagnation pressure are calculated from the one dimensional isentropic relationships. This entire process is marched backwards from the flow channel exit to the flow channel inlet to produce an estimate of each of the flow properties within the flow channel. Figures 8.2 through 8.5 show the one dimensional analytical solution compared to the three dimensional CFD solution at various locations relative to the channel centerline.

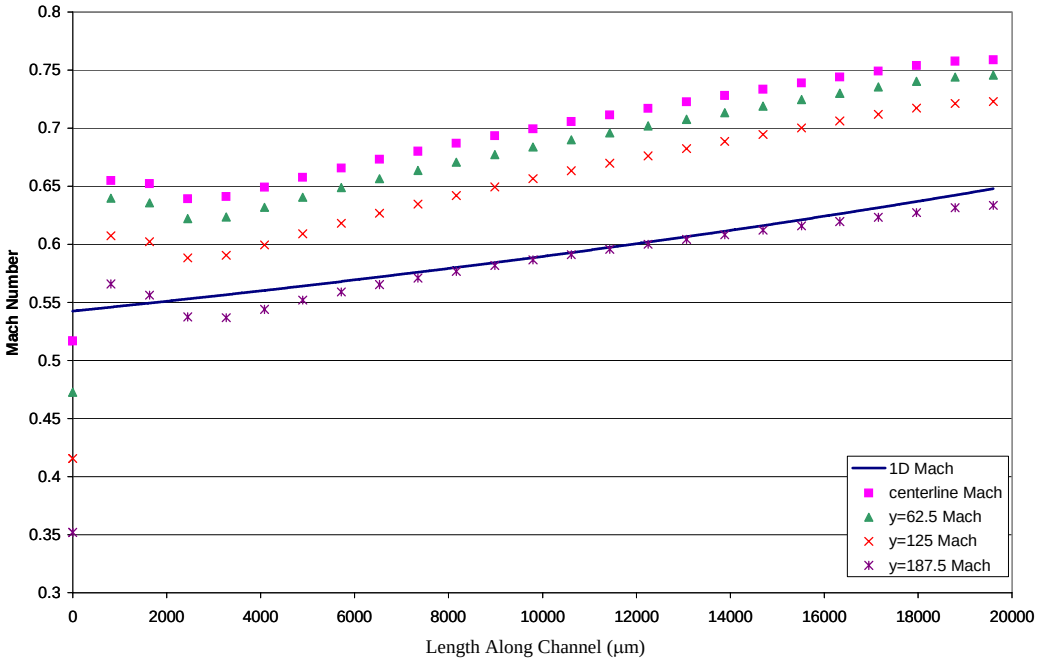

Figure 8.2 Comparison of Mach Number

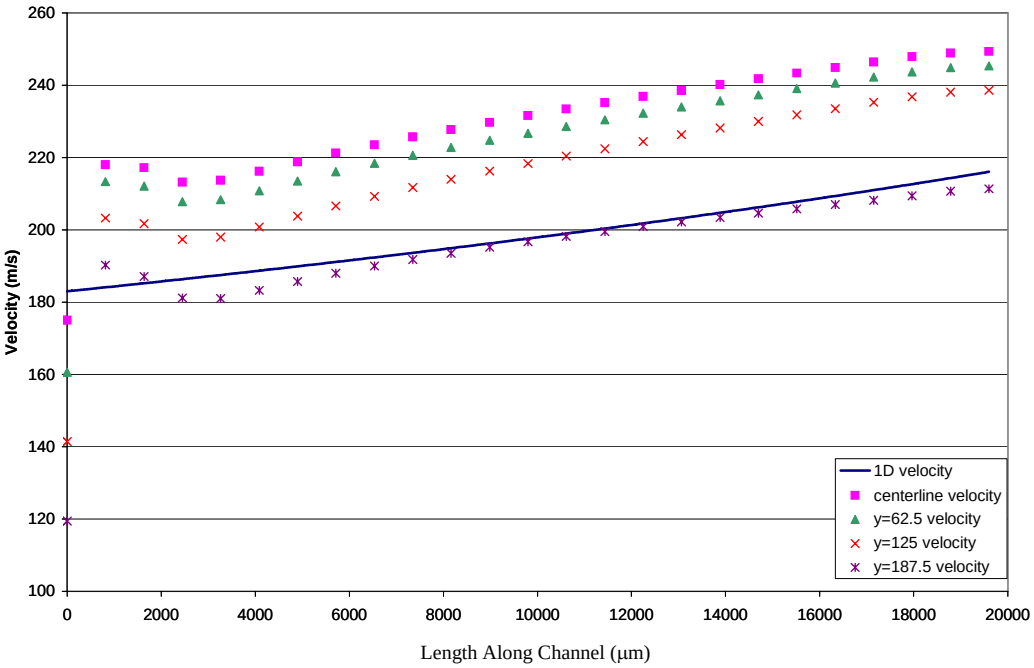

Figure 8.3 Comparison of Velocity

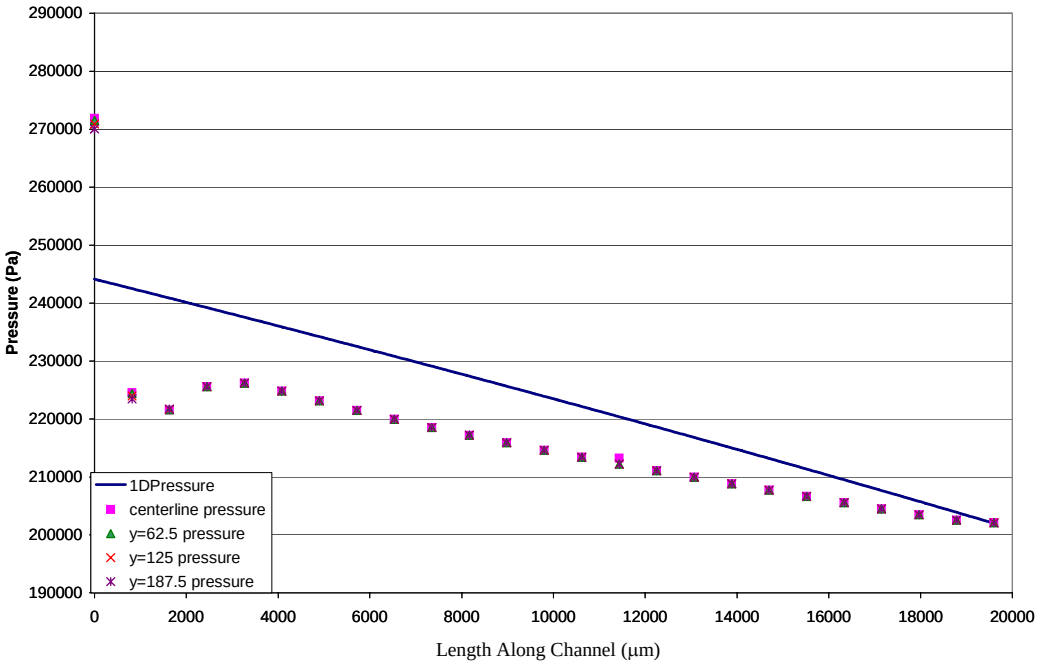

Figure 8.4 Comparison of Pressure

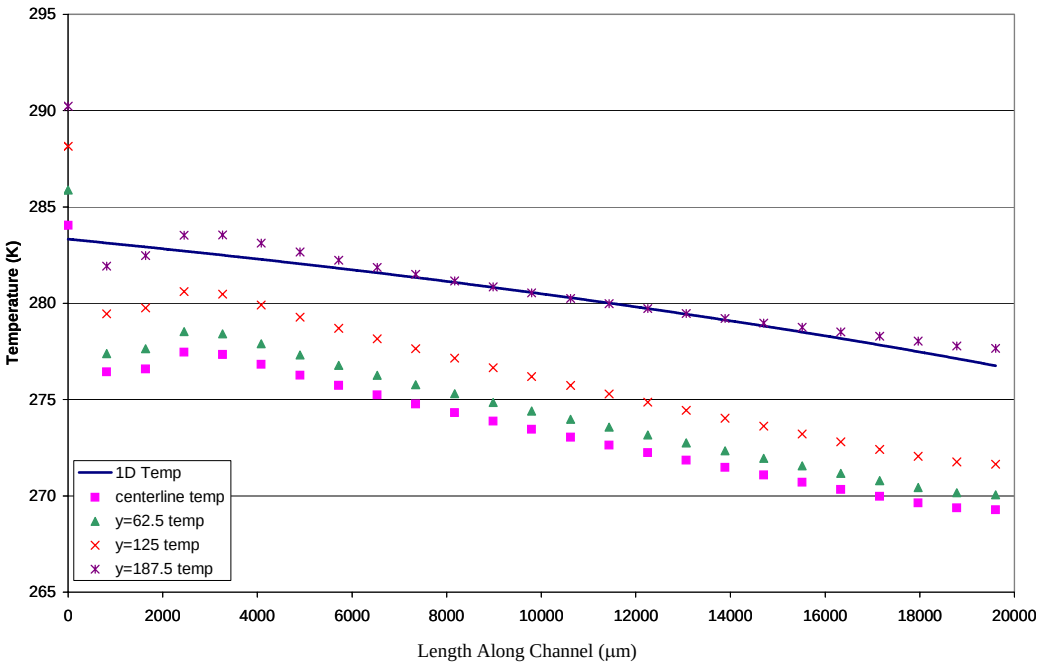

Figure 8.5 Comparison of Temperature

It is seen from these figures that the analytically based solution is generally bounded and in proximity of the CFD solution. The differences are due to the wall effects and the entrance effects which are taken into account in the CFD solution, but not in the 1D solution. This does, however, verify that solutions of this flow situation developed with the CFD solver can be used to predict the flow rate of air through this device.

8.3 Flow Control Prediction Curve

Using the CFD analysis, it was possible to formulate a curve which predicts the flow control ability of the device. The geometry of the device including the flow obstruction was created using pre-processing software package. This time, however, the inclusion of the flow obstruction limited the available symmetrical planes to one.

The flow obstruction was modeled as a cylinder. The width of the flow obstruction spanned the entire width of the channel. In order to fit a continuous grid throughout the flow channel, it was divided into 5 sections; one semi-cylindrical volume at the center of the channel, two volumes upstream of the cylinder, and two volumes downstream of the cylinder. Figure 8.6 below illustrates the geometrical configuration used for these simulations. Figure 8.7 shows a close up of the flow obstruction within the device. Note that the plane of symmetry in this device is towards the rear of the snapshot and that only the upper and lower walls are shaded.

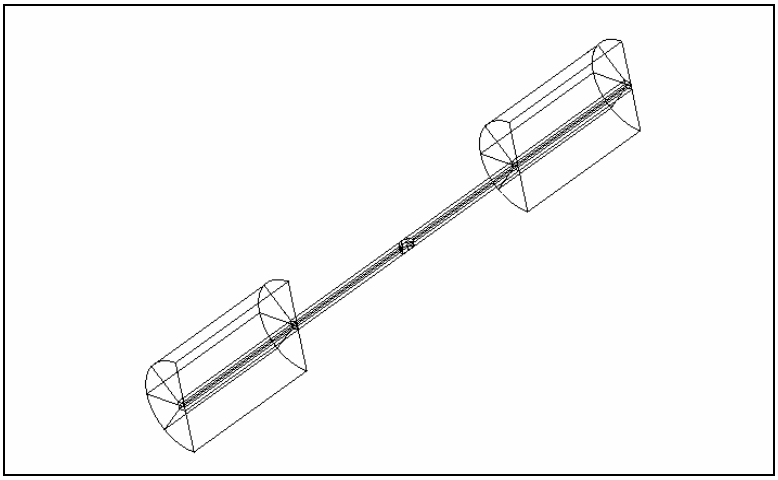

Figure 8.6 Geometry used for CFD Analysis

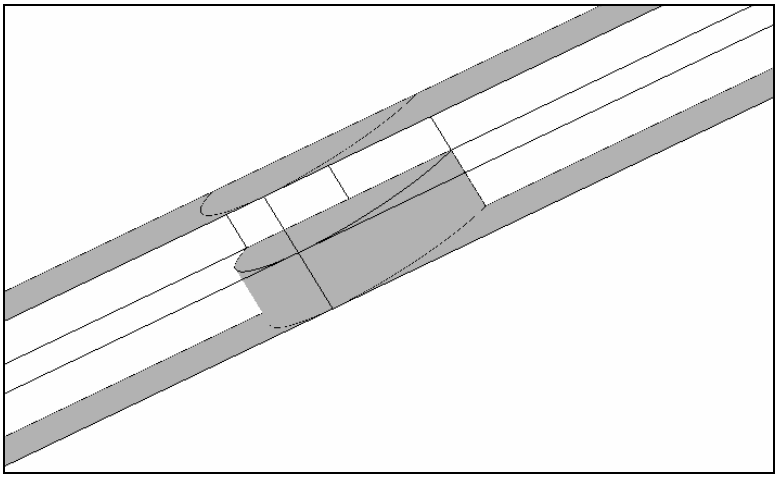

Figure 8.7 Close-Up of Flow Obstruction Geometry

Using a single symmetry plane resulted in a mesh that consists of 17 independent volumes: 5 for the channel as stated above and 6 sections each upstream and downstream representing the device's connection to a 6.35 mm tube at each end. Each entity was again

evenly divided by 25 nodes resulting in 24 sections per entity. Therefore, each volume contained a total of 13,824 cells and each entire configuration consists of 235 008 cells.

Geometries were constructed to determine the mass flow rate of air through the device when the flow obstruction is elevated to various positions. For these simulations, the inlet and exit pressures were held constant at 316 kPa and 202 kPa, respectively. The only variable that was changed was the position of the flow obstruction. The piston positions used to generate a predictive curve are shown below in Table 5.2.

Table 8.2 Test Matrix for Simulations

Obstruction Position (μm)	% Closure of Channel	Comments
0	0	Used information from initial simulation
125	25	
180	36	
250	50	
320	64	
375	75	
500	100	No simulation, mass flow is zero

Unfortunately, due to the nature of the CFD preprocessing package, a new geometry had to be constructed for each position of the flow obstruction position. There was one exception which expedited the generation of the geometries. The flow obstruction is modeled as a cylinder that has a range of motion from zero actuation (forming a continuous boundary with the wall) to fully closed (extending to the top of the flow channel). For any position within this range, there exists a complimentary position. In other words, since the flow channel is 500 μm tall, the geometry created to simulate the situation when the obstruction was 125 μm into the flow can be used to simulate the situation when the obstruction is 375 μm into the flow with very little adjustment. The only changes needed were the addition of a complimentary volume of the piston, and the removal of the original piston.

The speed at which these numerical simulations converged was highly dependent on the initial conditions that were given to the solver. For this reason, the simulations were ran in order of lowest to highest position of the obstruction and the solutions from each run were used to determine the initial conditions for the present run. This provided a good starting point for the solver. The data obtained through the simulations is shown below in Figure 8.8.

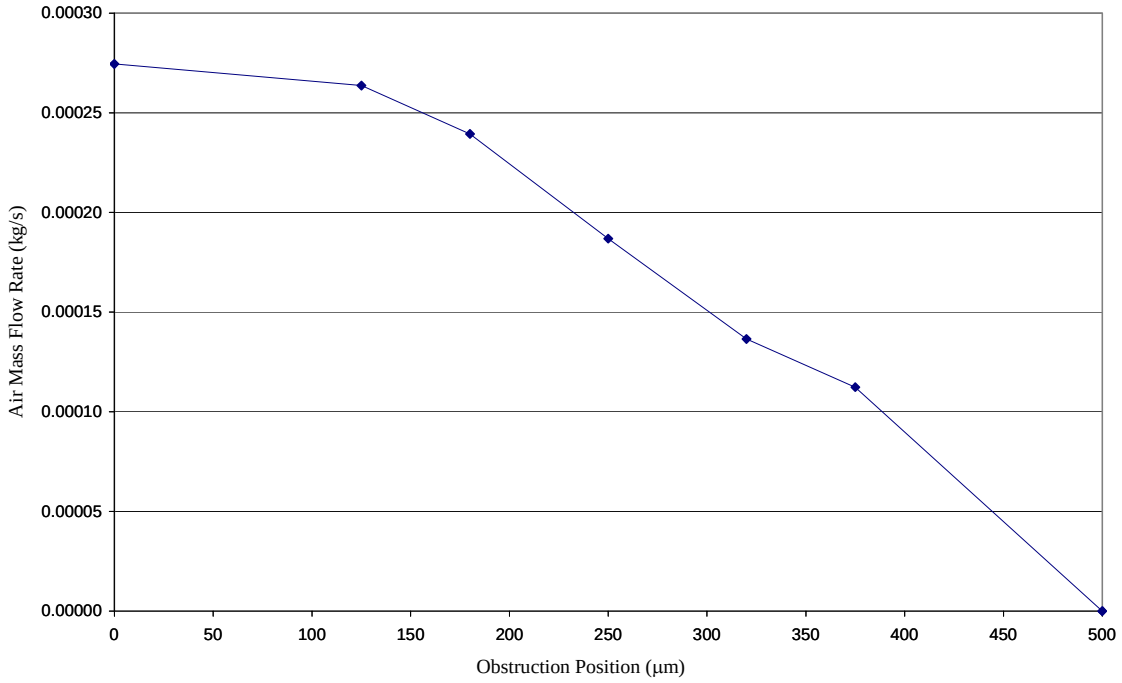

Figure 8.8 Results from CFD Simulations

It is interesting to note that two flow regimes exist over the range simulated with the CFD package. The results from the first two data points, which correspond to zero actuation and a piston height of 125 μm, show a flow regime that is subsonic throughout the entire domain. A transition between flow regimes occurs somewhere between the 125 μm data point and the 180 μm data point. Here, the passage becomes small enough to choke the flow between the piston top and the upper channel wall. For any level of actuation beyond this transition point, the flow rate is directly related to the cross sectional flow area or 500 μm less the obstruction position.

CHAPTER 9
Gas Flow Measurements

9.1 Flow Control Measurement

Once the prototype was assembled, its ability to control flow was demonstrated in the compressed air test apparatus. To do this, a pair of 6.35 mm copper tubes were glued to the ends of the flow channel and it was connected to the test apparatus.

The objective of these tests was to measure the flow rate of air through the prototype for a varying position of the piston, while holding the inlet and exit pressure constant. Measurements were performed on four separate occasions. Each set of measurements was taken by increasing the oil temperature from 22.9 ºC to 44.8 °C in small increments. At each increment, a measure of the air flow rate was taken, 19 points in all.

The supply and back pressures were held as close to 316 kPa and 202 kPa as could be attained with manual control. In all cases, the supply pressure was less than 317.6 kPa and greater than 312.5 kPa; the back pressure was between 204 kPa and 200 kPa. These conditions correspond to those in the CFD simulations. The data collected during these tests and the corresponding measurement uncertainty is shown below in Figure 9.1. The data for these tests is in Appendix B.

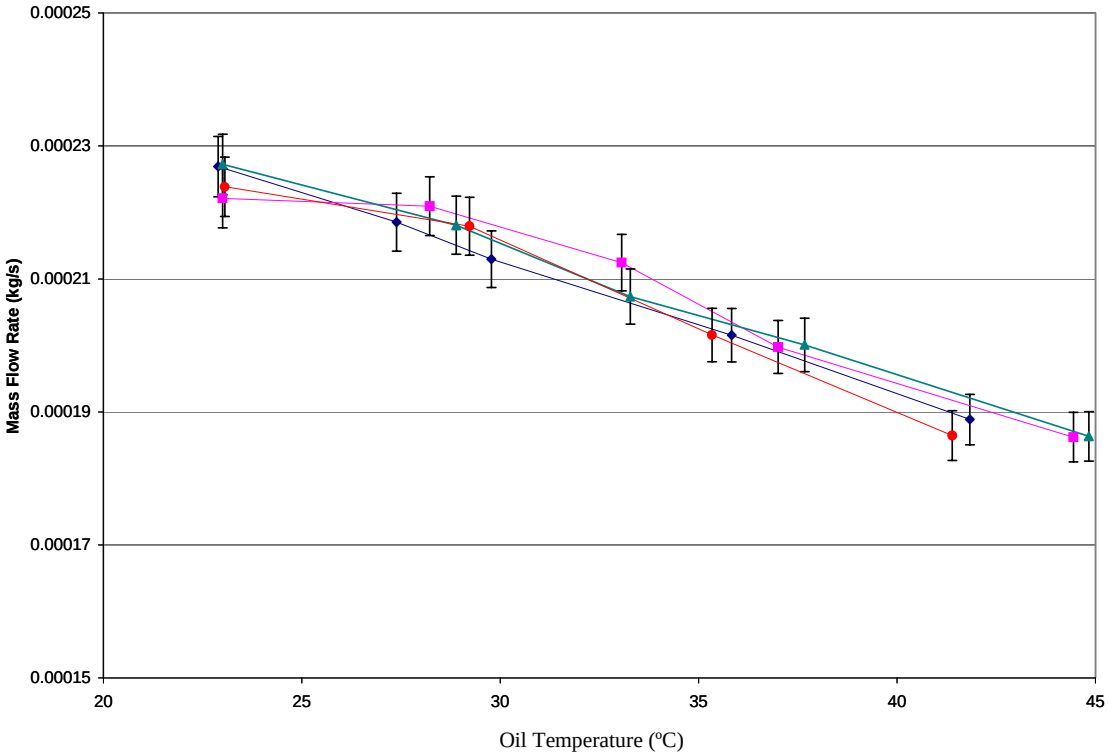

Figure 9.1 Results of Air Flow Measurements

These measurements show that the air flow rate was reduced by 22 % as the piston was pushed into the flow channel. Using the curve generated for the relationship between the oil temperature and the piston position, the range of operating temperatures corresponds to piston positions ranging from 0 μm to 300 μm above the floor of the channel. All things considered,

the flow rate of air through the device proved to be quite reasonable. This demonstrates that the prototype can induce the marginal flow resistance on demand.

9.2 Comparison to CFD Simulations

The results of these air flow measurements are shown below in Figure 9.3 compared to the results of the CFD analysis.

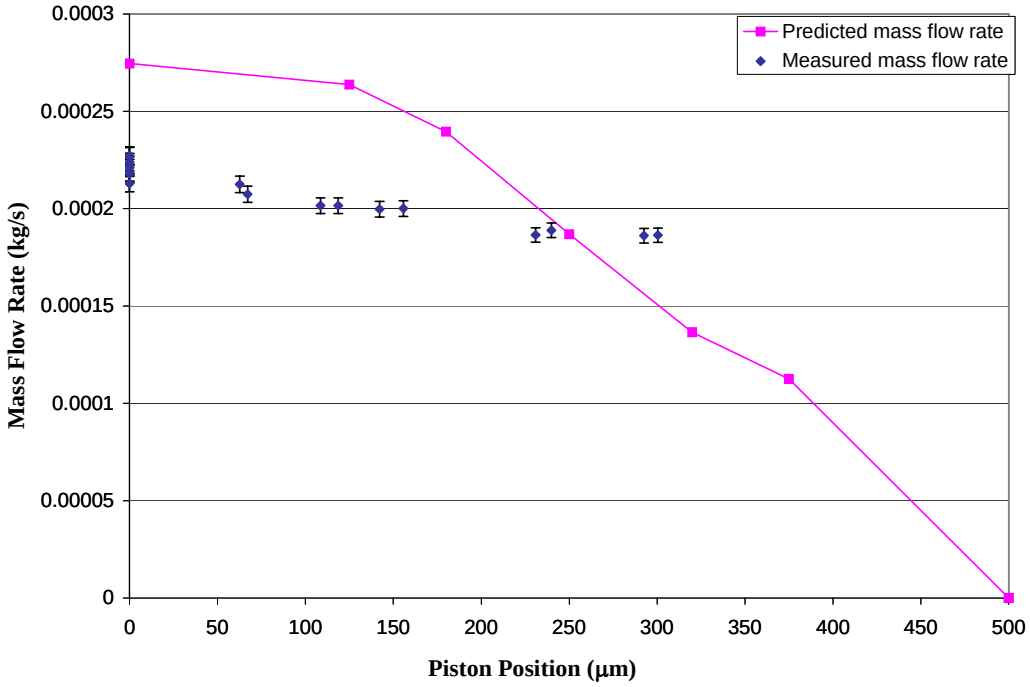

Figure 9.2 Comparison Between Gas Flow Measurements and CFD Analysis

Comparison of these measurements to the CFD simulations gives a lot of information about the device. First of all, it is seen that the measured air flow rate at low actuation is 17 % less than the simulated value. This is because the simulated device dimensions were different than those of the actual device. The simulated geometry was a rectangular cross section with a width of 1 000 μm and a height of 500 μm, which results in a cross sectional area of 500 000 μm^2. The fabricated device is has a slightly different configuration with a cross sectional area that is 14 % less than that of the simulated device. The difference in the flow rate of the fully open device is attributed to this.

Another difference between the simulated and measured data is seen by the trends is the data. The slope of the simulated data changes in the vicinity of 150 μm piston displacement, whereas the slope of the measured data does not change significantly over the range of data. This difference is because of the fact that the piston, as fabricated, does not entirely block off the flow channel, as it was modeled in the CFD work. In other words, the discontinuity in the boundary introduced by the piston is affecting the flow, but it does not restrict the flow in the same manner. The CFD analysis showed that, at a certain level of actuation, the flow became choked. Once the flow is choked, the mass flow rate should be directly proportional to the cross sectional flow area, which is inversely related to the piston displacement. This is why, at a

certain level, the CFD results show a change in the relationship between the mass flow rate and the displacement. The measured results do not show this shift in flow regime because the piston is not seal off enough of the flow path to choke the flow; but it does affect the mass flow rate through protrusion and area reduction.

Chapter 10
R134a Vapor Compression Test Results and Discussion

This chapter presents the results of the device's ability to control flashing of R134a within a vapor compression system. We performed to measure the mass flow rate of the refrigerant passing through the device under conditions similar to those that would occur in a household refrigerating appliance using the vapor compression test apparatus described in Chapter 3. We took two sets of test data, the first data set demonstrates steady state performance with a fixed set of operating conditions, the second data set shows the HVAC system's response to the device's actuation.

It needs to be noted that the pressure that the device is subject to in the vapor compression system is considerably higher than the pressures used in the air flow test bench; therefore precautions were taken to ensure proper operation prior to inserting the device into the vapor compression system. To do this, the connections to the 6.35 mm copper tubes were reinforced with multiple layers of epoxy. Also, to help prevent the pipe connections from leaking, the upstream pressure used during testing was slightly lower than most HVAC&R applications. Typical household refrigerating appliances have a design liquid line pressure of approximately 963 kPa, which corresponds to a condensing temperature of 38 ºC. For these measurements, the liquid line pressure was kept at 750 kPa for the steady state tests, which corresponds to a condensing temperature of 29 ºC, and slightly lower for the transient response tests. All raw test data is in Appendix C.

10.1 Steady State Operation

The condenser exit pressure was held constant at 750 kPa, while the level of liquid line subcooling was varied by changing the condenser HTF temperature and adding or removing refrigerant from the system. The evaporator HTF inlet was held constant at 4 ºC.

Two levels of actuation were used to characterize the operation of the device, corresponding to high and low levels of interaction between the piston and the flashing refrigerant. For the low actuation level, the measured oil temperature in the device was held constant at 25 ºC, which corresponds to no actuation; while the measured oil temperature was held at 40 ºC, corresponding to a piston height of 202 μm for the high actuation level tests.

A total of 781 data points were taken to characterize the steady state operation of the device under constant inlet pressure, two different levels of actuation, and a range of subcooling. Figure 10.1 shows the results of these measurements.

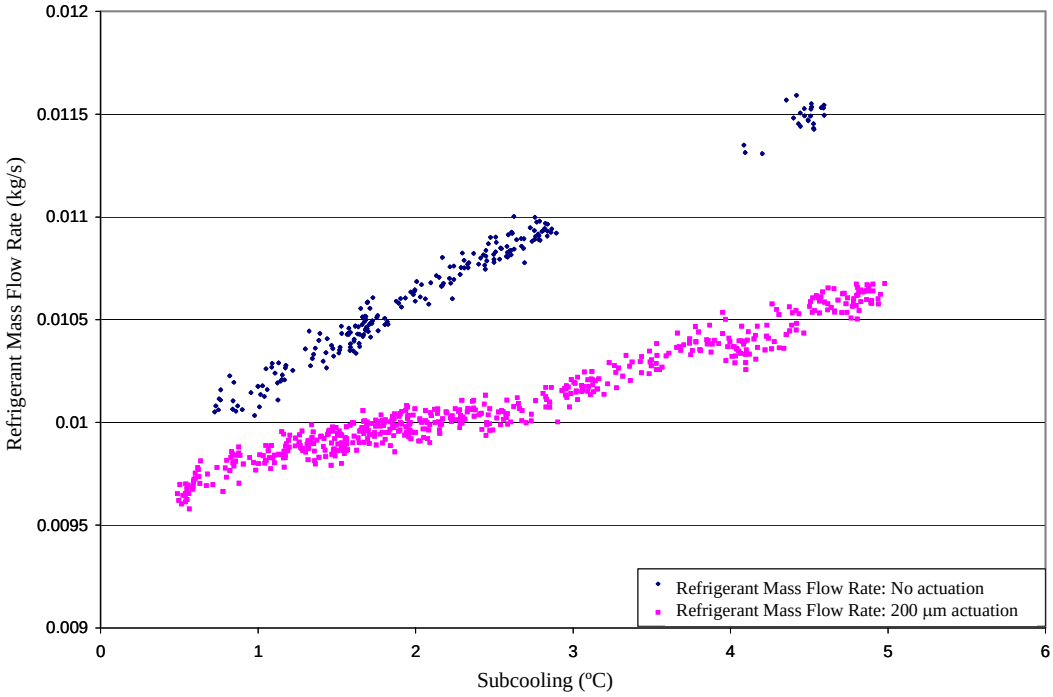

Figure 10.1 Steady State Refrigerant Mass Flow Rate for Two Levels of Actuation (750 kPa inlet pressure)

It is interesting that the effect on the mass flow rate from actuating the device seems to be strongly related to the level of subcooling. At low levels of subcooling the effect is very small, showing on average 3.5 % difference at 0.6 ºC subcooling. As the level of subcooling is increased, so is the impact of the device's actuation; at 5 ºC subcooling, there is a 10.7 % difference in the refrigerant mass flow rate.

10.2 Quasi-Transient Operation

The second set of data seems to give a bit more information, as it depicts the system's response to the device. For these tests, the power to the device's electrical resistance heater was abruptly switched up and down, and the system's response was recorded. For these tests, three power-up periods were input to the device, with progressively higher power each time until the maximum output of 2.75 W from the heater was reached. The three power-on periods brought the measured oil temperature from 25 ºC up to 46 ºC, 49 ºC, and 52 ºC, respectively, which correspond to actuation levels of zero up to 324 μm, 384 μm, and 445 μm. For the initial operation, the condenser exit conditions were approximately 725 kPa with 4 ºC of subcooling.

Figures 10.2 through 10.4 depict the system response to the changing valve oil temperature. Figure 10.2 shows the change in condensing pressure and subcooling, Figure 10.3 shows the change in refrigerant mass flow rate and system capacity, and Figure 10.4 shows the response of the evaporator exit superheat. The measured quantities in Figures 10.2 and 10.3 are normalized to each parameter's maximum value to better illustrate the change in each of the quantities.

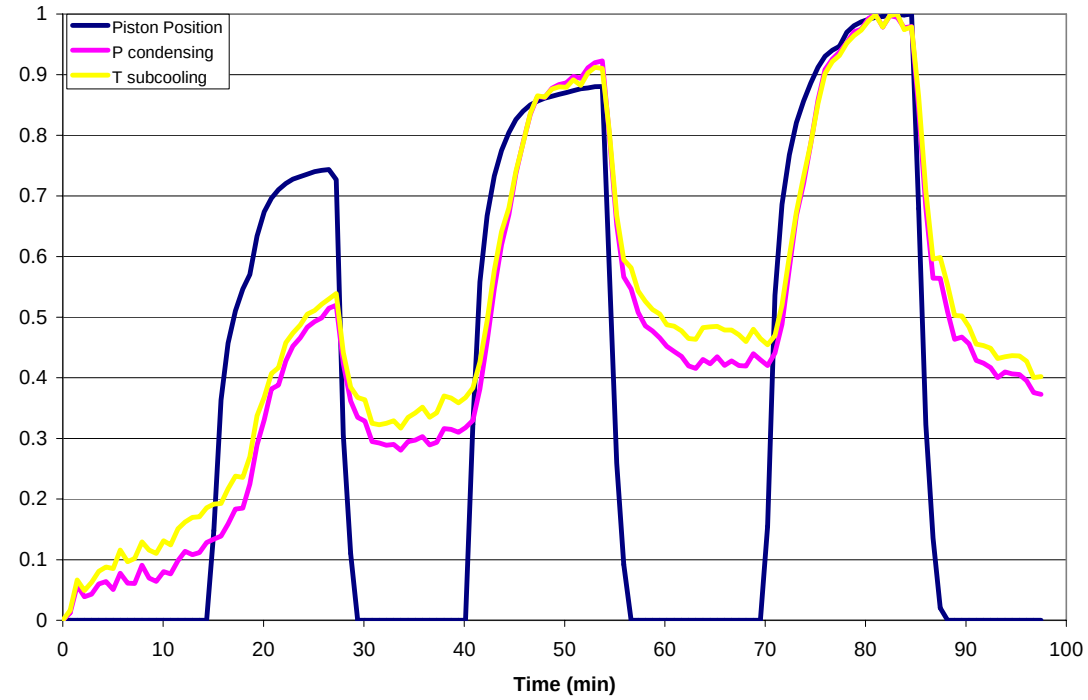

Figure 10.2 System Response – Normalized Piston Position, Condensing Pressure, and Subcooling

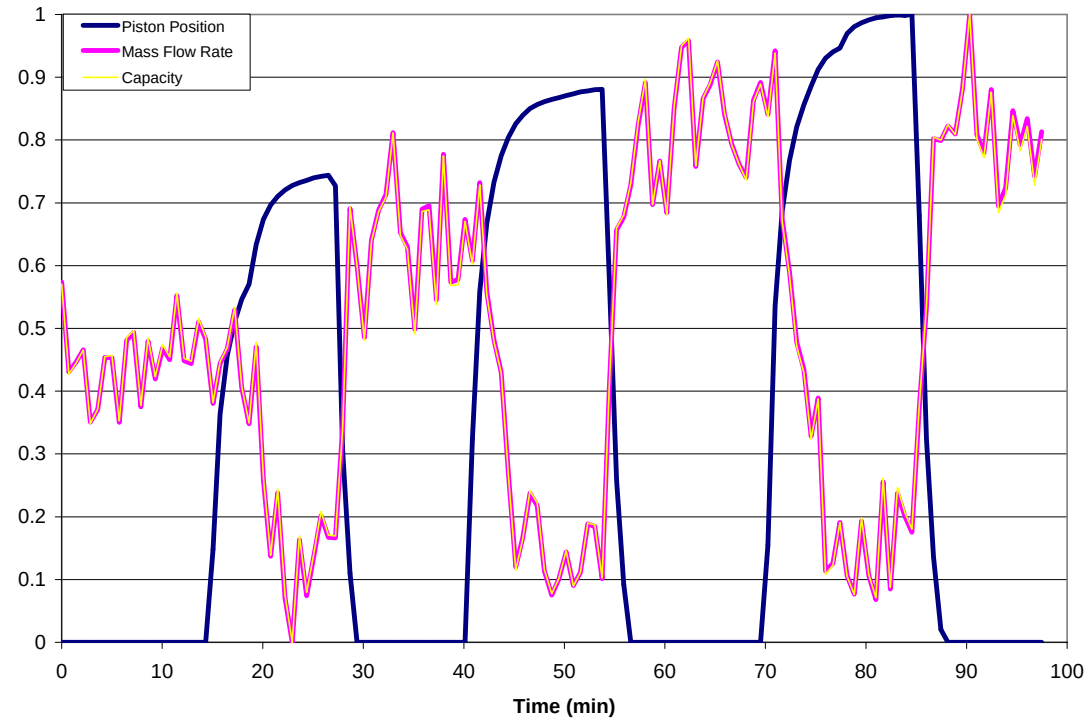

Figure 10.3 System Response – Normalized Piston Position, Refrigerant Mass Flow Rate, and System Capacity

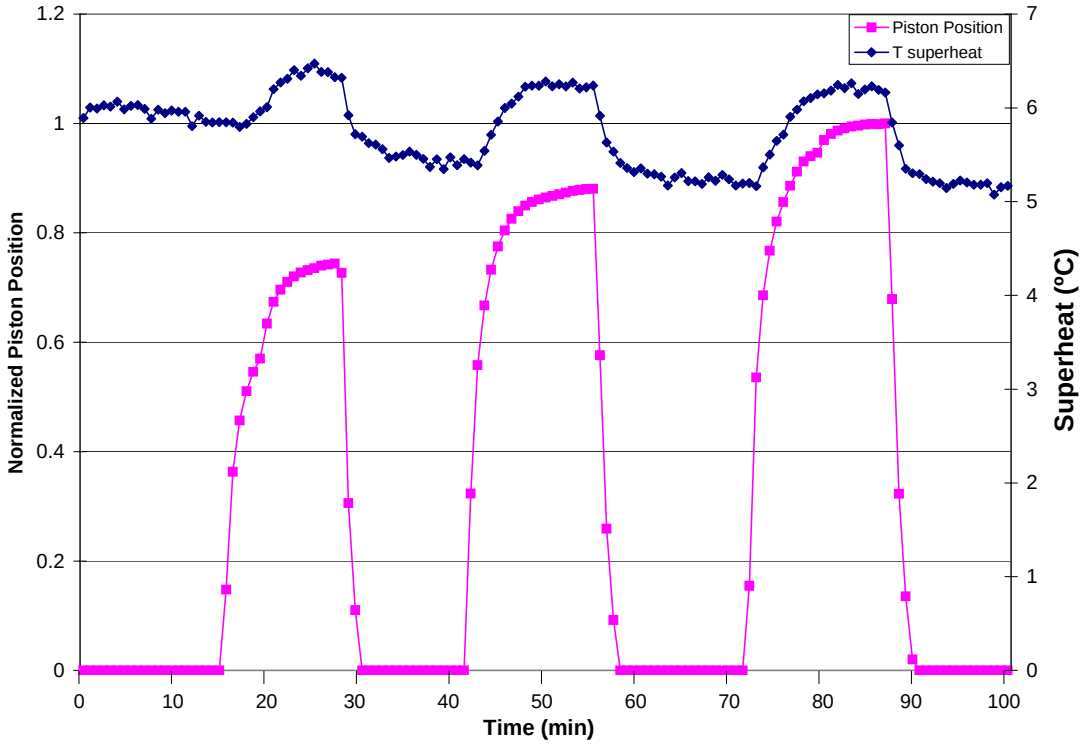

Figure 10.4 System Response – Evaporator Exit Superheat and Normalized Piston Position

The qualitative system response to the change in oil temperature is as would be expected. Heat is added to the oil reservoir in the device, which causes the piston to move into the refrigerant flow path, thereby creating a more restrictive metering device. This, in turn, reduces the refrigerant mass flow rate and therefore system capacity. This reduction in mass flow rate causes more refrigerant to accumulate in the condensing portion of the system which, in turn, causes the condensing pressure and subcooling to increase. Since less refrigerant remains in the evaporator, each unit of refrigerant that passes through evaporator must absorb a little more energy and therefore its exit temperature is higher.

Quantitatively, however, the system response is somewhat diminished by the changing operational parameters. The quantitative system capacity is shown below in Figure 10.5.

.

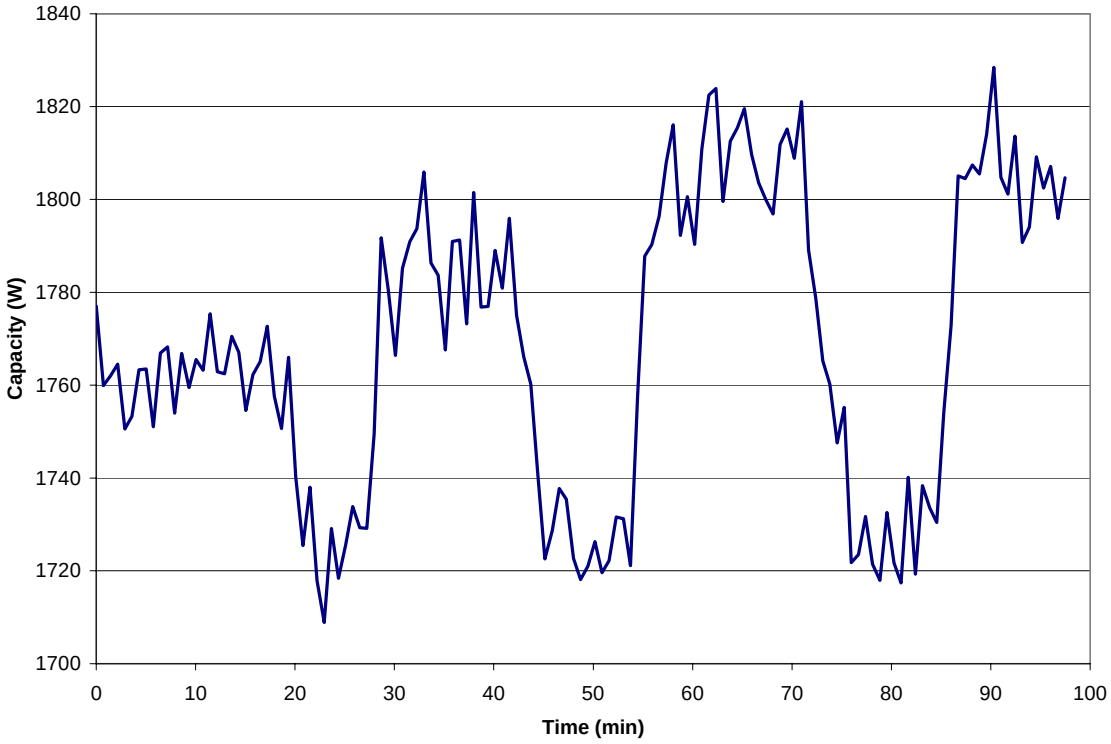

Figure 10.5 System Capacity in Response to Device Operation

10.3 Discussion

It is shown in the figure above that the change in system capacity is approximately 5 %, when comparing the low and high actuation levels. Since this work represents a very preliminary look into the way flashing refrigerant responds to this new geometrical configuration, it is not surprising that the magnitude of the shift is in this range. There are a few factors that can help explain why the magnitude is in this range.

The first reason has to do with the way that the oil temperature is measured. The capsule consists of a brass tubular section, approximately 33.0 mm in length with a diameter varying between 7.0 mm and 11.0 mm. Within the capsule are an electrical resistance heater and the tip of a thermocouple probe, with the probe aligned to the centerline of the tubular section. The oil in the capsule has a relatively low thermal diffusivity, as was discussed in Chapter 8, and the brass walls of the capsule have a large thermal conductivity. The inherent obstacle to obtain a good measurement of the overall average oil temperature is the thermal gradient within the capsule.

The oil in the reservoir rejects heat through the brass wall of the reservoir, which causes the oil near the walls to be colder than that along the centerline, where the thermocouple probe is placed. Furthermore, since the top of the capsule is kept cold by contact with the flashing refrigerant and the capsule itself is a very good thermal conductor, all of the walls of the capsule will be near the refrigerant flashing temperature. For this reason, a temperature measured at the centerline of the oil reservoir during operation in the vapor compression system will be warmer that the true average oil temperature. It is apparent from the data shown in Figures 10.2 through 10.4 that this may be a factor because the illustrated properties all begin to change when the piston position, based on the measured oil temperature, is around 200 μm. Since any interaction

between the piston and the refrigerant should impart some change in these properties, it is logical that the measured oil temperature must be a little warmer than the average oil temperature.

The exact relationship between the measured and true average oil temperature, however, is not known. When performing the measurements to obtain the relationship between measured oil temperature and piston displacement, an attempt was made to hold the top of the device at a 5 ºC (similar temperature to the test data flashing temperature) by packing the tube connections is dry ice. This, however proved to be a very difficult task and good data could not be obtained, therefore the relationship shown in Figure 6.22 was used.

The second reason for this level of response is that width of the piston, as fabricated, is smaller than the width of the flow channel, and therefore does not completely block off this area. As fabricated, the piston blocks off 81 % to 83 % of the width of the flow channel, depending on orientation. Therefore, at the highest piston elevation experienced in these tests (again based on the measured temperature – position relationship), the maximum blockage is approximately 73 % of the flow channel.

The third reason for the small change in capacity is the compounded effect of the increased inlet pressure and increased subcooling. The behavior of this device is, in general, similar to that of a short tube restrictor; and the flow rate through a short tube restrictor is strongly influenced by the inlet pressure and the level of subcooling.

When the device is actuated, the condensing pressure increases and the evaporating pressure decreases. This is due to the migration of refrigerant from the low pressure side of the system to the high pressure side. With any type of flow metering device, the pressure differential across the device is the driving potential for the flow, and therefore raising the condensing pressure and lowering the evaporating pressure will increase the potential (although with short tubes the evaporating pressure is not very influential). This is a common obstacle for all flow controlling devices.

The subcooling, however, is not an obstacle for most other types of flow controlling devices. Needle valves and traditional boss-and-valve-seat type devices, which are the general basis for most other types of flow restricting devices, are not affected by the level of subcooling in the upstream liquid line, provided that the flow is not two phase at the entrance of the device. This is because the refrigerant is flashed at the exit plane of these devices due to the abrupt changes in flow area and geometry. The flow through the device is single phase throughout, and the thermodynamic properties relative to saturation are not a factor in the flow.

With short tube restrictors, however, subcooling is one of the most important parameters governing the flow [67]. In typical applications, subcooled refrigerant enters a short tube, and a large pressure reduction is realized due to the abrupt area change. As the refrigerant flows through the short tube, the pressure is further reduced through friction until the exit plane. Within this portion, some of the refrigerant changes phase to vapor. When phase change occurs, the flow begins to exhibit some properties similar to choked flow. It is not choked, per se, but it exhibits some behavior similar to that of choked flow; the flow is relatively insensitive to, but not completely independent of the downstream pressure. In typical HVAC&R short tube applications the liquid density of a fluid inside a short tube is approximately 100 times that of the vapor density. Furthermore, the speed of sound is about 4 times faster in liquid than the vapor phase. Therefore, the generally accepted theory is that as some of the liquid refrigerant begins to change phase to vapor, the Mach number of the phase changing particles increases by a factor of approximately 400. This is a relatively crude approximation because liquid-vapor interactions exists, however the order of magnitude is important here. This vast increase in Mach number

generally brings the vapor phase of the flow to sonic conditions. The two phases flow together and the vapor phase is choked but some downstream information is able to propagate upstream within the liquid portion; this phenomenon is termed "approximately choked" flow.

If the liquid refrigerant entering the short tube has a large degree of subcooling, it must undergo a substantial reduction in pressure before liquid particles begin to vaporize. Once vaporization begins, the mass flow rate through the device is somewhat limited. Therefore, the level of subcooling determines when and where the transition to vapor begins, and therefore has a profound impact on the mass flow rate.

Due to the fact that the upstream pressure and subcooling both increase when the device is actuated, two driving potentials for the flow are increased and the overall impact of the increase restriction is lessened.

For the measurements in Chapter 9, it was demonstrated that this device could change the mass flow of air by approximately 22 % with 300 μm piston elevation. However, the underlying physics of flow with liquid to vapor phase change is vastly different from single phase gaseous flow. With this type of flow, the piston interaction will cause a significant pressure drop within the device, which will certainly impact if not be the cause of the onset of the liquid to vapor transition. The data shown in Figure 10.1 shows that the flow through the device with some piston actuation is less sensitive to subcooling than the flow through the unactuated device. A possible explanation is that the location of the flow's liquid-to-vapor transition point is fixed by the piston, which would limit the subcooling's effect on the mass flow rate.

However, given all of these effects the fact does remain that in the case of the measurements shown in Figure 10.5, a device input of 2.75 W of power was able to change the system capacity by approximately 100 W, and this may be a sufficient level of modulation for some applications. Different operating conditions will, of course, produce different results.

10.3.1 Subcooling Influence

It is known from the steady state data that, although greater subcooling results in greater mass flow, the loci of points from the actuated device vs. those of the unactuated device diverge. In other words, the influence that subcooling has on the mass flow rate is greatly reduced when the device is powered on. Therefore, during transient operation, when the device is powered up, the piston will engage the flow in the short tube which will increase the restriction. This will, in turn, increase the subcooling which increases the driving potential for the flow. However, since the slope of the actuated device's mass flow rate vs. subcooling (Figure 10.1) diverges from that of the unactuated device, the impact that the device has on the mass flow rate will be greater if the initial degree of subcooling is high. Therefore, operation with a larger degree of inlet subcooling at a given inlet pressure would allow the device more control over the system.

10.3.2 Inlet Pressure Influence

By selecting data points from the quasi-transient data that correspond to the same level of subcooling while in the hot and cold position, and comparing this to the steady state data, we can see that the inlet pressure will also affect the level of influence that the device will have on the flow. Figure 10.6 shows four data points that were measured with a constant subcooling of 4.6 ºC.

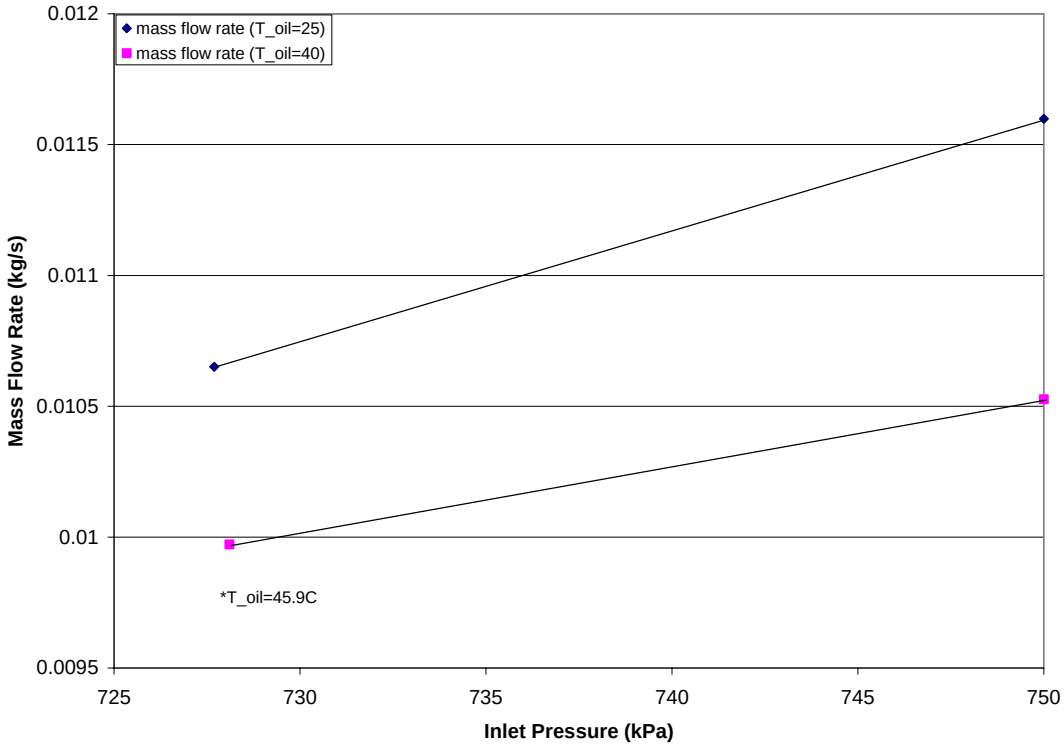

Figure 10.6 Mass Flow Rate vs. Inlet Pressure for 4.6 ºC Subcooling

These four points are shown with the mass flow rate plotted against the inlet pressure. We can see from this figure that as the pressure increases, the two curves diverge. Note that the low pressure, high actuation data point was measured with an oil temperature of 45.9 ºC, not 40.0 ºC, and therefore the difference between the slopes of the curves is actually larger than what is depicted, since an oil temperature of 40.0 ºC would result in greater mass flow than the data point shown above. Since these curves diverge as the inlet pressure is raised, the device's influence on the flow of refrigerant will be better at higher pressures than at lower pressures.

10.3.3 Temporal Response

The quasi-transient data also gives some insight into the transient response of the device. The data acquisition system requires a total of 40 s to multiplex through each channel and there is a 3 s delay between successive scans, therefore the total time lapse between successive scans of each channel is 43 s. The device's thermal time constant is determined from this data in the same manner as was done in Chapter 7 of this report. First, a section of the data was selected to encompass the power-up response of the device. For this analysis, only the third power-up sequence from the data in Figure 10.2 was used because the power was adjusted slightly during the other two sequences.

The data points which correspond to the first two scans after the obvious point of the heater switch were discarded. This is because exact time that the heater was switched on relative to the successive multiplexer scans is unknown. Next, the natural logarithm of the difference between the final steady state temperature and each scanned temperature was plotted against the elapsed time. This locus was fit with a straight line using a least squares regression, and the final temperature was adjusted until the highest R^2 value was obtained. This resulted in a final high

power temperature of 51.1 ºC and a thermal time constant of 126.5 s, the R^2 for this linear fit was 0.998. This measured time constant is within 11 % of the value from the simulations of 114.2 s. This is remarkably good considering all of the differences between the actual device and the simplified estimations used in the simulations.

The geometry used in the simulations was a simple tubular section of oil surrounded by a brass cavity, with a heavy brass weight near the bottom. The actual device's oil capsule consists of at least four different diameters within the capsule.

The heat source used in the simulations consisted of a very thin heater located along the centerline of the device. In fact, the heater that was actually used in the capsule was fitted into the capsule and consequently took on the circular shape of the capsule; therefore the heat in the actual device was added into the oil near the outer edge of the reservoir rather than along its centerline.

Finally, isothermal boundary conditions at the outer edges of the capsule were used for the simulations. The isothermal boundary condition of the top of the nickel membrane is probably fairly accurate, since the flashing refrigerant has an extremely large convection coefficient, but the boundary condition around the outside of the brass capsule is probably not very accurate. Since brass and nickel are very good thermal conductors, thermal energy in the brass would tend to leave the system readily via conduction to the nickel membrane. Instead, a simplified isothermal boundary condition was used for the outer edge of the brass. The true exit path of thermal energy in the brass must be two-fold, through the outer edge of the brass capsule into the ambient and through conduction to the nickel membrane; therefore, a more accurate simulation solution would lie somewhere between the case simulated in chapter 7 and a case where the outer edge of the brass were treated as perfectly insulated, forcing all of the heat loss through the nickel membrane.

It is obvious from the simulation results' temperature distribution that this should not have much of an effect on the time constant, since the overwhelming majority of the heat transfer resistance between the heat source and sink occurs within the oil. This is confirmed by the time constant measured in the test results. The parameter that is greatly affected is the relationship between heat input and the device's final temperature. The simulation results estimate that the oil temperature should increase by 39.5 ºC for every one watt of power input; whereas the actual measured temperature was considerably colder in the laboratory measurements. The warmest oil temperature was experienced during the quasi-transient tests; the oil temperature reached 51.86 ºC at the maximum heater output of 2.75 W. According to the estimate from the simulation work, power input of approximately 0.77 W should bring the oil temperature to this level. This is the result of the actual heat sink being greater than that modeled in the simulations.

10.4 Summary

The results of this section show the device's ability to modulate the expansion of refrigerant passing through it. Steady state data was taken to map the flow rate for a given inlet pressure. These results showed that the device has greater influence over the flow when the refrigerant inlet subcooling is high. Next, quasi-transient measurements were taken to depict the HVAC system's response to the device's actuation. The results of the steady state and quasi-transient were used to further understand the inlet conditions that impact the device's ability to control the mass flow rate.

Next, information from the quasi-transient measurements was compared to computer simulations. The data showed that the computer code predicted the device's time constant fairly

well, but the assumed thermal boundary conditions used in the simulations resulted in an estimate which underpredicted the amount of heat loss. Therefore, the actual level of increased temperature was not as high as that found in the simulations.

CHAPTER 11
Summary and Future Work

11.1 Summary

The design, fabrication and testing of a microfabricated thermopneumatic refrigerant expansion device is presented in this work. An initial prototype of this device was fabricated out of silicon using deep reactive ion etching. A vapor compression system test apparatus was constructed and outfitted with measurement equipment, and testing of the silicon prototype was attempted. Based on the findings of this experiment, changes were made to the device's design and material to improve the reliability and ease of assembly.

The material of the device was changed to nickel, which is a more ductile material than silicon, thereby reducing the chance of fracture. A process for forming micromolded nickel pieces with characteristic heights of 150 μm to 1.2 mm was developed as part of this project. Traditionally, the drive for new fabrication techniques has focused on moving towards smaller, better tolerance features in order to produce lighter, faster responding products. Through this motivation, however, the difficulties associated with meso-scale fabrication techniques are often neglected. Fabrication processes were developed to make thick layer nickel electroplating within SU8 micromolds a feasible option with inexpensive processes. Until recently, very little work had been done with SU8-nickel micromolding in the meso-scale. Many obstacles were overcome to develop these processes.

A second test apparatus was constructed to characterize the performance of the device using compressed air. There are two reasons for this second test method. First, it is not possible to analytically or numerically calculate parameters associated with refrigerant expansion through this device. Using compressed air flow instead of refrigerant expansion as a test bench allows for a basis of comparison to computational fluid dynamics (CFD) simulations. Secondly, using compressed air instead of a refrigerant is less stressful on the device, which is desired during the developmental stage.

Optimal fabrication process parameters for this device were determined and a working prototype was fabricated. The prototype components were characterized to document the capabilities of these new fabrication techniques.

Three dimensional CFD simulations were performed on the flowfield within the device at various levels of actuation to predict the device's ability to control mass flow rate of compressed air. The assembled prototype was demonstrated on the air flow test bench and the results were compared to the CFD results.

A numerical code was developed to determine the device's temporal response. Simulations were performed with this code at various levels of power input to the device and the results were used to determine the device's time constant and relationship between actuation level and power input.

Next, the device was tested in an R134a vapor compression system. Both steady state and transient tests were performed. Testing in the vapor compression system showed greater heat input to the device was necessary to overcome the heat loss to the refrigerant to improve mass flow rate control. The steady state tests showed that the level of flow control is strongly dependent on the refrigerant subcooling. The transient tests were performed to demonstrate the HVAC system's response to actuation of the device, and to benchmark the device's time constant. The measured time constant matched well with the calculated time constant from the

temporal response simulation code; but the relationship between the actuation level and power input was offset by the device's refrigerant heat sink.

11.2 Significant Contributions

A number of significant contributions were made through this effort. The development of this flow metering device is a novel contribution. This device was designed to be used as the main throttling device in a small HVAC&R system, where traditional active expansion devices are too large or too costly. However, it was also demonstrated with compressed air and due to the structural and material integrity of this device, it may be used to vary the flow rate of many fluids in many different flow scenarios.

This device works on the principle of introduction or removal of a boundary discontinuity which can be applied to numerous situations. As demonstrated in this work, this principle can be used to vary the flow rate of a passing fluid. However, this principle can also be used in external flow situations by assembling the device without the top piece, i.e. so that the lower flow channel wall is the uppermost piece. This concept could be used for vortex generation or to encourage laminar to turbulent boundary layer transition.

Theoretical and numerical descriptions of the device were derived to predict the motion of, the stresses within, the flow rate through, and the temporal response of the device. These efforts provide tools for future engineers to continue this work with a map of how different materials and alternate dimensions affect the response.

Lastly, fabrication steps were developed to enable the deposition of very tall SU8 layers. This method was used to prepare molds with depths as deep as 1.2 mm, which were then filled with metal through electrodeposition. Through this work an inexpensive UV lithography method to create meso-scale structures has been contributed.

11.3 Future Work

In order to bring this device to a usable standard within industry, a considerable amount of work must be done. First, the prototype tested during this effort demonstrated a lot of the difficulties inherent to initial designs. A number of the auxiliary components should be redesigned to improve the performance of this device.

One major shortcoming was due to the uncertainty of the actual piston position within the flow path during actuation in the vapor compression system. The piston position was measured in relation to the oil reservoir temperature under ambient conditions, but the relationship between the oil temperature and position in the system could not be determined very well. A method of benchmarking this relationship should be devised and used to help describe the fluid mechanics occurring within the flow channel.

The oil used for this prototype was selected because it already exists within the HVAC test apparatus, and if it were to leak into the system there would be no catastrophic consequence. This oil has a low thermal diffusivity and a high heat flux exists from the heater to the membrane; therefore, large temperature gradients can exist within the oil reservoir. This adds considerably to the uncertainty of the actual piston position. Selecting a different liquid to be used in the chamber will reduce the uncertainty. The search for an appropriate candidate fluid should find one with a large coefficient of thermal expansion, a higher thermal diffusivity, and have the ability to exist in the vicinity of an electrical resistance heater without causing damage to the heater.

Thirdly, the heater used in this prototype was unable to raise the oil temperature to a level capable to bringing the piston to the top of the flow path when operating in the HVAC system. An electric resistance heater with a greater capacity should be used a future design.

These steps are all intermediate design steps, as commercially available parts would likely be too expensive to use in a real world device. After all of the relevant information is obtained, new chamber materials geometry would have to be developed for mass production.

On the fabrication front, there are certain feature limitations that are inherent to the processes. Specifically, since SU8 is a negative type photoresist, any alignment, dosage, or scattering imperfections will ultimately result in nickel pieces whose vertical structures are thinner than the mask dark fields, and whose trench structures are wider than the mask light fields. Although these affects have been minimized through process development, they are still not perfect. The piston described in the prototype had a diameter at its tip between 900 μm and 913 μm; the target diameter for this feature was 950 μm. This ultimately resulted in the piston blocking off a smaller portion of the channel than desired. In order to improve the device performance, the simplest method is to factor in these process limitations during the design at the mask level; i.e. generate new masks with 1000 μm diameter dark fields if 950 μm are desired.

Another task that needs to be done to bring this device from laboratory exploratory work to a commercially viable product is the determination of appropriate assembling and packaging. Specifically, techniques should be developed to assemble these devices at the wafer level. Individual assembly of these devices would likely lead to a product that was too costly for market acceptance.

Finally, the results of the HVAC system tests bring about questions related to refrigerant expansion within the geometry prescribed by this device. The steady state data shows that the device's ability to affect the mass flow rate of refrigerant is heavily dependent on the level of subcooling. Specifically, when plotting the mass flow rate against the subcooling, the actuated device and unactuated device data points diverge. It has been observed through short tube flow visualization experiments, that as subcooling is increased the transition point from liquid to two-phase moves further downstream within the short tube. Extending these observations to the work in this report, it seems likely that these trends can be explained by the transition point from liquid to two-phase being fixed at the point of interaction with the piston. This is purely speculative and not completely understood at the present; laboratory experimentation would be necessary to verify or reject any plausible explanations.

References

[1] 1993 ASHRAE Handbook, *Fundamentals*, American Society of Heating, Refrigerating and Air-Conditioning Engineers, Inc. Atlanta, GA 1993.

[2] D. Aaron and P. Domanski, *An Experimental Investigation and Modeling of the Flow Rate of Refrigerant 22 through the Short Tube Restrictor*, NISTIR 89-4120, United States Department of Commerce, July 1989.

[3] W. V. Payne, *A Universal Mass Flowrate Correlation for Refrigerants and Refrigerant/Oil Mixtures Flowing through Short Tube Orifices*, Ph. D. Dissertation submitted to Texas A&M University, Department of Mechanical Engineering, May 1997.

[4] W. F. Stoecker and J. W. Jones, *Refrigeration and Air Conditioning*, McGraw-Hill, Inc. New York, 1986.

[5] 1988 ASHRAE Handbook, *Equipment*, American Society of Heating, Refrigerating and Air-Conditioning Engineers, Inc. Atlanta, GA 1988.

[6] R. A. Davis, *Influence of Expansion Device and Refrigerant Charge On the Performance of a Residential Split-System Air Conditioner using R-410A Refrigerant*, report prepared for Customer Energy Management, April 2001.

[7] J. Proctor, *Residential and Small Commercial Central Air Conditioning, Rated Efficiency isn't Automatic*, Presentation, ASHRAE Winter meeting, 2004.

[8] R. J. Mowris, A. Blankenship, and E. Jones, *Field Measurements of Air Conditioners with and Without TXVs*, 2004 ACEEE Summer Study Proceedings.

[9] J. Rugh and V. Hovland, *National and World Fuel Savings and CO2 Emission Reductions by Increasing Vehicle Air Conditioning COP*, 2003 Automotive
Alternate Refrigerant Systems Symposium, July 17, 2003.

[10] W. V. Payne and P. Domanski, *Potential Benefits of Smart Refrigerant Distributors*, Air-Conditioning and Refrigeration Technology Institute, ARTI-21CR/605-200-50-01, http://www.fire.nist.gov/bfrlpubs/build02/PDF/b02130.pdf.

[11] K. R. Williams, N. I. Maluf, E. N. Fuller, R. J. Barron, D. P. Jaeggi, and B. P. van Drieenhuizen, *A Silicon Microvalve for the Proportional Control of Fluids*, Digest of the 10th International Conference on Solid-State Sensors and Actuators (Transducers '99), Sendai, Japan, June 1999, pp. 1804-1807.

[12] A. K. Henning, *Liquid and Gas-Liquid Phase Behavior in Thermopneumatically Actuated Microvalves*, Proceedings, Micro Fluidic Devices and Systems (International Society for Optical Engineering, Bellingham, WA, 1998; A. B. Frazier and C. H. Ahn, eds.), volume 3515, pp. 53-63.

[13] A. K. Henning, *Microfluidic MEMS*, Proceedings, IEEE Aerospace Conference, Paper 4,906 (IEEE Press, Piscataway, NJ, 1998).

[14] A. K. Henning, *Microfluidic MEMS for Semiconductor Processing*, Second IEEE International Conference on Innovative Systems in Silicon, Austin TX, October 1997.

[15] A. K. Henning, J. Fitch, D. Hopkins, L. Lilly, R. Faeth, E. Falsken, and M. Zdeblick, *A Thermopneumatically Actuated Microvalve for Liquid Expansion and Proportional Control*, Proceedings Transducers '97: 1997 International Solid State Sensors and Actuators Conference, pp. 825-828.

[16] N. Nguyen and S. Wereley, *Fundamentals and Applications of Microfluidics*, Artech House, Inc., Norwood, MA 2002.

[17] M. Gad-El-Hak, *The MEMS Handbook*, CRC Press, Boca Raton, FL 2002.

[18] Z. Ciu, *A Knowledge Base for Microfluidic Devices*, http://www.ccmicro.rl.ac.uk/info_microfluidics.html 2004.

[19] G. Kovacs, *Micromachined Transducers Sourcebook*, WCB McGraw-Hill, Boston, 1998.

[20] A. P. Papavasiliou, D. Liepmann, and A. Pisano, *Fabrication of a Free Floating Silicon Gate Valve*, Proceedings of IMECE, International Mechanical Engineering Congress and Exposition, Nashville, TN, November 14-19, 1999.

[21] A. P. Papavasiliou, *Bubble-Actuated Planar Microvalves*, Ph. D. Dissertation submitted to the University of California, Berkeley, Department of Mechanical Engineering, Spring 2001.

[22] M. J. Madou, *Fundamentals of Microfabrication*, second edition, CRC Press, Boca Raton, FL 2002.

[23] E. Kukharenka, M. Farooqui, L. Grigore, and M. Kraft, *Electroplating Moulds using Dry Film Thick Negative Photoresist*, Journal of Micromechanics and Microengineering 13 (2003), pp. S67-S74.

[24] L. Guerin, A. Torosdagi, M. Heuschkel, P. Renaud, *Microfluidic Systems Fabrication by Lamination of Photoplastic (SU8) Films*, NANOTECH'98, Montreux, Switzerland.

[25] L. Guerin, *The SU8 Homepage*, http://www.geocities.com/guerinlj/.

[26] T. Baumeister, E. Avallone, and T. Baumeister III, *Marks' Standard Handbook for Mechanical Engineers*, eighth edition, McGraw-Hill, New York, 1978.

[27] E.W. Lemmon, M.O. McLinden, and M.L. Huber, 2002, *NIST Reference Fluids Thermodynamic and Transport Properties − REFPROP 7.0*. Standard Reference Database 23, National Institute of Standards and Technology, Gaithersburg, MD, USA.

[28] J. M. Gere and S. P. Timoshenko, *Mechanics of Materials*, third edition, PWS Publishing Company, Boston, 1990.

[29] N. LaBianca, and J. Delorme, *High Aspect Ratio Resist for Thick Film Applications*, in Proc. SPIE vol. 2438, SPIE, (1995), pp. 846-852.

[30] H. Lorenz, CEO MIMOTEC SA, Switzerland, personal communication.

[31] C. H. Ho, K. P. Chin, C. Yang, H. Wu, and S. Chen, *Ultrathick SU-8 Mold Fabrication and Removal, and its Application of LIGA-like Micromotors with Embedded Roots*, Sensors and Actuators A 102 (2002), pp. 130-138.

[32] R. Feng, and R. J. Farris, *Influence of Processing Conditions on the Thermal and Mechanical Properties of SU8 Negative Photoresist Coatings*, Journal of Micromechanics and Microengineering 13 (2003), pp. 80-88.

[33] Microchem, *NANO SU-8 2000 Negative Tone Photoresist Formulations 2035-2100*, http://www.microchem.com/products/pdf/SU8_2035-2100.pdf.

[34] EVGroup, *Automated SU-8 Resist Processing*, http://www.EVGroup.com.

[35] *SU-8: A Thick Photoresist for MEMS*, http://aveclafaux.freeservers.com/SU-8.html.

[36] K. Lee, N. LaBianca, S. Rishton, and S. Zohlgharnain, *Micromachining Applications for a High Resolution Ultra-Thick Photoresist*, J. Vac. Scien. Technol. B 13 (1995), pp. 3012-3016.

[37] J. M. Shaw, J. D. Gelorme, N. C. LaBianca, W. E. Conley, and S. J. Holmes, *Negative Photoresists for Optical Lithography*, IBM Journal of Research and Development, 41(1997), pp. 81-94.

[38] H. Lorenz, M. Despont, N. Fahrni, N. LaBianca, P. Renaud, P. Vettiger, *EPON SU8: A Low-Cost Negative Resist for MEMS*, MicroMechanics Europ MME 96, Spain, (1996), pp. 32-35.

[39] L. Guerin, C.W. Newquist, P. Renaud, *SU8 Photoepoxy : A New Material for FPD and PDP Applications*, DISPLAY WORKS'98, San Jose, (1998).

[40] W.W. Flack, W.P. Fan, S. White, *The Optimization and Characterization of Ultra-Thick Photoresist Films*, Advances in Resist Technology and Processing XV Proceedings, SPIE 1998 #3333-67.

[41] A. Bertsch, H. Lorenz, and P. Renaud, *3D Microfabrication by Combining Microstereolithography and Thick Resist UV Lithography*, Sensors and Actuators A 73, (1999), pp. 14-23.

[42] B. Eyre, J. Blosiu, and D. Wiberg, *Taguchi Optimization for processing EPON SU8 resist*, Proceedings MEMS'98, Heidelberg, (1998), pp. 218-222.

[43] R. Ruhmann, K. Pfeiffer, M. Falenski, F. Reuther, R. Engelke, and G. Grutzner, *SU-8 – A High Performance Material for MEMS Applications*, mstnews 1/02. http://www.microchem.com/resources/tok_ebeam_resist.pdf.

[44] J. Zhang, K. Tan, and H. Gong, *Polymerization Optimization of SU-8 Photoresist and its Applications in Microfluidic Systems and MEMS*, J. Micromech Microeng. 11(2001), pp. 20-26.

[45] C. H. Lin, G. Lee, B. Chang, and G. Chang, *A New Fabrication Process for Ultrathick Microfluidic Microstructures Utilizing SU-8 Photoresist*, J. Micromech. Microeng. 12 (2002), pp. 590-597.

[46] E.H. Conradie and D. F. Moore, *SU8 Thick Photoresist Processing as a Functional Material for MEMS Applications, J. Micromech. Microeng*. 12 (2002), pp. 368-374.

[47] Z. E. Ling, K. Lian, and L, Jian, *Improved Patterning Quality of SU8 Microstructures by Optimizing the Exposure Parameters*, Proc SPIE 3999 (2000).

[48] P. Jin, K. Jiang, and N. Sun, *Ultra-Thick SU-8 Fabrication for Reciprocating Engines*, Journal of Microlithography, Microfabrication and Microsystems, Vol 3, No. 4, 2004.

[49] H. Lorenz, M. Despont, N. Fahrni, J. Brugger, P. Vettiger, and P. Renaud, *High-Aspect-Ratio, Ultrathick, Negative-Tone Near-UV Photoresist and its Applications for MEMS*, Sensors and Actuators A 64 (1998), pp. 33-39.

[50] P. Renaud Microsystems Laboratory Lausanne, Switzerland, personal communication.

[51] P. M. Dentinger, K. L. Krafcik, K. L. Simison, R. P. Janek, J. Hachman, *High Aspect Ratio Patterning with a Proximity Ultraviolet Source*, Microelectronic Engineering 61-62 (2002), pp. 1001-1007.

[52] G. Stoney, *The Tension of Metallic Films Deposited by Electrolysis*, Proc. Roy. Soc. Lond. A82 (1909).

[53] L. Dellmann, S. Roth, C. Beuret, G. Racine, H. Lorenz, M. Despont, P. Renaud, P. Vettiger, and N. de Rooij, "*Fabrication Process of High Aspect Ratio Elastic Structures for Piezoelectric Motor Applications*", in Proc. Transducers 1997**,** Chicago, (1997). pp. 641-644.

[54] P. M. Dentinger, W. Clift, and S. Goods, *Removal of SU-8 Photoresist for Thick Film Applications*, Microelectronic Engineering 61-62 (2002) pp. 933-1000.

[55] P. M. Dentinger, *Removal of SU-8 Photoresist for Thick film Applications II: Dry Techniques*, Micro and Nano Engineering Conference 2001, Sept. 16-19, 2001, Grenoble, France.

[56] G. Hong, A. S. Holmes, and M. E. Heaton, *SU8 Resist Plasma Etching and its Optimization*, DTIP 2003, Mandelieu-La Napoule, France, 5-7 May 2003.

[57] P. M. Dentinger, *Removal of SU-8 Photoresist for Thick film Applications II: Wet Techniques*, Micro and Nano Engineering Conference 2001, Sept. 16-19, 2001, Grenoble, France.

[58] P. Renaud, H. Van Lintel, M. Heuschkel, L. Guerin, *Photo-Polymer Microchannel Technologies and Applications*, μTAS'98, Banff, Alberta, 1998, pp. 17-22.

[59] L. Guerin, M. Bossel, M. Demierre, S. Calmes, and P. Renaud, *Simple and Low Cost Fabrication of Embedded Microchannels by Using a New Thick-Film Photoplastic*, Transducers 1997, Chicago, (1997), 1419-1422.

[60] T. Fritz, T. Leuerer, C. Krueger, W. Mokwa, and U. Schnakenberg, *Mechanical Properties of Electroplated Nickel*. Technical Digest Micro Materials 2000, 3rd International Conference and Exhibition, Berlin, Germany, April 17-19 (2000), pp. 752-755.

[61] W. J. Callister *Materials Science and Engineering, An Introduction*, third edition, John Wiley & Sons, Inc. New York, 1994.

[62] K. B. Lee, and L. Lin, *Zinc Bonding for MEMS Packaging at the Wafer-Level*, Proceedings of 2001 ASME International Mechanical Engineering Congress and Exposition, November 11-16, 2001, New York, NY

[63] R. W. Fox and A. T. McDonald, *Introduction to Fluid Mechanics*, fourth edition, John Wiley & Sons, Inc. 1992.

[64] F. P. Incropera and D. P. DeWitt, *Fundamentals of Heat and Mass Transfer*, third edition, John Wiley & Sons, Inc. New York, 1990.

[65] H. M. Deitel and P. J. Deitel, *C How to Program*, second edition, Prentice-Hall, Inc. New Jersey, 1994.

[66] B. K. Hodge and K. Koenig, *Compressible Fluid Dynamics with Personal Computer Applications*, Simon and Schuster, 1995.

[67] Y. Kim, *Two-Phase Flow of HCFC-22 and HFC-134a Through Short Tube Orifices*, Ph D. Dissertation, Texas A&M University, College Station TX, 1993.

Appendix A

Raw Code for Transient Analysis

```
#include<stdio.h>
#include<math.h>

void main()
{
 int m, n, conv, weight_factor;
 double t, totalheatgen, heatgen, timestep, change;
 double heatgenpercell, mschange, rms_change, weighted_temp, average_temp;
 double T_old[53][217], T_new[53][217];



conv=0;
totalheatgen=0.0;
timestep=0.0001;
t=0.0-timestep;
heatgen=totalheatgen/146.0;
heatgenpercell=4*heatgen/(0.000000000003375*3.1415927);

/***********************/
/* Set initial values */
/***********************/
for(m=1; m<52; m++){
 for(n=1; n<=216; n++){
  T_old[m][n]=20;
  }
 }

/*****************************/
/*Set the boundary conditions*/
/*****************************/
for(n=1; n<=216; n++){
 T_old[52][n]=25.0;
 T_new[52][n]=25.0;}

for(m=1; m<=52;m++){
 T_old[m][1]=25.0;
 T_new[m][1]=25.0;
 T_old[m][216]=5.0;
 T_new[m][216]=5.0;}

/*******************************/
/* Temperature calculation loop*/
/*******************************/

while(conv==0){
```

```
 t=t+timestep;
 mschange=0.0;
/************************/
/*Calculate temperatures*/
/************************/
 for(m=1; m<=51; m++){
  for(n=2; n<=215; n++){
   if(m==1){
    if(n==68){
     /*USE EQUATION #7 FOR OIL-BRASS*/
     T_new[m][n]=T_old[m][n]+
      0.36149573*(T_old[m+1][n]-T_old[m][n])+
      0.00163896*(110*(T_old[m][n-1]-T_old[m][n])+
       0.282*(T_old[m][n+1]-T_old[m][n]));
     }
    else{
     if(n==215){
      /*USE EQUATION #7 FOR NI-OIL*/
      T_new[m][n]=T_old[m][n]+
       0.26370056*(T_old[m+1][n]-T_old[m][n])+
       0.00144919*(0.282*(T_old[m][n-1]-T_old[m][n])+
        90.7*(T_old[m][n+1]-T_old[m][n]));
      }
     else{
      if(n>68){
       /*USE EQUATION #6 FOR OIL*/
       T_new[m][n]=T_old[m][n]+
        0.002297422*(T_old[m+1][n]-T_old[m][n])+
        0.000574356*(T_old[m][n-1]+T_old[m][n+1]-2*T_old[m][n])+
        +0.000000000045826*heatgenpercell;
       }
      else{
       /*USE EQUATION #6 FOR BRASS*/
       T_new[m][n]=T_old[m][n]+
        0.603306667*(T_old[m+1][n]-T_old[m][n])+
        0.150826667*(T_old[m][n-1]+T_old[m][n+1]-2*T_old[m][n]);
       }
      }
     }
    }
   else{
    if(n==68){
     if(m==42){
      /*USE EQUATION #5 FOR OIL-BRASS*/
      T_new[m][n]=T_old[m][n]+
       (0.001493141536/m)*(55.141*((m-0.5)*(T_old[m-1][n]-T_old[m][n]))-
```

```
      110*((m+0.5)*(T_old[m][n]-T_old[m+1][n])))+
      0.001493141536*(110*(T_old[m][n-1]-T_old[m][n])-55.141*(T_old[m][n]-
      T_old[m][n+1]));
   }
  else{
   if(m>42){
    /*USE EQUATION #1 FOR BRASS*/
    T_new[m][n]=T_old[m][n]+
     (0.15082646/(m*m))*(T_old[m+1][n]-T_old[m][n]+m*m*(T_old[m+1][n]+T_old[m-1][n]-
       2*T_old[m][n]))+0.15082646*(T_old[m][n+1]+T_old[m][n-1]-2*T_old[m][n]);
     }
   else{
    /*USE EQUATION #2 FOR OIL-BRASS*/
    T_new[m][n]=T_old[m][n]+(0.090373933/m)*((m-0.5)*(T_old[m-1][n]-T_old[m][n])-
        (m+0.5)*(T_old[m-1][n]-T_old[m][n]))+0.0016389607*(110*(T_old[m][n-1]-
        T_old[m][n])-0.282*(T_old[m][n]-T_old[m][n+1]));
    }
   }
  }
 else{
  if(n==215){
   if(m==42){
    /*USE EQUATION #4 FOR NI-OIL*/
    T_new[m][n]=T_old[m][n]+(0.0012665039/m)*(45.491*(m-0.5)*(T_old[m-1][n]-
       T_old[m][n])-90.7*(m+0.5)*(T_old[m][n]-T_old[m+1][n]))+
       0.0012665039*(45.491*(T_old[m][n-1]-T_old[m][n])-90.7*(T_old[m][n]-
        T_old[m][n+1]));
    }
   else{
    if(m>42){
     /*USE EQUATION #2 FOR NI-BRASS*/
     T_new[m][n]=T_old[m][n]+(0.1240094536/m)*((m-0.5)*(T_old[m-1][n]-T_old[m][n])-
        (m+0.5)*(T_old[m-1][n]-T_old[m][n]))+0.00123576934*(110*(T_old[m][n-1]-
         T_old[m][n])-90.7*(T_old[m][n]-T_old[m][n+1]));
     }
    else{
     /*USE EQUATION #2 FOR NI-OIL*/
     T_new[m][n]=T_old[m][n]+(0.06592514/m)*((m-0.5)*(T_old[m-1][n]-T_old[m][n])-
        (m+0.5)*(T_old[m-1][n]-T_old[m][n]))+0.00144919083*(0.282*(T_old[m][n-1]-
        T_old[m][n])-90.7*(T_old[m][n]-T_old[m][n+1]));
     }
    }
   }
  else{
   if(m==42){
    if(n>68){
```

```
      /*USE EQUATION #1 FOR BRASS*/
      T_new[m][n]=T_old[m][n]+(0.15082646/(m*m))*(T_old[m+1][n]-
          T_old[m][n]+m*m*(T_old[m+1][n]+T_old[m-1][n]-2*T_old[m][n]))+
          0.15082646*(T_old[m][n+1]+T_old[m][n-1]-2*T_old[m][n]);
      }
     else{
      /*USE EQUATION #3 FOR OIL-BRASS*/
      T_new[m][n]=T_old[m][n]+(0.00163896072/m)*(0.282*((m-0.5)*(T_old[m-1][n]-
          T_old[m][n]))-110*((m+0.5)*(T_old[m][n]-T_old[m+1][n])))+
          (0.090373933)*(T_old[m][n-1]+T_old[m][n+1]-2*T_old[m][n]);
      }
     }
    else{
     if(n>68 && m<42){
      /*USE EQUATION #1 FOR OIL*/
      T_new[m][n]=T_old[m][n]+(0.00057435556/(m*m))*(T_old[m+1][n]-
         T_old[m][n]+m*m*(T_old[m+1][n]+T_old[m-1][n]-2*T_old[m][n]))+
         0.00057435556*(T_old[m][n+1]+T_old[m][n-1]-2*T_old[m][n]);
      }
     else{
      /*USE EQUATION #1 FOR BRASS*/
      T_new[m][n]=T_old[m][n]+(0.15082646/(m*m))*(T_old[m+1][n]-
         T_old[m][n]+m*m*(T_old[m+1][n]+T_old[m-1][n]-2*T_old[m][n]))+
         0.15082646*(T_old[m][n+1]+T_old[m][n-1]-2*T_old[m][n]);
      }
     }
    }
   }
  }
  change=(T_old[m][n]-T_new[m][n])/T_old[m][n];
  mschange=mschange+change*change;
  T_old[m][n]=T_new[m][n];

  }/*next n*/
 }/*next m*/
rms_change=sqrt(mschange/(10650.0));
if(rms_change<0.000001){
 conv=1;
 }

/*if(floor(t)==t){
 printf("The temperature distribution at time %d is\n", t);
 printf("          m          n          Temperature\n");
 for(m=0;m<51;m++){
  for(n=0;n<215;n++){
   printf("        %d       %d       %f\n", m, n, T_old[m][n]);
```

```
   }
  }
 }*/

 } /*closes while*/

/************************************/
/*Calculate average oil temperature*/
/************************************/
weighted_temp=0.0;
weight_factor=0;
for(m=1; m<42; m++){
 for(n=68; n<215; n++){
  weighted_temp=weighted_temp+m*T_old[m][n];
  weight_factor=weight_factor+m;
  } /*next n*/
 } /*next m*/
average_temp=weighted_temp/weight_factor;

/*****************/
/*Output Results*/
/*****************/

printf("The solution achieved steady state at time %f\n", t);
printf("The average oil temperature is %f\n", average_temp);
printf("m        n        Temperature\n");
for(m=1;m<=52;m++){
 for(n=1;n<=216;n++){
  printf("        %d      %d      %f\n", m, n, T_old[m][n]);
  }
 }
}/*closes main*/
```

Appendix B

Air Flow Measurement Data and Uncertainty

B.1 Raw Data

Table B.1 Data Set #1 – Data Taken November 4, 2005, 9 am

Point	Oil Temperature (°C)	Upstream Pressure (kPa)	Time (s)	Volume of Air Collected (l)	Air Temperature (°C)	Calculated Air Density (kg/m^3)	Calculated Mass Flow Rate (kg/s)
1	22.89	312.5	40	7.8	29.44	1.1635736	0.000226897
2	27.39	315.8	40	7.5	27.44	1.1655004	0.000218531
3	29.78	315.0	40	7.3	28.56	1.1670035	0.000212978
4	35.83	313.5	45	7.8	29.67	1.1627193	0.000201538
5	41.83	316.3	45	7.3	29.28	1.1642152	0.000188862

Table B.2 Data Set #2 – Data Taken November 4, 2005, 1 pm

Point	Oil Temperature (°C)	Upstream Pressure (kPa)	Time (s)	Volume of Air Collected (l)	Air Temperature (°C)	Calculated Air Density (kg/m^3)	Calculated Mass Flow Rate (kg/s)
6	23.00	315.0	40	7.6	28.00	1.1691574	0.00022214
7	28.22	316.6	40	7.6	29.61	1.1629328	0.000220957
8	30.06	315.6	40	7.3	29.28	1.1642152	0.000212469
9	37.00	314.1	45	7.7	28.44	1.1674336	0.000199761
10	44.44	315.0	50	8.0	29.39	1.1637874	0.000186206

Table B.3 Data Set #3 – Data Taken November 4, 2005, 5 pm

Point	Oil Temperature (°C)	Upstream Pressure (kPa)	Time (s)	Volume of Air Collected (l)	Air Temperature (°C)	Calculated Air Density (kg/m^3)	Calculated Mass Flow Rate (kg/s)
11	23.06	316.2	40	7.8	29.0	1.1652860	0.000227231
12	28.89	317.6	40	7.5	29.56	1.1631463	0.000218090
13	33.28	315.2	45	8.0	28.72	1.1663588	0.000207353
14	37.67	316.5	45	7.7	27.94	1.1693732	0.000200093
15	44.83	315.6	45	7.2	29.17	1.1646433	0.000186343

Table B.4 Data Set #4 – Data Taken November 4, 2005, 7 pm

Point	Oil Temperature (°C)	Upstream Pressure (kPa)	Time (s)	Volume of Air Collected (l)	Air Temperature (°C)	Calculated Air Density (kg/m^3)	Calculated Mass Flow Rate (kg/s)
16	23.06	315.9	40	7.7	29.61	1.1629328	0.000223865
17	29.22	317.0	40	7.5	29.78	1.1622926	0.00021793
18	35.33	312.7	45	7.8	29.61	1.1629328	0.000201575
19	41.39	317.6	45	7.2	29.00	1.1652860	0.000186446

B.2 Uncertainty Analysis for Gas Flow Measurements

The air flow rate is calculated from the measured atmospheric air pressure, the volume and temperature of the air collected in the cylinder, and the time elapsed during the collection. The mass flow rate is related through these parameters as follows:

$$\dot{m} = \frac{\rho \forall}{t} = \frac{\forall}{t}\rho\left(P_{atm}, T_{air}\right)$$

Although Refprop [27] was used to calculate the density of the air in the cylinder, it is convenient to use the ideal gas law for the purposes of the uncertainty analysis.

$$\dot{m} = \frac{\forall}{t}\frac{P_{atm}}{\mathrm{R}T_{air}}$$

Therefore the influence of each measured parameter is:

$$\frac{\partial \dot{m}}{\partial \forall} = \frac{P_{atm}}{t\mathrm{R}T_{air}}$$
$$\frac{\partial \dot{m}}{\partial P_{atm}} = \frac{\forall}{t\mathrm{R}T_{air}}$$
$$\frac{\partial \dot{m}}{\partial t} = -\frac{\forall P_{atm}}{t^2\mathrm{R}T_{air}}$$
$$\frac{\partial \dot{m}}{\partial T_{ait}} = -\frac{\forall P_{atm}}{t\mathrm{R}\left(T_{air}\right)^2}$$

And the uncertainty of the mass flow rate is found from the uncertainty of each measurement.

$$U_{\dot{m}} = \sqrt{\left(\frac{\partial \dot{m}}{\partial \forall}U_{\forall}\right)^2 + \left(\frac{\partial \dot{m}}{\partial P_{atm}}U_{P_{atm}}\right)^2 + \left(\frac{\partial \dot{m}}{\partial t}U_t\right)^2 + \left(\frac{\partial \dot{m}}{\partial T_{air}}U_{T_{air}}\right)^2}$$

Table B.5 Calculated Uncertainty for all data

Point	dm_dot/dV	dm_dot/dP_atm	dm_dot/dt	dm_dot/dT_air	Uncertainty	U (%)
1	0.029214725	2.24729E-09	5.69687E-06	7.53444E-07	4.08096E-06	1.799%
2	0.029263103	2.16443E-09	5.48683E-06	7.26866E-07	4.01185E-06	1.836%
3	0.029300841	2.10943E-09	5.3474E-06	7.09309E-07	3.96725E-06	1.863%
4	0.025949578	1.99612E-09	4.49793E-06	6.68745E-07	3.43455E-06	1.704%
5	0.025982963	1.87057E-09	4.21501E-06	6.27488E-07	3.34614E-06	1.772%
6	0.029354921	2.20017E-09	5.57744E-06	7.41187E-07	4.04964E-06	1.823%
7	0.029198635	2.18846E-09	5.54774E-06	7.33316E-07	4.02807E-06	1.823%
8	0.029230833	2.10439E-09	5.33463E-06	7.05924E-07	3.95777E-06	1.863%
9	0.026054792	1.97852E-09	4.45826E-06	6.65535E-07	3.42957E-06	1.717%
10	0.023376074	1.84427E-09	3.74017E-06	6.18437E-07	2.99424E-06	1.608%
11	0.02925772	2.25059E-09	5.70526E-06	7.55663E-07	4.08697E-06	1.799%
12	0.029203996	2.16006E-09	5.47575E-06	7.23933E-07	4.00374E-06	1.836%
13	0.026030805	2.05371E-09	4.6277E-06	6.90193E-07	3.48349E-06	1.680%
14	0.02609808	1.98181E-09	4.46567E-06	6.67749E-07	3.43527E-06	1.717%
15	0.025992517	1.84562E-09	4.1588E-06	6.19347E-07	3.32924E-06	1.787%
16	0.029198635	2.21725E-09	5.62074E-06	7.42965E-07	4.05331E-06	1.811%
17	0.029182562	2.15847E-09	5.47173E-06	7.22871E-07	4.0008E-06	1.836%
18	0.025954342	1.99649E-09	4.49875E-06	6.6899E-07	3.43518E-06	1.704%
19	0.026006862	1.84664E-09	4.1611E-06	6.20031E-07	3.33108E-06	1.787%

Appendix C
Test Data and Uncertainty for Refrigerant Flow Control Measurements

In the interest of saving space, the measurement uncertainty methodology is presented in the beginning of this section and the Uncertainty is included in the raw data portion of this appendix.

C.1 Uncertainty Analysis

The capacity of heat transferred in the evaporator is measured on the refrigerant side and on the HTF side.

HTF side uncertainty

The HTF side capacity is determined by measuring the HTF temperature at the inlet and exit of the evaporator, and the HTF mass flow rate. The average of the inlet and exit temperature is used to determine the HTF specific heat, Cp.

$$C_p = 1.805\left(T_{HTF,in} + T_{HTF,out}\right) + 3304.357$$

Therefore, the uncertainty of the specific heat measurement is:

$$U_{C_p} = \sqrt{1.805\left(U_{T_{HTF,in}}{}^2 + U_{T_{HTF,out}}{}^2\right)}$$

Since each temperature is measured with 5 thermocouples, each having a measurement uncertainty of 0.15 ºC, the uncertainty of each of these values is 0.0067 ºC, and the uncertainty of the specific heat is a constant 0.00127, which is insignificant for specific heats in the range of 3300 and will be left off of the remainder of the calculations.

The capacity is calculated from the product of the mass flow rate with the difference between the inlet temperature and the exit temperature.

$$Q = \dot{m} C_P \left(T_{HTF,in} - T_{HTF,out}\right)$$

Therefore the uncertainty due to the mass flow measurement uncertainty is:

$$\frac{\partial Q}{\partial \dot{m}} = \frac{C_P}{\left(T_{HTF,in} - T_{HTF,out}\right)}$$

And the uncertainties due to the measured temperatures are:

$$\frac{\partial Q}{\partial T_{HTF,in}} = \dot{m} C_P$$

$$\frac{\partial Q}{\partial T_{HTF,in}} = \dot{m} C_P$$

Therefore, the measurement uncertainty of the HTF side capacity is

$$U_Q = \sqrt{\left[\left(\frac{\partial Q}{\partial \dot{m}}\right) U_{\dot{m}}\right]^2 + \left[\left(\frac{\partial Q}{\partial T_{HTF,in}}\right) U_{T_{HTF,in}}\right]^2 + \left[\left(\frac{\partial Q}{\partial T_{HTF,in}}\right) U_{T_{HTF,in}}\right]^2}$$

The refrigerant side capacity is calculated by measuring the valve inlet temperature, the evaporator exit temperature, pressure, and volumetric flow rate. The valve inlet temperature is used to determine the liquid enthalpy, the evaporator exit temperature and pressure are used to determine the vapor enthalpy and the vapor density. The capacity is then calculated from:

$$Q = \rho \dot{\forall} \left(h_{ref,vap} - h_{ref,liq}\right)$$

The uncertainty of the liquid enthalpy is:

$$U_{h_{rev,liq}} = \frac{\partial h_{liq}}{\partial T_{ref,liq}} U_{T_{ref,liq}}$$

And the uncertainty of the vapor enthalpy is:

$$U_{h_{rev,vap}} = \sqrt{\left(\frac{\partial h_{vap}}{\partial T_{ref,vap}} U_{T_{ref,vap}}\right)^2 + \left(\frac{\partial h_{vap}}{\partial P_{ref,vap}} U_{P_{ref,vap}}\right)^2}$$

The uncertainty of the density term is

$$U_\rho = \sqrt{\left(\frac{\partial \rho}{\partial T_{ref,vap}} U_{T_{ref,vap}}\right)^2 + \left(\frac{\partial \rho}{\partial P_{ref,vap}} U_{P_{ref,vap}}\right)^2}$$

Therefore, the uncertainty of the capacity measurement is:

$$U_{Q_{ref}} = \sqrt{\left(\rho \dot{\forall} U_{h_{ref,vap}}\right)^2 + \left(\rho \dot{\forall} U_{h_{ref,liq}}\right)^2 + \left(\dot{\forall} \Delta h U_\rho\right)^2 + \left(\Delta h \rho U_{\dot{\forall}}\right)^2}$$